DETERMINATION OF GLACIAL-ICE TEMPERATURE PROFILES USING RADAR AND AN ANTENNA-GAIN ESTIMATION TECHNIQUE

BY

Mike Hughes

Submitted to the graduate degree program in Electrical Engineering
and the Graduate Faculty of the University of Kansas School of Engineering
in partial fulfillment of the requirements for the degree of
Master of Science

_____

Dr. Kenneth Demarest
Chairperson

Committee Members* _____

Dr. Chris Allen*

_____

Dr. Carl Leuschen*

Date defended: _____

The Thesis Committee for Mike Hughes certifies
That this is the approved Version of the following thesis:

DETERMINATION OF GLACIAL-ICE TEMPERATURE PROFILES USING RADAR AND AN ANTENNA-GAIN ESTIMATION TECHNIQUE

Committee:

_____
Dr. Kenneth Demarest
Chairperson

_____
Dr. Chris Allen

_____
Dr. Carl Leuschen

Date defended: _____

ABSTRACT

Knowledge of glacial ice temperature profiles is important to the study of glaciology. Currently, the only method of obtaining ice temperature profiles is by drilling ice cores, which is a long and arduous process. Fortunately, ice-penetrating radar can be used to obtain temperature profiles without the need of ice cores. A radar technique incorporating common mid-point geometries is presented for measuring ice temperature. However, in order for this technique to work, accurate estimates of the far-zone antenna gain within glacial ice are necessary. Currently, commercial electromagnetics software packages utilizing the finite element method (FEM) are used by academia and industry to accurately characterize antennas in free space, and near finite dielectric and conductive materials. Unfortunately, these commercial packages are incapable of accurately determining the far-zone antenna gain near a dielectric half-space such as glacial ice. Therefore, to solve this problem, a routine for determining the far-zone gain of an antenna located near glacial ice was developed, which utilizes an FEM package in conjunction with a near-to-far-field transformation (NFFT). Additionally, glacial ice imposes another complication to estimating far-zone antenna gain: the dielectric constant is a function of depth. Therefore the far-zone antenna gain within glacial ice changes as a function of depth due to increased ray bending resulting from refraction. To solve this problem, the geometric optics technique (GO) was used to propagate the far-zone antenna gain determined within the relatively shallow upper region of glacial ice, dubbed the quasi-far-zone, to any depth within glacial ice. Results are presented showing that this technique is capable of accurately determining the far-zone gain at any depth within glacial ice for an arbitrary antenna located near glacial ice. Additionally, results are presented showing that with the aid of this numerical antenna gain estimation software, ice-penetrating radar can be used to determine glacial ice temperature profiles at all depths.

ACKNOWLEDGEMENT

I would like to thank Dr. Demarest for being my adviser and committee chair. His support and vast knowledge of electromagnetics made this work possible. I would also like to thank Dr. Allen and Dr. Leuschen for serving on my committee, and providing their invaluable support and insight. Also, while at CReSIS, I had the fortune of being exposed to numerous areas of remote-sensing. Therefore, I wish to thank all the faculty, staff, and students at CReSIS for their support in furthering my development as an electrical engineer.

TABLE OF CONTENTS

LIST OF FIGURES

LIST OF TABLES

CHAPTER 1: Introduction

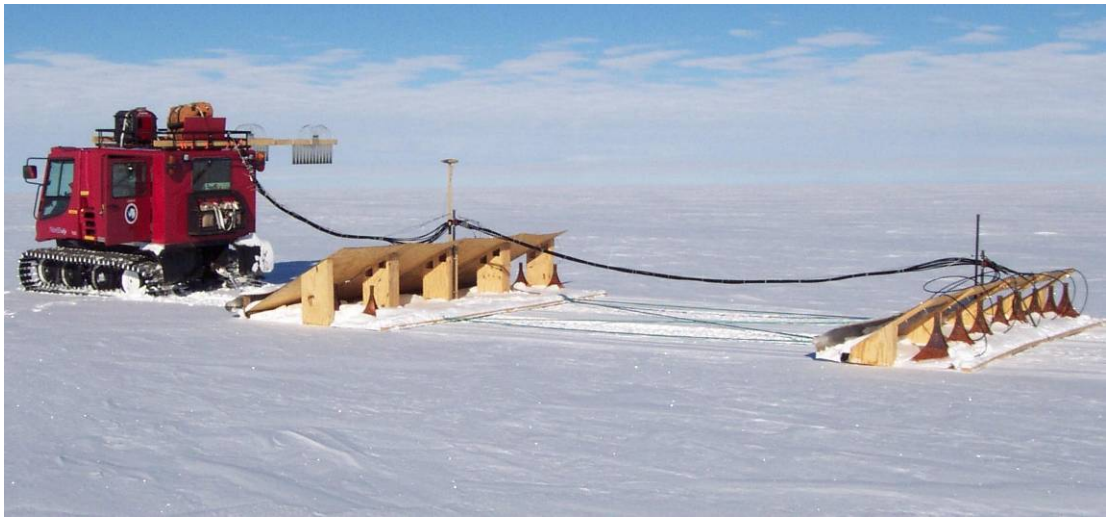

Figure 1.1 – Ice-Penetrating Radar System

1.1 Motivation

Glaciers play an integral role in the global climate. They hold the majority of Earth's fresh water, have played a key role in shaping much of the Earth's surface, and provide a record of past climate conditions. In addition, glaciers are of ever increasing interest due to the onset of global climate change, since scientists consider the glacial mass balance to be an indicator of future trends in climate change [31]. Additionally, due to the vast amount of fresh water encompassing glacial ice sheets, particularly those in Antarctica and Greenland, rapidly melting glaciers could cause dramatic increases in sea levels, inundating coastal areas. Scientific models are required to fully understand the interaction between glaciers and the global climate. However, scientists are currently lacking the accurate data necessary to produce such models, and the understanding of many aspects of glaciers remains poor [31].

One particularly powerful technique for obtaining accurate data pertaining to glacial ice is radar remote-sensing, hereafter called ice-penetrating radar (Figure 1.1). Currently, ice-penetrating radar is used to map bed conditions, surface conditions, and

internal layers of glacial ice, allowing such calculations as ice thickness and annual snow accumulation. However, with accurate knowledge of the far-zone antenna radiation pattern within glacial ice, the full power of ice-penetrating radar can be utilized. With this knowledge, the attenuation as a function of depth can be accurately determined. Then, since it is directly related to attenuation, temperature as a function of depth can be obtained.

Glacial ice temperature profiles are invaluable to the study of glaciers and climate. In particular, “ice temperature is important for a variety of glacial processes, including glacial flow, meltwater drainage, and subglacial erosion and deposition,” [31]. Currently however, obtaining ice temperature profiles is a long and difficult process, since it requires the drilling of ice cores, a process that can take years to complete. The ability to use ice-penetrating radar in obtaining temperature profiles would eliminate the need for drilling ice cores to obtain temperature measurements. This would make temperature profiles much easier to obtain over much broader areas of the Antarctica and Arctic ice sheets, which should greatly improve the science of studying glaciers and climate. Next, the proposed radar set-up for measuring ice temperature is presented.

1.2 Radar Set-Up for Attenuation Profiling

The proposed radar set-up for determining glacial ice attenuation as a function of depth involves placement of both transmit and receive antennas directly on the ice-cap surface in common midpoint (CMP) geometry. Two separate CMP configurations are utilized to achieve two separate signals off of each resolution layer [27], as shown in Figure 1.2. The resolution layer shown in Figure 1.2 is 100 meters, and indicates the depth-range for which a single attenuation value is obtained. Also, the use of two separate CMP configurations is desirable since it reduces some of the uncertainties associated with attenuation profile extraction [32].

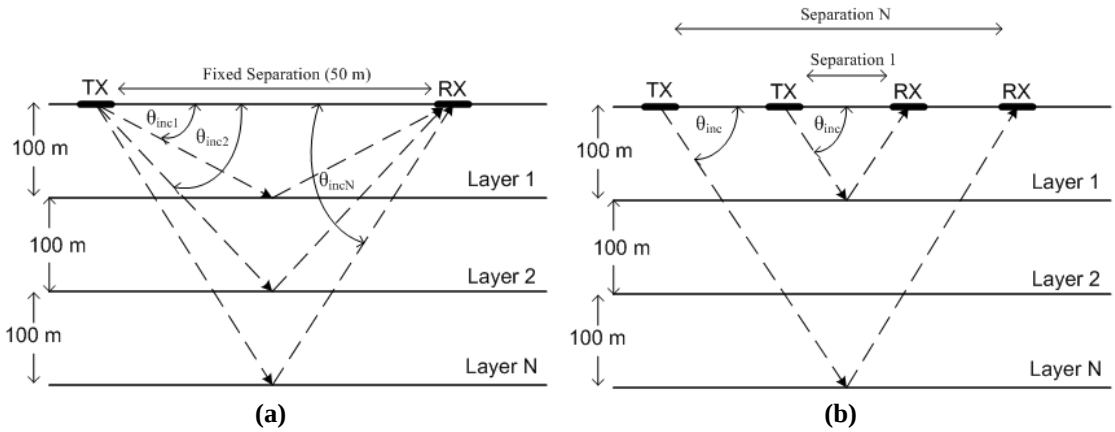

Figure 1.2 – Bistatic-Radar Common Midpoint Configurations

(a) Configuration 1 – Fixed Separation (b) Configuration 2 – Fixed Incident Angle

In the first CMP configuration shown in Figure 1.2(a), the antennas are set at a fixed distance from each other. A 50 m separation was used in this case. Signals are returned from each resolution layer at this fixed antenna separation at different incident angles. In the second CMP configuration shown in Figure 1.2(b), the antenna separation is varied so as to maintain a fixed incident and reflected angle between the antennas and the resolution layer of interest.

Figure 1.2 displays the rays traveling between each antenna as propagating in a straight line. In reality, these rays are continuously refracted towards the normal direction with increasing depth. Therefore, in order to accurately determine ice attenuation as a function of depth, the effect of refraction as a function of depth must be incorporated in the estimation of far-zone antenna gain.

In order to indicate the necessity of accurate far-zone antenna gain estimation in accurately determining ice attenuation, the radar range equation in terms of loss [32], L (attenuation), and based on CMP geometry is presented below

$$L = \frac{P_t G^2 \lambda^2 \Gamma_{ice}}{P_r (8\pi R)^2} \qquad \textbf{Eq. 1.1}$$

The parameters P_r and P_t are the power received and transmitted which are accurately known. Also, R is the range to the target which is determined by the round-trip transit time of the radar signal. Additionally, Γ_{ice} is the internal ice specular reflection coefficient which can be assumed to be -80 dB. However, any uncertainties associated with Γ_{ice} are eliminated through use of the two combined radar CMP configurations (see Chapter 4). Therefore, the only unknown in Equation 1.1 required in determining the loss L is the antenna gain G. Equation 1.1 assumes the transmit and receive antennas are identical, which is the case for the two proposed CMP geometries.

One proposed radar system for determining glacial ice attenuation as a function of depth is the wideband bi-static ice depth sounder designed by David Dunson [12]. The key system parameters associated with this radar are outlined in Table 1.1. The parameters shown in Table 1.1 are used in producing the simulated attenuation results shown in Chapter 5.

Table 1.1 – Radar System Key Parameters

Parameters	Values
Radar Type	Pulse Compression, Coherent Receiver
TX & RX Antenna Gain	3 dB
Chirp Frequency Range	120 MHz to 300 MHz
Transmitting Power	800 W
Receiver Noise Figure	2 dB
Pulse Duration	1 μs or 10 μs
Equivalent Receiver Noise Temperature	253 K

1.3 The Importance of Predicting Antenna Gain

As shown in Section 1.2, accurate predictions of antenna gain are required in order to accurately measure glacial ice attenuation. For most antennas, this is not a

simple task. Due to the complexity of most modern antennas (and other electronic devices), their analysis does not lead to closed form solutions of Maxwell's equations. Therefore, numerical methods for approximating these solutions while maintaining engineering accuracy is required [39]. A number of numerical techniques exist for approximating solutions to Maxwell's equations, each of which differ in the way they discretize the problem from the continuous domain. One means of categorizing these techniques is to separate them into those based on partial differential equation formulations, and those based on integrodifferential equation formulations.

The two most popular techniques within the partial differential equation category are the finite difference (FD) and finite element method (FEM). Either of these techniques can be exploited in the time or frequency domain. However, FD is usually exploited in the time domain, and called the FDTD (finite-difference time-domain) technique [26]. Both of these techniques are similar in that they directly solve for the near-zone electric and magnetic fields within a finite solution space. Also, since both of these techniques solve for fields within a finite space, boundary conditions and hybrid methods are required for analyzing open structures to transform the infinite region to a finite one [39]. Although both the FDTD and FEM techniques are well-suited for arbitrary and versatile materials and geometries, and considered computational efficient, the FEM is considered to be slightly superior to the FDTD in these categories [39]. In particular, the FEM technique is much better suited for arbitrary geometries than the FDTD [7].

The most popular technique within the integrodifferential equation category is the method of moments (MoM) [19]. Rather than solving directly for the fields within a finite solution space, as with the FEM and FDTD techniques, the MoM works by determining the currents on individual segments of the antenna structure resulting from the antenna excitation [19]. Also, unlike the FEM and FDTD techniques, the MoM is best suited for open structures [39]. Therefore, the MoM can directly determine far-zone patterns in an open region without the requirement of hybrid techniques. Two major drawbacks of the MoM however, are its inability to analyze

problems of arbitrary materials (i.e. dielectrics) or geometries. But, although the MoM is not generally well-suited for antennas that contain dielectrics, some formulations, such as the Numerical Electromagnetic Code (NEC) [8] can model wire antennas on or near a dielectric half-space, and provide far-zone patterns within that half-space using a near-to-far-field transformation. Although glacial ice is a dielectric half-space, it presents other difficulties discussed in the next section.

1.4 Complications in Determining Antenna Gain within Glacial Ice

Glacial ice significantly alters the gain pattern of antennas relative to their free-space counterparts. The alteration is initially caused by the permittivity of ice being greater than that of free space, leading to increased radiation in glacial ice relative to the free-space pattern. This initial alteration of the gain pattern can be determined by modeling the antenna above an infinite dielectric half-space of ice with a dielectric constant equal to that at the ice surface.

In reality, the dielectric constant of glacial ice is not constant, but increases with increasing depth to a maximum value, which is that of pure ice. This dielectric constant gradient is caused by increasing pressure with depth yielding an increased density with depth, which is related to the dielectric constant. Therefore, the energy propagating from the antenna within glacial ice is continuously refracted towards the normal with increasing depth, which further modifies the far-zone antenna gain.

West and Demarest [46] handled the problems associated with determining far-zone antenna gain within glacial ice for simple wire antennas. They used the NEC in conjunction with geometric optics ray tracing (GO) to develop a two-step hybrid technique for finding the far-zone gain of wire-type antennas mounted on or near glacial ice with depth-dependant density profiles. Due to the depth-dependant density profile of glacial ice, the hybrid technique was required. The NEC code was used to calculate the electromagnetic fields within the upper-surface of the ice. Then, GO was

used to calculate the antenna gain increase over the antenna gain determined in the upper-surface of the ice, resulting form the focusing effect of the ice density profile.

The MoM-GO technique proposed by West and Demarest proved useful for wire-type antennas mounted above glacial ice. But, due to the inability of the MoM to analyze complex materials and geometries, the MoM is unsuitable for analyzing the complex antennas often used in modern ice-penetrating radars. Therefore, a technique capable of analyzing modern complex antennas, as well as dealing with the complicated material properties of glacial ice is required, which is presented next.

1.5 A Solution for Determining Far-Zone Antenna Gain in Glacial Ice

Accurate far-zone antenna gain estimations are required in order to accurately measure ice attenuation as a function of depth. However, from Section 1.4, it is apparent that glacial ice complicates the far-zone gain estimation. With the exception of the MoM-GO technique, none of the previously discussed antenna analysis techniques are capable of dealing with the far-zone gain altering effects of glacial ice. However, the MoM-GO technique is only capable of modeling simple wire-type antennas above glacial ice. Therefore, a technique capable of handling both complicated antennas and the gain-altering effects of glacial ice is required.

As discussed in Section 1.3, the FEM technique is the best at handling complicated structures, but on its own is incapable of modeling infinite structures such as an antenna in the presence of a glacial ice. In order to analyze radiating structures in the presence of a very large problem domain using rigorous methods such as FEM, it is necessary to use hybrid techniques [13]. In fact even in the presence of an infinite homogeneous background, the commercial FEM code HFSS requires the combination of FEM and an NFFT (near-to-far-field transformation) algorithm to determine far-zone fields. However, electrically large inhomogeneous

backgrounds are more difficult and each specific problem requires its own technique [9, 13, 24, and 45].

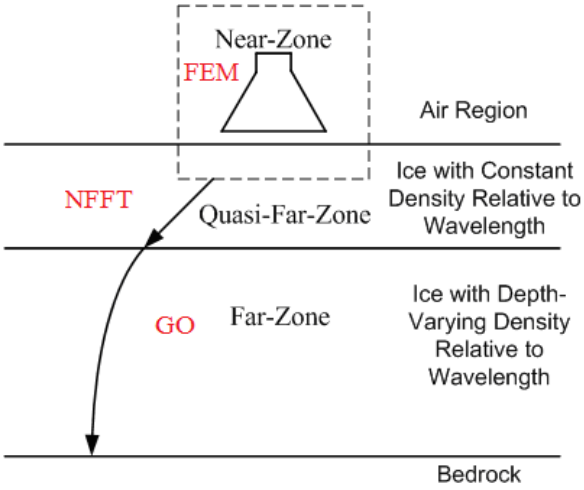

Figure 1.3 – The Three Field Regions

In this thesis, a solution is presented for determining the far-zone gain of antennas mounted at or near the surface of glacial ice. This technique handles the difficulties of analyzing complex antennas, as well as the gain-modifying properties of glacial ice. The electric and magnetic fields radiated by the antennas are divided into three regions: the near-zone, the quasi-far zone, and the far-zone. Shown in Figure 1.3 are the three regions, along with the respective technique used to determine the fields in that regions. The near-zone fields are determined using the FEM code HFSS. A dual-dielectric NFFT algorithm is used to solve the problem of the antenna being mounted above a half-space of ice. Then, a GO algorithm [46] is used to account for the depth-varying dielectric constant of the ice. Using the combined FEM-NFFT-GO algorithm, the far-zone antenna pattern at any depth within glacial ice can be determined.

1.6 Thesis Organization

The overall goal of this work is to determine the ice attenuation, and thus ice temperature, at any depth within glacial ice from radar returns. As stated previously, precise knowledge of the far-zone antenna gain is necessary to accurately determine the radar signal attenuation at each depth. Therefore, the majority of this work is devoted to determination of the far-zone antenna gain. A three-part hybrid technique was developed to determine the far-zone antenna gain, involving FEM, a near-to-far-field transformation (NFFT), and GO. FEM modeling using HFSS is discussed on its own in Chapter 2. Next, the FEM-NFFT-GO hybrid technique is discussed in Chapter 3. Results from both the FEM-NFFT and combined FEM-NFFT-GO technique are presented in Chapter 4. The proposed technique for determining temperature from radar returns and simulated results are discussed in Chapter 5. Finally, Chapter 6 discusses conclusions and future work. A full derivation of the dual-dielectric NFFT routine is presented in Appendix A. Also, the code used to implement the FEM-NFFT-GO routine is discussed in Appendix B. The code used for performing ice temperature extraction simulations in presented in Appendix C.

CHAPTER 2: Antenna Analysis Using HFSS

Full characterization of radar systems requires antenna analysis. One of the most popular antenna analysis tools is the commercial software Ansoft HFSS. Among other things, it is useful for determining input impedance, scattering parameters, and both near-zone and far-zone antenna patterns in free space. The code directly solves for the electric and magnetic near-zone field values in a solution space surrounding the geometry of interest (Figure 2.1) using the finite element method (FEM). The FEM is discussed in Section 2.1. Since field values determined within the solution space are often still in the near-zone, a near-to-far-field transformation (NFFT), performed in post-processing, is necessary to determine the free-space far-zone field values. Free-space antenna modeling using HFSS is presented in Section 2.2, and the HFSS NFFT for obtaining free-space far-zone field values is presented in Section 2.3.

With some modeling adjustments, HFSS can also be used to determine near-zone parameters for antennas located above glacial ice. Unfortunately, for reasons discussed in Section 2.4, the HFSS NFFT can not be used to transform these near-zone field values to the far-zone.

2.1 The Finite Element Method

The finite element method is a useful tool for solving vector electromagnetic wave equation boundary problems for complex radiating structures. Within a given solution space surrounding the radiating structure of interest, the FEM [39] code solves the 3D vector wave equations with given boundary conditions for a finite number of 3D elements, often tetrahedrons, which fill the solution space. Due to the relative accuracy and speed of the FEM for a variety of radiating structures [40], the method has found much commercial success in products such as Ansoft HFSS™ (high frequency structure simulator), a product often used by the Center for Remote

Sensing of Ice Sheets (CRESIS) for modeling antennas radiating in free space. In free space, the software provides accurate values for scattering parameters and input impedance. Also, through the use of a near-to-far-field transformation, HFSS is capable of generating far-zone radiation patterns in free-space. Additionally, due to the software's ability to model an arbitrary variety of materials, it is capable of accurately calculating near-field parameters for radiating structures located above glacial ice. However, even with the many post-processing features of HFSS, it is incapable of accurately determining far-zone radiation patterns for antennas located above a dielectric half-space such as glacial ice.

Although it is possible to have multiple materials within the software's finite solution space, it is impossible to model multiple materials outside of the solution space. When enclosing the solution space with any of the available boundary conditions (usually radiating boundary conditions are used), the code assumes the medium outside of the solution space is a homogeneous medium of the users choice. Therefore, since a dielectric half-space is infinite relative to the antenna, it is impossible to determine the far-zone radiation pattern of antennas located near a dielectric half-space, such as glacial ice.

Even though HFSS is incapable of determining far-field radiation patterns for antennas located near a dielectric half-space, it is still capable of determining accurate electric and magnetic near-field values, provided the modeled dielectric medium within the solution space is large enough relative to the antenna. Therefore, HFSS can be utilized in determining the electric and magnetic near-field values, a key step in solving the overall far-zone antenna gain determination problem.

2.2 Free-Space Antenna Modeling

When modeling antennas in free-space (or any homogeneous medium) with HFSS, the antenna is embedded in a finite solution space in which the wave equation

derived from the differential form of Maxwell's Equations is solved. In addition to other parameters, the size and material properties of the solution space require user specification. Other parameters requiring using specification are boundary conditions, port excitation, and solution set-up. Each of these specification requirements are discussed next.

2.2.1 The Solution Space

The antenna being modeled is embedded in the solution space and enclosed by a solution box as shown in Figure 2.1. The user can specify the solution space to have any material properties, including such parameters as permittivity, permeability, and loss tangent. Even anisotropic materials can be modeled in HFSS. Also, the solution space can be set to any geometry and size, but analysis time is directly linked to the size of the solution space. Usually, the solution space is rectangular, with a minimum size of a quarter wavelength at the frequency of interest [21].

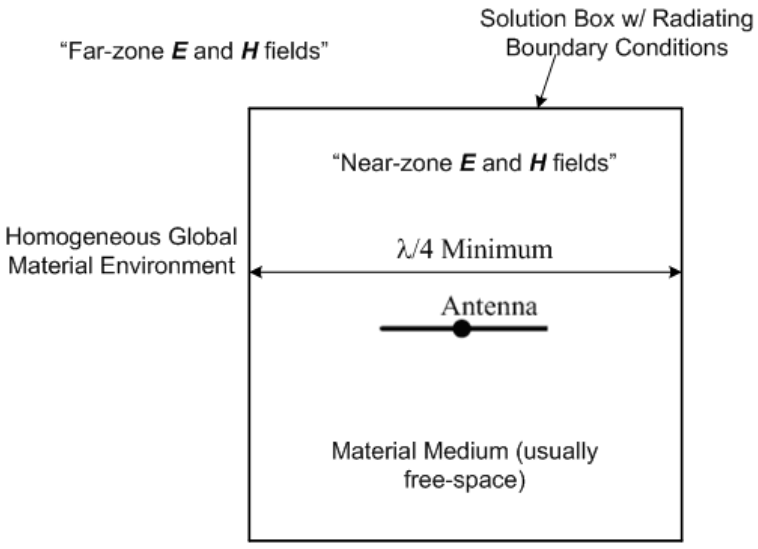

Figure 2.1 – Generic HFSS Modeling

2.2.2 Boundary Conditions

Due to discontinuities associated with the finite solution space, boundary conditions are required. This is because the fields are discontinuous along the boundaries, so the spatial derivatives can not be calculated directly. Therefore, user-specified boundary conditions are used to define the field behavior at the solution space boundaries [21].

For the case of a structure open to infinite space, two different types of boundaries are often utilized: radiation and PML (perfectly matched layer) boundaries. Although implemented differently, both radiation and PML boundaries achieve the same end result: making a finite solution space behave as if it were infinite. However, only radiation boundaries are discussed here, since due to ease of implementation, they are used more frequently. Figure 2.1 shows a generic HFSS simulation setup, utilizing a radiation boundary.

Radiation boundary conditions are also referred to as absorbing boundary conditions since the "system absorbs the wave at the radiation boundary, essentially ballooning the boundary infinitely far away form the structure and into space" [21]. Therefore, the radiation boundary is non-reflecting and enables a finite space to be treated as an infinite space.

2.2.3 Port Excitation

When using HFSS, antenna feeds are modeled as ports. A port is "a unique type of boundary condition that allows energy to flow into and out of a structure" [21]. HFSS uses an arbitrary port solver to determine the natural modes that can exist inside of a transmission structure having the same cross section as the port. Two types of ports are used in HFSS: wave ports and lumped ports.

With wave ports, the port is assumed to be connected to an infinitely long waveguide having the same cross-section and properties as the port. The wave port

solver determines the characteristic impedance, complex propagation constant, associated s-parameters of the port, and supports multiple modes. By default, the outer edge of a wave port is defined to have a “Perfect E boundary,” meaning that the port is enclosed inside of a perfect conductor, such as a waveguide. The perfect E boundary forces the electric field to be perpendicular to the boundary surface. Additionally, wave ports must always be directly connected to the solution box boundary, and lie on a planar surface. When specifying a wave port, the port location must overlap a 3-dimensional object. Figure 2.2 shows a picture of a waveport feeding a coaxial line. Also shown in Figure 2.2 is an integration line, which defines the positive direction at each port.

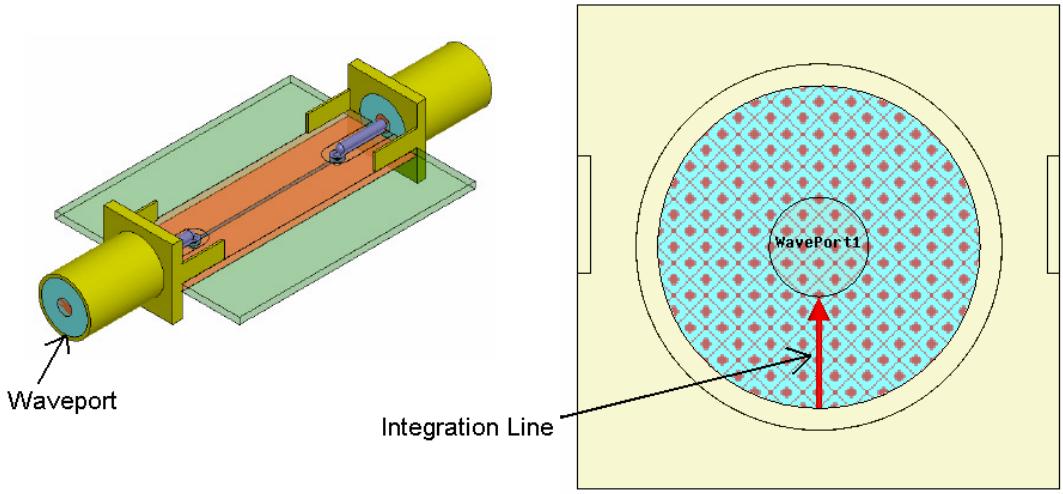

Figure 2.2 – Waveport Usage in Coax-to-Stripline HFSS Model

Lumped ports are used for driving sources internal to the solution box boundary. Unlike wave ports, lumped ports only support a single mode (TEM) and can be considered to be an ideal current source. Also, lumped ports use a perfect E boundary only along port edges that interface with conductors. All other edges of the port utilize “Perfect H boundaries,” which force the electric field to be tangential to

the port surface. When defining a lumped port, one specifies a 2-dimensional surface for the feed input, and defines an integration line, which is simply the direction of the current on that surface. Also, the characteristic impedance of the port is specified. Figure 2.3 shows a picture of a lumped port for feeding a dipole antenna.

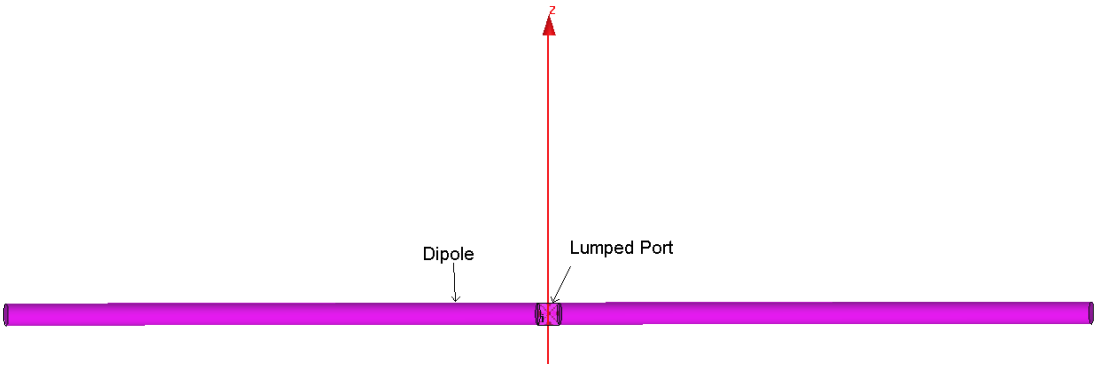

(a)

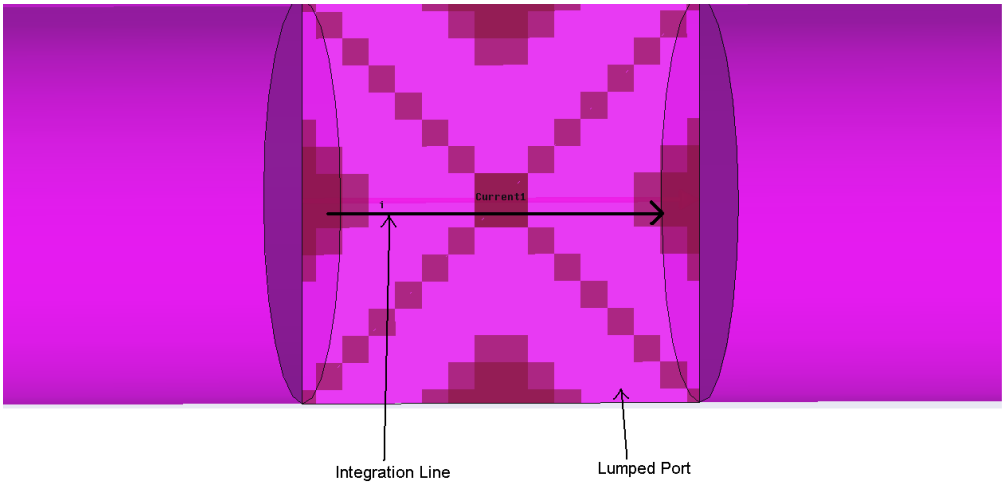

(b)

Figure 2.3 – Lumped Port Usage in Dipole HFSS Model

(a) Entire Dipole (b) Zoomed in on Port (Feed)

2.2.4 Solution Set-Up

The last required specification for analyzing structures using HFSS is the solution set-up. The minimum items required in the solution set-up are the solution frequency, maximum number of adaptive passes, and the parameter Delta S. The maximum number of adaptive passes and Delta S are both features of the adaptive solution process of HFSS.

HFSS uses adaptive meshing to analyze structures, where the mesh is a grid of tetrahedrons. Adaptive meshing works by searching for the largest gradients in the E-field throughout a region in the solution box, and adjusting the mesh accordingly with each subsequent adaptive pass. With each adaptive pass, HFSS compares the S-parameters from the current pass to those of the previous pass. If the maximum change in the S-parameters has changed by less than the user-defined "Delta S," or the maximum number of adaptive passes has been exceeded, the solution has converged. The default Delta S setting is 2%, and is recommended as sufficient by HFSS.

A useful optional input when adding a solution set-up is the frequency sweep, which allows for results to be determined for a range of frequencies in addition to the solution frequency. The converged mesh at the solution frequency is used to solve for the fields at the frequencies specified in the frequency sweep.

2.3 Far-Zone Field Calculations Using HFSS

The field values determined within the solution space are typically in the near zone, since the solution box is usually too small for fields to reach the far-zone. Therefore, HFSS incorporates a NFFT (near-to-far-field transformation) to determine far-zone field values. In order for HFSS to calculate meaningful far-zone field values, non-reflecting boundaries such as radiation or PML must be specified at the solution

box. This allows HFSS to make the finite solution space appear as an infinite one, since the non-reflecting boundaries absorb all incident radiation. Otherwise, any radiation incident on the boundaries would be reflected back, invalidating the near-zone field values. With this NFFT algorithm, near-zone field values sampled on the solution space boundary are converted to far-zone field values.

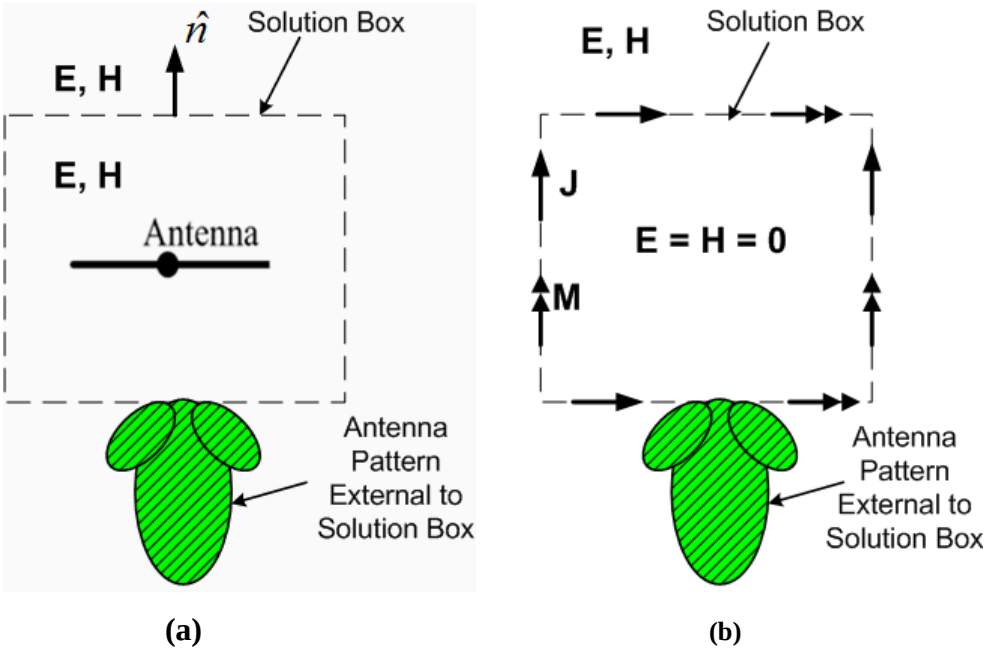

Figure 2.4 – Free-Space Equivalence
(a) Original Problem (b) Equivalent Problem

The HFSS NFFT algorithm makes use of the Schelkunoff Equivalence Principle [18] to replace the complicated geometry and associated near-zone fields inside the solution box with an equivalent structure that radiates the same far-zone fields external to the solution box as did the original geometry. Figure 2.4(a) shows an antenna residing in free-space. This figure shows the solution box surrounding the antenna on which the near-zone fields were calculated by HFSS, along with the (yet to be determined) far-zone pattern that the antenna radiates external to the solution

box. Figure 2.4(b) shows an electrically equivalent geometry. Here the radiating source (antenna) within the sampling surface is removed, and electric and magnetic surface currents are placed on the solution box, with values given by:

$$\mathbf{J} = \hat{n} \times \mathbf{H} \qquad \textbf{Eq. 2.1}$$

$$\mathbf{M} = \mathbf{E} \times \hat{n} \qquad \textbf{Eq. 2.2}$$

where **E** and **H** are the electric and magnetic fields originally present on the solution box surface, respectively, and the unit vector $\hat{n}$ is directed outward from the surface. According to the Schelkunoff Equivalence Principle [18], these currents generate the same fields outside the solution box as did the original radiating structure, and zero (null) fields inside the solution box.

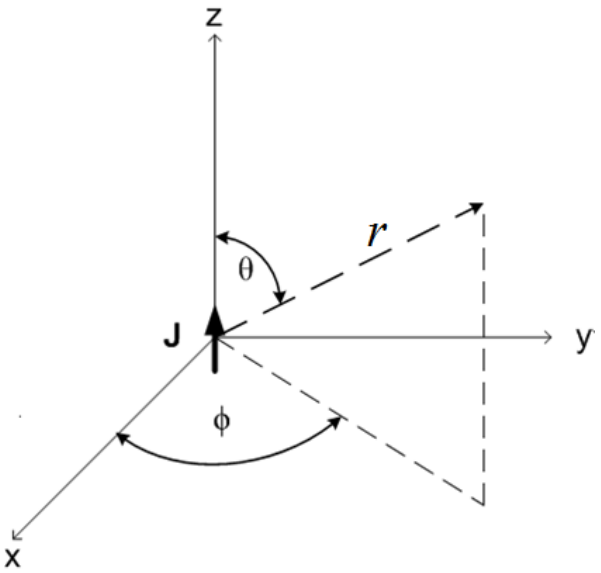

Figure 2.5 – Geometry for a z-Directed Hertzian Dipole

HFSS implements the NFFT by first sampling the electric and magnetic near-zone fields on the solution box boundary. Then, the near-zone fields are converted to

equivalent surface currents on a rectangular grid located on the solution box boundary. Each electric and magnetic current segment behaves as an infinitesimal (Hertzian) electric and magnetic dipole, respectively which radiates into a homogeneous environment.

The fields radiated by the equivalent currents are calculated using the well-known fields of a Hertzian dipole, such as the z-directed electric Hertzian dipole in Figure 2.5. The electric dipole shown in Figure 2.5 radiates the following theta and phi components of the electric field in the far-zone [4]

$$E_\theta^J(\theta,\phi) = \frac{jk\eta JwI\sin\theta}{4\pi}e^{-jkr} \qquad \textbf{Eq. 2.3}$$

$$E_\phi^J(\theta,\phi) = 0 \qquad \textbf{Eq. 2.4}$$

where *w* and *l* are the dimensions of the sampled electric current source *J*, and *r* is the distance from the origin to the point of observation. The observer is assumed to be located at coordinates θ and □ on a sphere located at infinity, which eliminates the range dependence *r* that would typically be in the denominator of Equation 2.3. Also, *k* is the lossless free-space wavenumber given by

$$k = 2\pi f\sqrt{\mu_f\varepsilon_f} \qquad \textbf{Eq. 2.5}$$

where f is the frequency in Hz, μ_f is the free-space magnetic permeability (4π x 10^{-7} H/m), and ε_f is the free-space electric permittivity (8.854 x 10^{-12} F/m). Also, η is the lossless free-space intrinsic impedance given by

$$\eta = \sqrt{\frac{\mu_f}{\varepsilon_f}} \qquad \textbf{Eq. 2.6}$$

Similarly, a z-directed magnetic current segment located at the origin radiates the following theta and phi components of the electric field in the far-zone [4]

$$E_\theta^M = 0 \qquad \textbf{Eq. 2.7}$$

$$E_\phi^M = \frac{jk\eta Mwl\sin\theta}{4\pi} e^{-jkr} \qquad \textbf{Eq. 2.8}$$

where M is the magnetic current source magnitude.

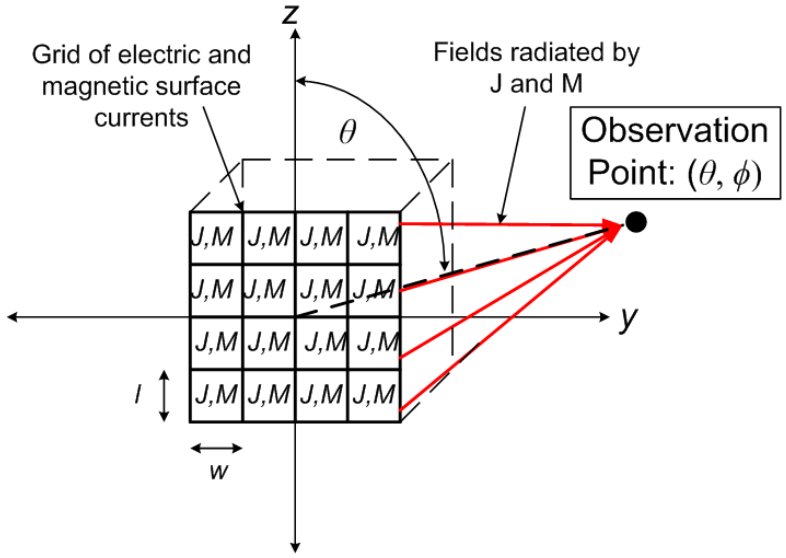

Figure 2.6 – NFFT Superposition from a Single Surface of Current Segments

Figure 2.6 shows a grid of electric and magnetic surface currents, J and M on a single surface. Each current radiates a theta or phi polarized electric field, described by Equations 2.3 through 2.8, towards the far-zone observation point at coordinates θ and □. The total far-zone theta and phi components of the electric field are simply the superposition of all of the far-zone electric fields radiated by the individual current

segments. For a surface such as that shown in Figure 2.6, the total field is calculated by

$$E_\theta^T(\theta,\phi) = \sum_{m=1}^{M}\sum_{n=1}^{N}\left[E_\theta^J(n,m,\theta,\phi) + E_\theta^M(n,m,\theta,\phi)\right] \qquad \textbf{Eq. 2.10}$$

$$E_\phi^T(\theta,\phi) = \sum_{m=1}^{M}\sum_{n=1}^{N}\left[E_\phi^J(n,m,\theta,\phi) + E_\phi^M(n,m,\theta,\phi)\right] \qquad \textbf{Eq. 2.11}$$

where the indexes *N* and *M* represent the number of rows and columns for which the surface has been discretized into surface currents *J* and *M.*

2.4 Modeling Antennas above a Half-Space of Glacial Ice

The procedure presented in Sections 2.2 and 2.3 is sufficient to model radiating structures in free-space or some other homogeneous medium. However, in remote sensing of polar ice sheets, antennas radiate into a half-space of glacial ice. This affects all characteristics of the antenna, including its input impedance, near-zone fields, and far-zone fields. With some modeling adjustments (Section 2.4.1), near-zone fields and input impedance can still be obtained. In fact, these HFSS modeling adjustments have been routinely performed at CRESIS for obtaining the input impedance of ice-mounted antennas. However, true far-zone fields can not be obtained using HFSS alone.

2.4.1 HFSS Modeling Adjustments for Antennas Near Glacial Ice

The process of modeling antennas near a dielectric half-space in HFSS is similar to the generic modeling described in Sections 2.2. However, now, some of the material representing the half-space must be placed within the solution box in order to

model the effects of the half-space on near-zone antenna phenomena. Also, additional requirements are placed on the size of the solution box, which are listed in Table 2.1. When modeling a dielectric half-space in HFSS, the solution box size must be increased to at least the minimum size of 2λ, compared with a minimum size of λ/4 for the homogeneous medium case. Experimental evidence has shown that this increase in solution box size is required to obtain accurate near-zone fields. Figure 2.7 displays a generic antenna modeled near a half-space of ice, incorporating the requirements from Table 2.1. Note that when modeling antennas mounted above a dielectric half-space, HFSS is capable of determining accurate near-zone fields, but not far-zone fields.

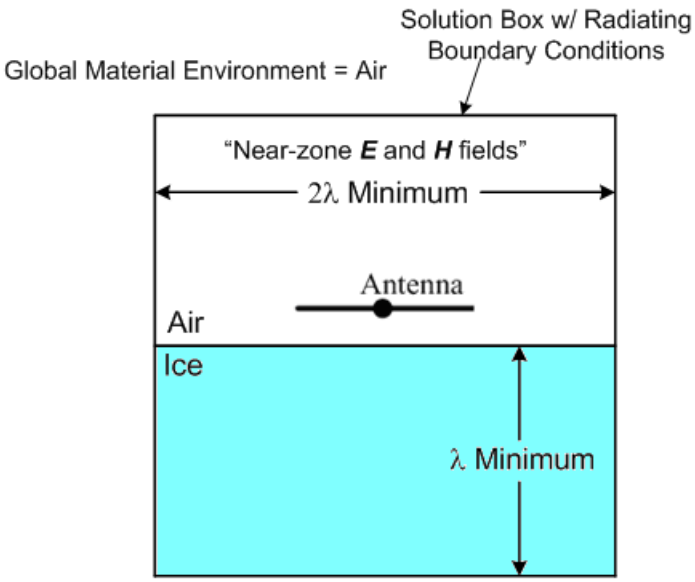

Figure 2.7 – HFSS Modeling Near a Half-Space

Table 2.1 – HFSS Modeling Requirements Near Glacial ice

Boundary Conditions:	Radiating
Square Solution Box Dimension:	2λ minimum
Ice Half-space Dimension:	λ minimum

2.4.2 What HFSS Will Let You Do Even Though It Is Incorrect!

Although it is impossible to obtain correct far-zone antenna patterns for ice-mounted antennas using HFSS alone, HFSS will not prevent users from trying. As discussed in Sections 2.2 and 2.3, HFSS can only correctly perform its NFFT algorithm into a homogeneous infinite medium, specified by the global material environment (GME). Therefore, the NFFT algorithm used by HFSS is useless for far-zone radiation into anything other than a homogeneous medium. That being said, HFSS will not prevent the user from generating incorrect far-zone field results.

A theory proposed by an HFSS employee for possibly obtaining nearly correct far-zone fields within air or ice involved adjustment of the GME. He suggested that modeling the antenna above glacial ice, but setting the GME to air or ice, depending on the observer's location, would produce nearly correct far-zone fields within air or ice, respectively.

The E-plane far-zone fields resulting from such a procedure are presented in Figure 2.8, for an ice-mounted horizontal Hertzian dipole. In Figure 2.8(a), the GME is air, and Figure 2.8(b), the GME is ice. Also shown in Figure 2.8 is the exact result [40] for a horizontal Hertzian dipole located above a half-space of glacial ice. Both of the results obtained from HFSS disagree dramatically with the true result, indicating that true far-zone fields for ice-mounted antennas can not be obtained using HFSS alone.

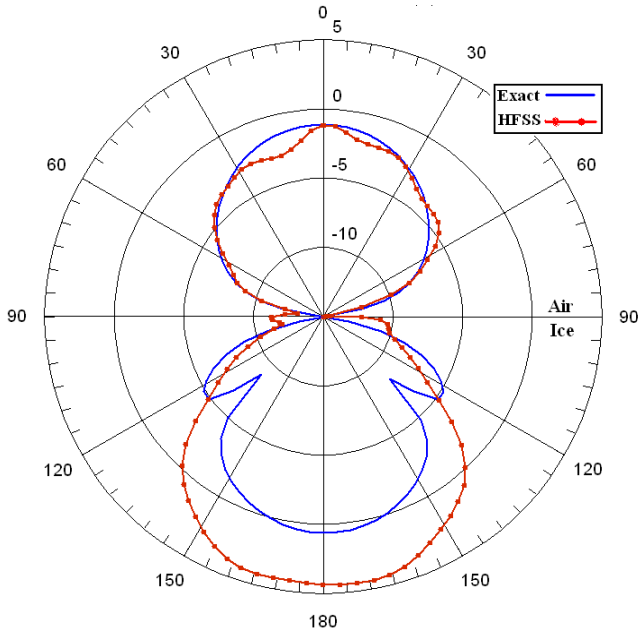

(a)

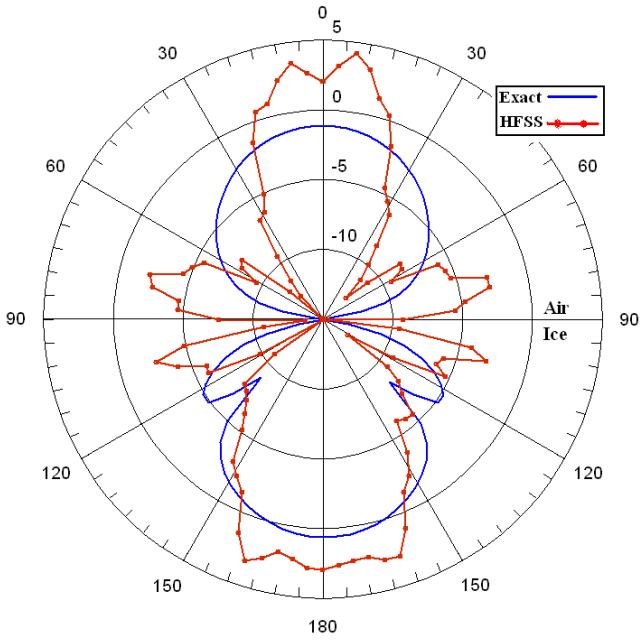

(b)

Figure 2.8 – Far-Zone E-plane for Horizontal Hertzian Dipole Mounted Above Glacial Ice from HFSS (dB)

(a) GME = Air (b) GME = Ice

2.5 HFSS Modeling Summary

In the context of modeling antennas near glacial ice, HFSS is only useful for determining near-zone fields and input impedances, and this requires the modeling technique discussed in Section 2.4. Also, although HFSS allows the calculation of far-zone fields, these results are incorrect for ice-mounted antennas. The inability of HFSS to determine far-zone fields for ice-mounted antennas is due to the HFSS NFFT only being capable of transforming near-zone fields to a homogeneous far-zone. In order to determine true far-zone fields, a custom NFFT is required, which is discussed in Chapter 3. In this custom NFFT, the near-zone fields calculated in HFSS are sampled and exported to memory. These near-zone fields are then converted to a series of equivalent radiating current filaments. The NFFT algorithm allows the currents to radiate essentially in an infinite half-space, allowing for the determination of accurate Green's functions associated with the current filaments.

CHAPTER 3: Far-Zone Field Patterns in Glacial Ice

In order to accurately determine glacial ice temperature profiles from radar returns, accurate far-zone antenna gain estimation is required. Typically, far-zone antenna gain is determined using commercial software such as HFSS. However, due to the complicated properties of glacial ice, these commercial software packages are incapable of determining the far-zone gain for ice-mounted antennas (see Chapter 2). This chapter presents a new hybrid technique for determining the far-zone gain of glacial ice-mounted antennas, which addresses the problem by dividing the geometry into three regions: the near-zone, the quasi-far-zone, and the far-zone. Fields in the near-zone are determined using the finite element method (FEM) via HFSS. In the quasi-far-zone, which is the region just below the surface of the ice where the wavefronts are planar, the fields are determined using a near-to-far-field transformation (NFFT). In the far-zone, which is the region starting just below the quasi-far-zone and ending at bedrock, fields are determined using geometric optics ray tracing (GO). The combined three-part non-iterative hybrid technique is called the FEM-NFFT-GO technique.

The basic theory of this technique is presented in Section 3.1. Also, the practical aspects of the technique, as well as the operation of the FEM-NFFT-GO software are presented in Section 3.2.

3.1 Background for the FEM-NFFT-GO Technique

The FEM-NFFT-GO technique involves three steps: the FEM modeling of the antenna above the upper layer of glacial ice to obtain electric and magnetic near-zone field values, the transformation (NFFT) from the near-zone to the quasi-far-zone (a few wavelengths below the air/ice interface), and the projection of the quasi-far-zone fields to any depth within the non-uniform glacial ice (GO). The three regions (near-

zone, quasi-far-zone, and far-zone) are depicted in Figure 3.1, where an antenna is mounted near an air/ice interface.

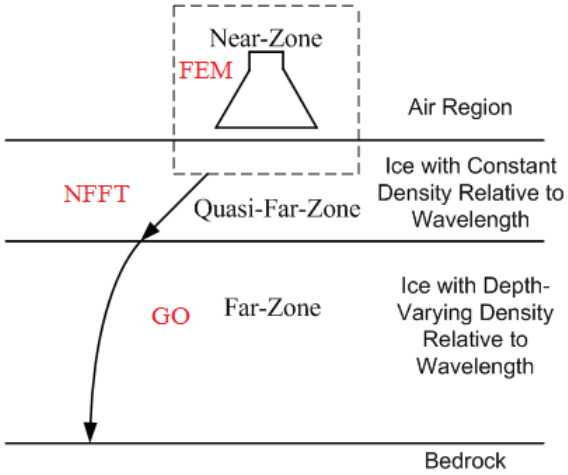

Figure 3.1 – The Three Field Regions

3.1.1 Far-Zone Fields within Uniform Glacial Ice

The quasi-far-zone, shown in Figure 3.1, is assumed to be a relatively uniform region that is deep enough (a couple wavelengths from the air/ice interface) for fields within the region at VHF frequencies to be considered planar. Far-zone fields in this region are determined using the FEM-NFFT routine. Since the FEM was largely discussed in Sections 1.3 and Chapter 2, it will not be discussed here. Also, in Section 2.2, an NFFT for homogeneous backgrounds was discussed. Therefore, this section is primarily devoted to discussing a dual-dielectric NFFT algorithm, which is used for determining far-zone fields in uniform glacial ice.

The dual-dielectric NFFT is more complicated than the HFSS NFFT, since in addition to utilizing the electromagnetic equivalence theorem; it also utilizes the electromagnetic reciprocity theorem [18]. Although equivalence was discussed in Section 2.3 for homogeneous backgrounds, it is briefly discussed here in relation to a

dielectric half-space. The reciprocity theorem is unique to the dual-dielectric NFFT and is discussed in detail.

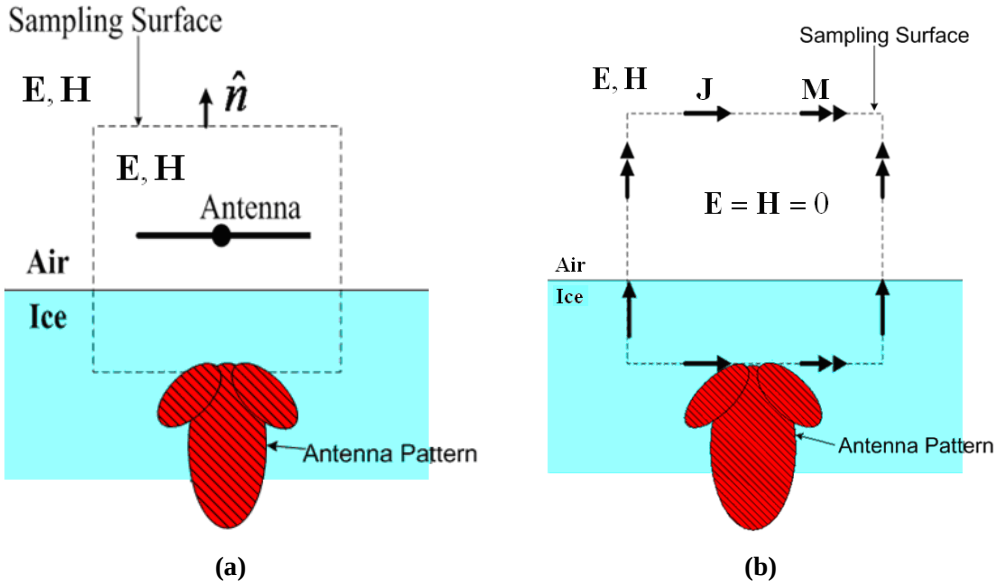

Figure 3.2 – Equivalence for a Half-Space of Glacial Ice
(a) Original Problem (b) Equivalent Problem

Figure 3.2 shows how the equivalence principle is used in the dual-dielectric NFFT. An antenna mounted above a homogeneous half-space of ice is shown in Figure 3.2(a). This figure shows the sampling surface on which the near-zone fields were calculated by HFSS, along with the (yet to be determined) quasi-far-zone pattern radiated by the antenna below the air/ice interface. Note that in Figure 3.2(a), the near-zone fields are sampled on a sampling surface, rather than the solution box as is done by the HFSS NFFT algorithm (shown in Figure 2.2(a)). Thus, one major difference between the HFSS NFFT and the dual-dielectric NFFT is the ability to sample near-zone field values at an arbitrary sampling location.

Figure 3.2(b) shows an electrically equivalent geometry to Figure 3.2(a). Here the antenna is removed, and electric and magnetic surface currents, with values given

by Equations 2.1 and 2.2, are placed on the sampling box. As was shown in Section 2.3, the superposition of the fields radiated by these currents generates the same total electric and magnetic fields outside the sampling box as did the original radiating structure, and zero (null) fields inside the sampling box.

The calculation of the fields radiated by these equivalent electric and magnetic surface currents is straightforward when the background medium is free space, but the presence of the air/ice boundary presents a more difficult problem. A general solution involves the decomposition of the spherical waves emanating from the currents into a spectrum of plane waves, whose reflections from and transmission through the dielectric interface can be determined from the Fresnel reflection and transmission coefficients. However, when the observer is electrically far from the boundary (as in the case of the quasi-far-zone), the reciprocity principle can be used to simplify the analysis [38]. For this case, only the geometric optics waves – those obeying Snell's law – need be considered.

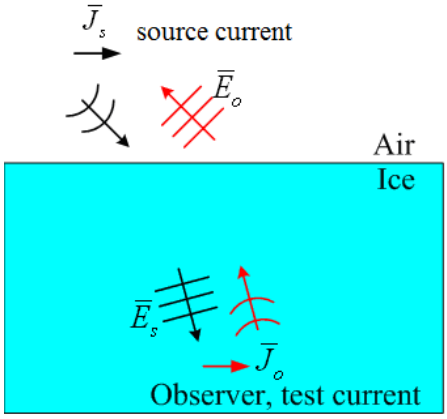

Figure 3.3 – Reciprocity for a Half-Space of Glacial Ice

Reciprocity states that the response of a system to a source is unchanged when source and observer are interchanged [18]. Figure 3.3 shows this reciprocal relationship between a source current $\bar{J}_s$ and an observer's test current $\bar{J}_o$, where the observer is assumed to be located in the far-zone a couple wavelengths from the

air/ice interface. Fields transmitted by the source current are in black, and those fields transmitted by the observer's test current are in red. The field transmitted by the observer's test current is planar within the vicinity of the air/ice interface, whereas the field transmitted by the source antenna is not yet planar in the vicinity of the air/ice interface. Therefore, reciprocity can be used to describe $\overline{E}_s$ (electric field due to the source current at the point of observation) in terms of the field $\overline{E}_o$ (electric field due to the observer test current near the air/ice interface), which is a plane wave. The derivation and presentation of these plane wave formulas is presented in Appendix A. Also, Appendix A provides a thorough description of all the supplementary formulas and variable descriptions necessary for coding the dual-dielectric NFFT routine.

The total quasi-far-zone electric field at any pair of observation angles θ and is the superposition of the electric fields radiated by each electric and magnetic current source along the sampling box, determined by the formulas presented in Appendix A. Recalling that the near-zone field sampling box is rectangular, there are six two-dimensional surfaces on which electric and magnetic current sources exist. When the source and observer are in different mediums, the sum of total parallel and perpendicular polarized electric fields radiated from a surface are found by

$$E^{T}_{\theta Surf}\left(i,\theta,\phi\right)=\sum_{m=1}^{M}\sum_{n=1}^{N}\left[E^{Ti}_{\theta E}(m,n,\theta,\phi)+E^{Ti}_{\theta M}(m,n,\theta,\phi)\right] \qquad \textbf{Eq. 3.1}$$

$$E^{T}_{\phi Surf}\left(i,\theta,\phi\right)=\sum_{m=1}^{M}\sum_{n=1}^{N}\left[E^{Ti}_{\phi E}(m,n,\theta,\phi)+E^{Ti}_{\phi M}(m,n,\theta,\phi)\right] \qquad \textbf{Eq. 3.2}$$

where i is index representing the surface, M and N are the number of surface currents in each of the two dimensions of the surface, and $E^{T}_{\theta Surf}$ and $E^{T}_{\phi Surf}$ are the parallel and perpendicular components of the transmitted electric field radiated by the surface i. When the source and observer are located in the same medium, the sum of total parallel and perpendicular polarized electric fields radiated from a surface are

$$E_{\theta Surf}^{RI}\left(i,\theta,\phi\right)=\sum_{m=1}^{M}\sum_{n=1}^{N}\left[E_{\theta E}^{Ii}(m,n,\theta,\phi)+E_{\theta E}^{Ri}(m,n,\theta,\phi)+E_{\theta M}^{Ii}(m,n,\theta,\phi)+E_{\theta M}^{Ri}(m,n,\theta,\phi)\right]$$

Eq. 3.3

$$E_{\phi Surf}^{RI}\left(i,\theta,\phi\right)=\sum_{m=1}^{M}\sum_{n=1}^{N}\left[E_{\phi E}^{Ii}(m,n,\theta,\phi)+E_{\phi E}^{Ri}(m,n,\theta,\phi)+E_{\phi M}^{Ii}(m,n,\theta,\phi)+E_{\phi M}^{Ri}(m,n,\theta,\phi)\right]$$

Eq. 3.4

where $E_{\theta Surf}^{RI}$ and $E_{\phi Surf}^{RI}$ are the parallel and perpendicular components of the combined incident and reflected electric fields radiated by the surface *i*. Finally, the total electric far-fields at each pair of observation angles due to the contribution of all sampled surfaces are

$$E_{\theta}^{Total}\left(\theta,\phi\right)=\sum_{i=1}^{6}\left[E_{\theta Surf}^{T}\left(i,\theta,\phi\right)+E_{\theta Surf}^{RI}\left(i,\theta,\phi\right)\right]$$

Eq. 3.5

$$E_{\phi}^{Total}\left(\theta,\phi\right)=\sum_{i=1}^{6}\left[E_{\phi Surf}^{T}\left(i,\theta,\phi\right)+E_{\phi Surf}^{RI}\left(i,\theta,\phi\right)\right]$$

Eq. 3.6

Antenna patterns are often presented as gain relative to an isotropic radiator, which is given by the following expressions

$$G_{\theta o}(\theta,\phi)=\frac{2\pi\left|E_{\theta}^{Total}\left(\theta,\phi\right)\right|^{2}}{\eta_{o}}$$

Eq. 3.7

$$G_{\phi o}(\theta,\phi)=\frac{2\pi\left|E_{\phi}^{Total}\left(\theta,\phi\right)\right|^{2}}{\eta_{o}}$$

Eq. 3.8

where η_o is the intrinsic impedance of the medium containing the observer. For antenna patterns located above the air/ice interface, the intrinsic impedance is that of free-space (377 Ω), whereas for antenna patterns located below the air/ice interface, the intrinsic impedance is that of the upper-layer of ice (280 Ω).

3.1.2 Far-Zone Fields within Non-Uniform Glacial Ice

The non-uniform region of glacial ice, called the far-zone, is shown in Figure 3.1. This region extends from the quasi-far-zone to bedrock. As shown in Figure 3.1, rays propagating toward the bedrock are continuously refracted towards the normal direction in this region due to the depth-dependent density of glacial ice. This refractive gain must be accounted for if ice attenuation is to be accurately measured from radar sounding. Fortunately, the GO (geometric-optics ray tracing) technique can be used to determine the refractive gain. But, to be useful, the GO technique requires knowledge of the density profile causing the refractive gain.

Ice core data taken from Greenland and Antarctica have resulted in empirical ice density models that agree well with measured results [3, 10, and 43]. Combining the empirical ice density model with GO allows for the effect of depth-varying ice density on the far-zone antenna gain to be determined. Since the GO technique depends on both glacial ice density modeling and geometric optics, both are presented in this section.

3.1.2.1 Glacial Ice Empirical Density Model

Generally, ice density (and other constitutive parameters) varies as a function of depth only [20]. Near the surface, the ice is intermixed with air bubbles yielding a density less than that of pure ice [34], where the density of pure ice P is 0.92 g/cm^3. As the depth increases, the pressure due to the mass of ice above compresses the ice, thus reducing the volume of the air bubbles until the pure ice density is achieved. This compression occurs for roughly the first 100 meters of ice. An accurate model for the ice density is given by the following relation [37]

$$\rho = P - Ve^{Rz} \qquad \textbf{Eq. 3.9}$$

where z is the ice depth, and V and R are empirical constants. The values of V and R for Byrd Station in western Antarctica [10] and from the GISP2 [14 and 43] ice core from Summit Station, Greenland are shown in Table 3.1. The empirical relationship of Equation 3.9 using the constants shown in Table 3.1 provides a coefficient of determination of over 0.99. Also, presented in Figure 3.4 is glacial ice density in Antarctica and Greenland using Equation 3.9. Notice that near 100 m in depth, the density comes very close to that of pure ice. Also notice the subtle differences in density profile between Byrd Station in Antarctica and Summit Station in Greenland. This makes it evident that a density profile corresponding to the exact geographic location of interest is desirable when using the FEM-NFFT-GO technique to obtain the most accurate results.

Table 3.1 -- Ice Density Empirical Constants

	Antarctica	Greenland
V:	0.52	0.55
R:	-0.033	-0.022

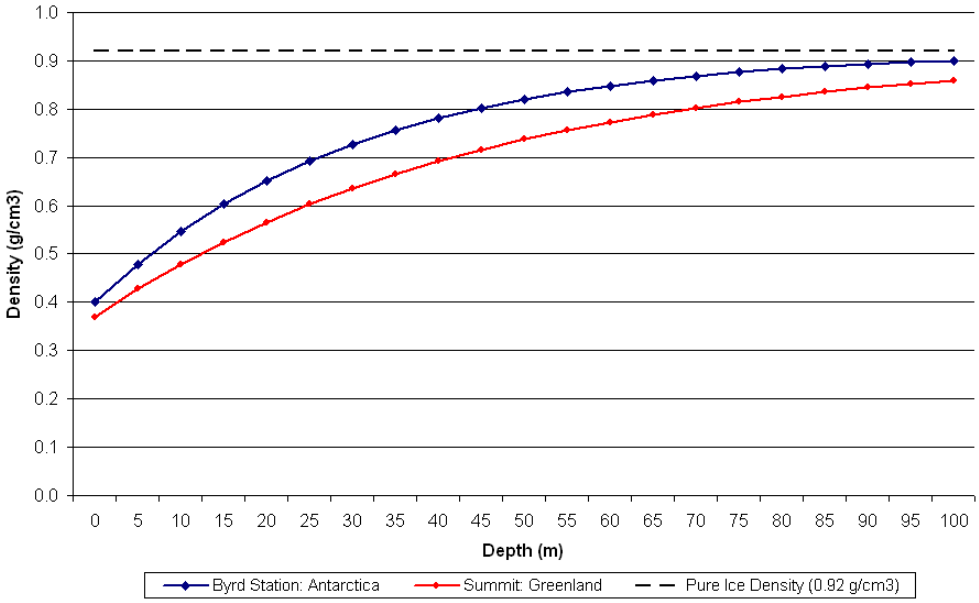

Figure 3.4 – Glacial Ice Density vs. Depth: Empirical Models

Also introduced by Robin [37] was the following empirical relationship between the glacial ice index of refraction and glacial ice density,

$$n = 1 + a\rho \qquad \textbf{Eq. 3.10}$$

where a is equal to 0.854. Recall that for non-magnetic media, the index of refraction is related to the dielectric constant via the following

$$n = \sqrt{\varepsilon_r} \qquad \textbf{Eq. 3.11}$$

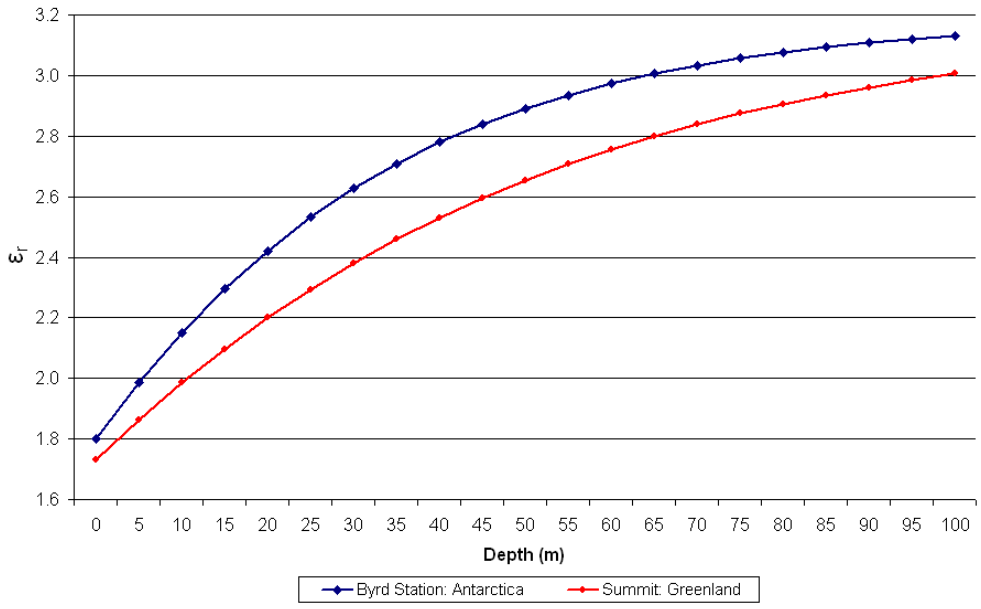

Figure 3.5 – Glacial Ice Dielectric Constant vs. Depth: Empirical Models

Although the FEM-NFFT portion of the technique (Appendix A) is discussed in terms of ε_r, (dielectric constant) the geometric optics relationships described here are more eloquently presented in terms of index of refraction. Also, in general, with high

frequency approximations such as geometric optics ray tracing, the index of refraction is used. Figure 3.5 shows the relationship between ε_r and depth using Equation 3.10 and 3.11. Notice that in both Antarctica and Greenland, the change in ε_r with depth begins to level off near 100 m in depth.

3.1.2.2 Geometric Optics Ray Tracing

Although geometric optics ray-tracing is often thought of at optical frequencies, it can also be used at the VHF frequencies used by ice-penetrating radars. The key point to consider when applying geometric optics is the relation of size and curvature of wavefronts to wavelength [36]. The electromagnetic fields a couple wavelengths into the upper-ice region (i.e. the quasi-far-zone) can be considered locally as propagating rays with planar wavefronts [46], indicating essentially no wavefront curvature, and the size of the wavefront is much larger than the wavelength. At greater depths, the ice density increases slowly compared to wavelength for VHF radars, so reflections are minimal [25], and the ray paths are bent increasingly toward the normal direction. From these ray trajectories the antenna gain at any depth can be determined.

The geometric depiction of ray bending occurring within the ice is presented in Figure 3.6. In Figure 3.6(a), a constant energy ray tube extending from a point source is propagating in a continuous medium, where the ray tube energy is focused on the area *dA*, at a distance *D* from the source. Figure 3.6(b) depicts the case where the mediums refractive index increases gradually with depth, and the constant energy ray tube is focused on the area *dA'*, located at the same distance *D* from the source. The area *dA'* in Figure 3.6(b) is less than the area *dA* in Figure 3.6(a). Therefore, the energy per unit area is increased for the case of gradually increasing dielectric constant, leading to an increased far-zone antenna gain in the medium having the dielectric constant-gradient.

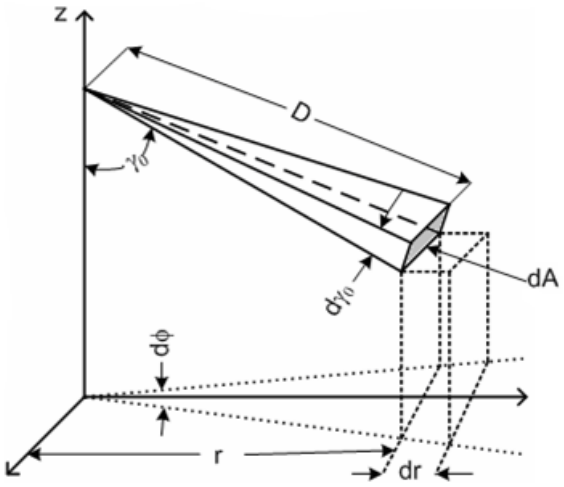

(a)

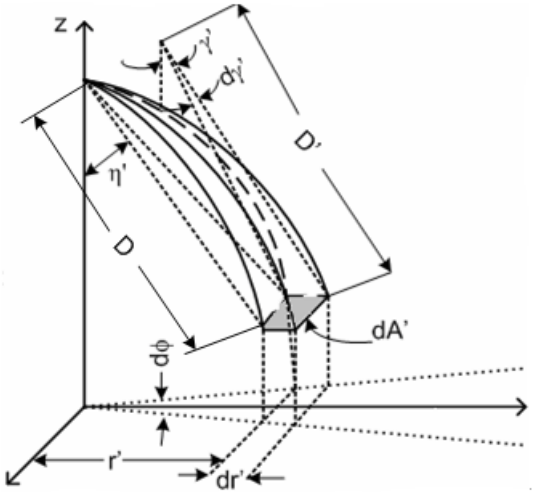

(b)

Figure 3.6 – Geometric Optics Ray Tracing – Constant Energy Tubes
(a) No Ray Bending (b)Ray Bending [45]

West and Demarest [46] reported the following relations for determining the far-zone antenna gain $G(z,\eta')$ as a function of depth and effective look angle

$$G(z,\eta') = G_0(\gamma_0,\phi)G_f(z,\eta') \qquad \textbf{Eq. 3.12}$$

where G_o is the quasi-far-zone gain in the upper region of glacial ice (relative to a free-space isotropic radiator), which is the result of the FEM-NFFT technique. Also, G_f is the gain factor improvement due to ray bending. The effective look angle η' is given by

$$\eta' = \tan^{-1}\left(\frac{r'}{z}\right) \qquad \textbf{Eq. 3.13}$$

where *r'* is the radial distance traveled by the ray beginning at the surface, as shown in Figure 3.6(b) and *z* is the depth within the ice. From geometric optics [46], the gain improvement factor is given by

$$G_f(z,\eta') = \frac{dA}{dA'} = \frac{D^2 \sin\gamma_0}{r'\dfrac{dr'}{d\gamma_0}\cos\gamma'} \qquad \textbf{Eq 3.14}$$

Here, γ_0 is the angle the ray makes with the normal as it is launched at the surface, *D* is the direct distance from the ray location at depth *z* from the starting location, and γ' is the angle the ray makes with the normal at any depth. The parameters *D* and γ' are given by

$$D = \sqrt{(r')^2 + z^2} \qquad \textbf{Eq. 3.15}$$

$$\gamma' = \sin^{-1}\left(\frac{n_i}{n}\sin\gamma_0\right) \qquad \textbf{Eq. 3.16}$$

Another key parameter found in Equation 3.14 is

$$r' = \int_0^z \frac{c}{\sqrt{n^2(z) + c^2}}\,dz \qquad \textbf{Eq. 3.17}$$

which is the radial distance traveled by a ray beginning at the surface, where $n(z)$ is the refractive index as a function of depth, and

$$c = n_0 \sin \gamma_0 \qquad \textbf{Eq. 3.18}$$

As stated in Section 3.1.2.1, glacial ice density profiles are often described by the following exponential relationship [37],

$$\rho(z) = P - Ve^{Rz} \qquad \textbf{Eq. 3.19}$$

$$n(z) = 1 + a\rho(z) \qquad \textbf{Eq. 3.20}$$

where the ice density ρ is now presented as a function of depth.

Making use of the exponential density profile described in Equations 3.19 and 3.20, and integrating Equation 3.17 yields the following result for the radial distance traveled by a ray at any depth

$$r' = \frac{-c}{R\sqrt{W}} \log\left[\frac{2\sqrt{WY} + 2W + X}{e^{Rz}\left(2\sqrt{WY_0} + 2W + X_0\right)} \right] \qquad \textbf{Eq. 3.21}$$

Differentiating Equation 3.21 with respect to γ_0 and then integrating with respect to z yields the following result

$$\frac{dr'}{d\gamma_0} = r' n_0 \cos\gamma_0 \left(\frac{1}{c} + \frac{c}{W}\right) + \frac{n_0 \cos\gamma_0}{RW}\left[\frac{\frac{X}{2} + W + 2c^2}{\sqrt{Y}} - \frac{\frac{X_0}{2} + W + 2c^2}{\sqrt{Y_0}} \right] \qquad \textbf{Eq. 3.22}$$

where,

$$W = 1 + 2aP + a^2P^2 - c^2 \qquad \textbf{Eq. 3.23}$$

$$X = \left(-2a^2PV - 2aV\right)e^{Rz} \qquad \textbf{Eq. 3.24}$$

$$Y = a^2V^2e^{2Rz} + X + W \qquad \textbf{Eq. 3.25}$$

$$X_0 = -2a^2PV - 2aV \qquad \textbf{Eq. 3.26}$$

$$Y_0 = a^2V^2 + X + W \qquad \textbf{Eq. 3.27}$$

Although an exponential density profile was assumed in the derivation of Equation 3.21 and 3.22, any density profile could be used in conjunction with the geometric optics ray tracing technique. However, this would require either numerical calculation of r' and $\frac{dr'}{d\gamma_0}$, or another closed form derivation of these parameters.

3.2 Using the FEM-NFFT-GO Technique to Determine Far-Zone Electric Fields

In this section, the practical aspects of running the FEM-NFFT-GO technique are presented, as well as some of the practical aspects used in creating the routine. Regarding the FEM-NFFT procedure, these include near-zone-field sampling, sampling location, and sampling resolution. Also presented is the procedure for actually running the FEM-NFFT-GO routine using the *Master.m* Matlab script. The Matlab script keeps most of the inner-workings of the routine hidden from the user, so these inner-workings are left for Appendix B.

3.2.1 Sampling and Exporting Near-Zone Fields

HFSS has a useful built-in feature called the vector field calculator. This allows for the performance of mathematical operations, as well as exportation of data, on all saved field data in the modeled geometry [22]. It also allows for certain types of data to be imported into HFSS. The Fields Calculator is easily accessed from the

main HFSS toolbar, by clicking HFSS < Fields < Calculator. Figure 3.7 displays the Fields Calculator window for HFSS v. 10.

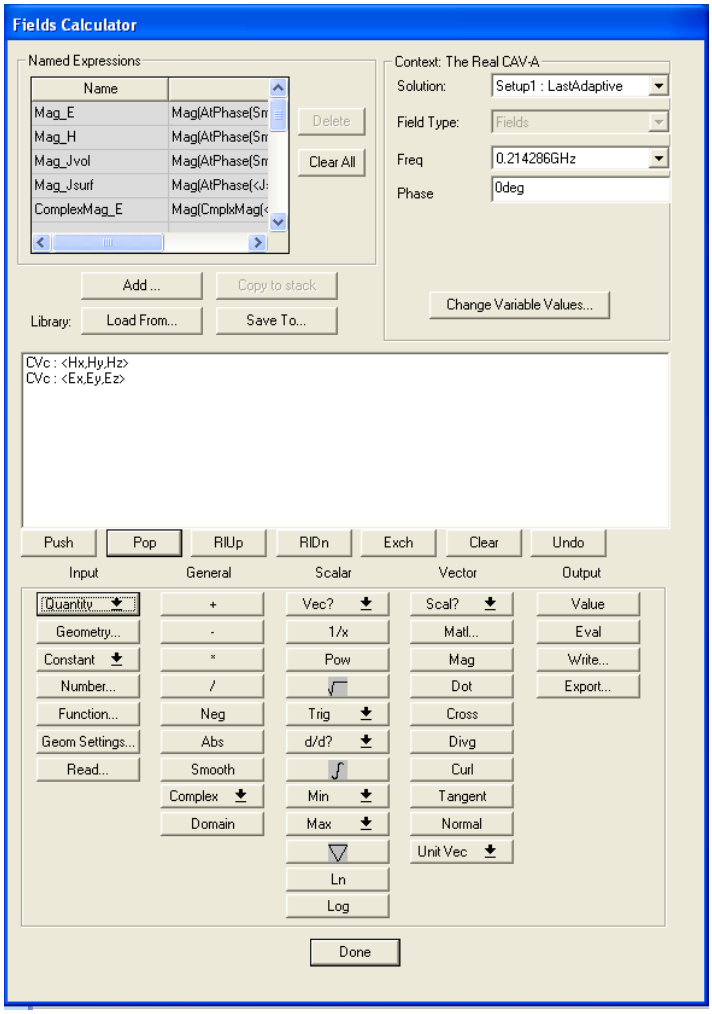

Figure 3.7 – HFSS v. 10 Fields Calculator

For the purposes of this work, only exportation of the vector Cartesian complex electric and magnetic near zone fields is of interest. This is easily accomplished by selecting Quantity < E and then Quantity < H in the Fields Calculator window shown in Figure 3.7, which also shows the E and H fields added

to the display. Once the E and H fields have been added to the Fields Calculator display, they are exported by using the Export command displayed in Figure 3.7. Once the Export command has been pressed, the window shown in Figure 3.8 is displayed. Exportation of field data requires the specification of an output file name (shown as *dataOut.txt* in Figure 3.8), and the input of a *.pts* file (shown as *samplingPoints.pts* in Figure 3.8), which specifies the three dimensional grid on which to sample near-zone field data.

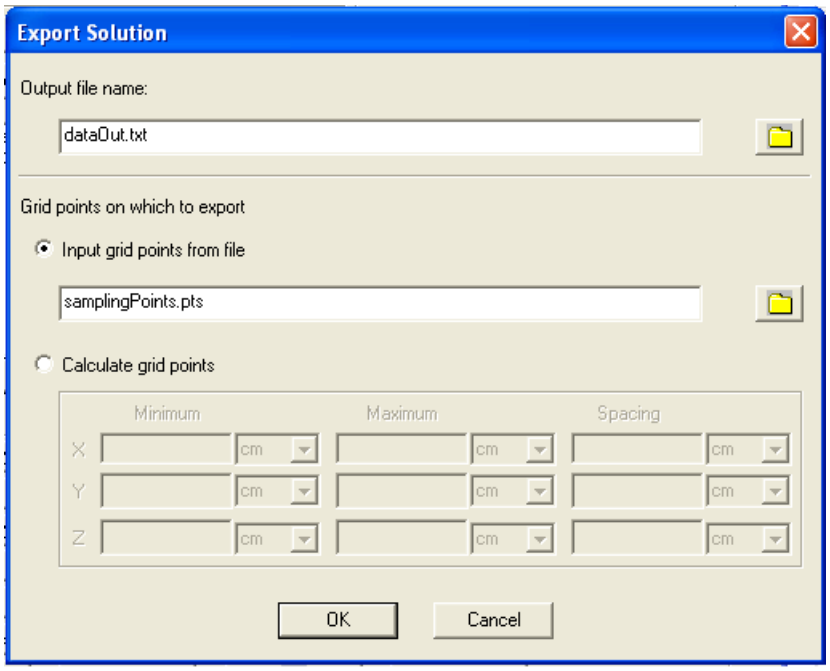

Figure 3.8 – HFSS v. 10 Fields Calculator Export Solution Window

The output data file contains the vector Cartesian electric or magnetic near-zone fields sampled on a grid specified by the *.pts* file. The output ASCII text file is in the format specified by Table 3.2, where *F* represents the field value, either E or H. The ASCII text file is then easily imported by Matlab for further processing.

Table 3.2 – HFSS Vector Cartesian Field Value Output File Format

Column 1	Column 2	Column 3	Column 4	Column 5	Column 6	Column 7	Column 8	Column 9
x-position	y-position	z-position	Real[F(x)]	Imag[F(x)]	Real[F(y)]	Imag[F(y)]	Real[F(z)]	Imag[F(z)]

The input *.pts* file contains the list of Cartesian coordinates in three dimensions on which the near-zone field values are sampled. The *.pts* file extension is recognized by HFSS as being a "Point File," which lists points in Cartesian coordinates in the following format shown in Table 3.3.

Table 3.3 – HFSS Points File Format

Column 1	Column 2	Column 3
x-position	y-position	z-position

Fortunately, HFSS also integrates with Microsoft® Visual Basic® Scripting Edition (VBScript) [23], which eliminates the tediousness associated with outputting data files containing the E and H fields. The VBScript is used to not only automate the process of uploading *.pts* files and outputting data files, but is also used to determine the relevant HFSS model parameters and geometry. Therefore, when running the FEM-NFFT-GO routine, the near-zone-field sampling is automated and transparent to the user.

Appendix B describes the Matlab and VBScript code used to automate the near-zone field sampling process. This code includes the outputting of the relevant HFSS model parameters and geometry, the generation of *.pts* files, and the outputting of the sampled near-zone field values to ASCII text files to be further processed by Matlab.

Two important parameters associated with near-zone field sampling are sampling location and sampling resolution. The sampling location is a rectangular surface similar to the solution box, and called the sampling box. Through a trial of FEM-NFFT processing, a desirable location for the sampling box was determined to

be ¼ the size of the solution box. Therefore, if a 2λ solution box is used, a λ/2 sampling box is used. Results verifying the ideal solution box and sampling box dimensions are withheld to the FEM-NFFT results shown in Chapter 4, since the complete FEM-NFFT technique should be presented prior to the FEM-NFFT results. The sampling resolution is specified in terms of the number of points per wavelength. A reasonable sampling resolution used for much of this work is 10 points/λ. However, as will be shown later with the null field test, occasionally, higher resolution is necessary. The determination of whether or not to use higher resolution is application specific.

3.2.2 Running the FEM-NFFT-GO Routine

This section describes the procedure necessary for running the FEM-NFFT-GO routine. This involves running a Matlab script in conjunction with HFSS.

3.2.2.1 HFSS Requirements

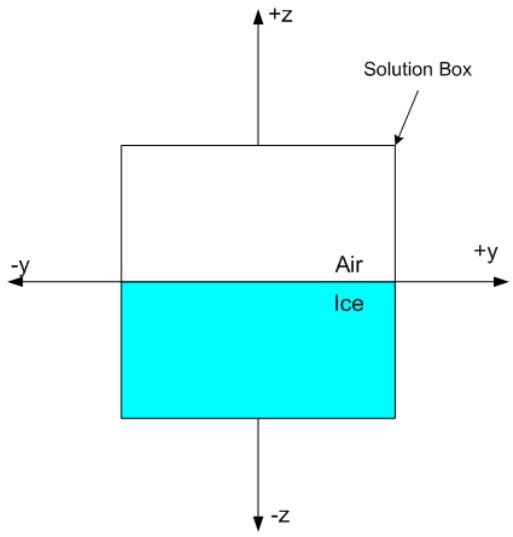

Figure 3.9 – HFSS Half-Space Modeling Convention

In order for HFSS to interface properly with the FEM-NFFT-GO routine, some modeling and naming conventions are required when modeling antennas in HFSS. When modeling ice-mounted antennas in HFSS, the Matlab code assumes that the half-space of ice extends from $z=0$ towards negative values of z, and the half-space of air extends from $z=0$ towards positive values of z. This is shown in Figure 3.9.

Table 3.4 – HFSS Model Naming Conventions

HFSS Item	Required Name
Solution Box	BoundaryBox
Solution Setup	Setup1

Due to the VBScript used in automatically sampling the near-zone electric and magnetic fields, some naming conventions are required for building the HFSS model. These naming conventions are outlined in Table 3.4. As discussed previously, the "Solution Box" is the box enclosing the solution space, on which radiating boundary conditions are specified. The "Solution Setup" was discussed in Section 2.1, and "Setup1" is in fact the default name.

The only other requirement of HFSS when running the FEM-NFFT-GO routine is that the desired HFSS model with solved near-zone field values be open while running the NFFT portion of the routine, which accomplishes the near-zone field sampling. Also, only one HFSS model at a time should be open while running the routine.

3.2.2.2 The *Master.m* Matlab File

In this section, the operation of the *Master.m* Matlab script file is discussed, which is the only code with which the user is required to interface. The *Master.m* script is divided into three sections: inputs to specify for the FEM-NFFT-GO routine,

the FEM-NFFT routine, and the GO routine. The way that the script is divided allows for the user to run the FEM-NFFT routine by itself, or in conjunction with the GO routine.

Table 3.5 – FEM-NFFT-GO Input Parameters

Input	Description	Format
dirIn	the directory containing the raw near-zone field data	string
ptsInput	sample points per wavelength	integer
sDecXY	the sampling box decrement value for the 4 vertical faces	real number
sDecZ_Top	the sampling box decrement value for the top face	real number
sDecZ_Bot	the sampling box cecrement value for the bottom face	real number
thetaMin	the minimum value of observatin angle θ	degrees
thetaMax	the maximum value of observatin angle θ	degrees
numTheta	the number of θ values desired	number
phi	the single observation angle Φ	degrees
e1	the relative permittivity of the top medium	real number
e2	the relative permittivity of the bottom medium	real number
u1	the relative permeability of the top medium	real number
u2	the relative permeability of the bottom medium	real number
location	the ice density profile model to use	(1) for Antarctica, (2) for Greenland
zDepth	the depth values in meters at which to calculate the far-zone gain	Matlab vector

There are a total of 15 inputs required for the FEM-NFFT-GO routine, which are described in Table 3.5. The input *dirIn* is the directory which contains all of the intermediate text files for communicating with HFSS, which includes among other things, the text files containing the near-zone electric and magnetic field values (see Section 3.2.1). The input *ptsInput* is the sampling resolution in terms of points/λ described in Section 3.2.1.

Three of the more complicated input parameters are *sDecXY*, *sDecZ_Top*, and *sDecZ_Bot*. Each of these inputs are used to specify the sampling box size. The *sDecXY* input specifies the reduction in size of the sampling box relative to the solution box in the *X* and *Y* dimensions. The *sDecZ_Top* input specifies the reduction in size of the sampling box relative to the solution box in the positive *Z* dimension. Finally, the *sDecZ_Bot* input specifies the reduction in size of the sampling box relative to the solution box in the negative *Z* dimension. The formulas for determining the size of the sampling box from the decrement factors are as follows

$$sampBox_{XY} = (solution\ box\ size) - 2 * sDecXY \qquad \textbf{Eq. 3.28}$$

$$sampBox_{Z} = (solution\ box\ size) - sDecZ\_Top - sDecZ\_Top \qquad \textbf{Eq. 3.29}$$

where $sampBox_{XY}$ is the size of the sampling box in wavelengths in the *X* and *Y* dimensions and $sampBox_{Z}$ is the size of the sampling box in wavelengths in the *Z* dimension.

The reason for differentiating the sampling box size in the *X*, *Y*, and *Z* dimensions has to do with the variability in HFSS antenna modeling. As discussed in Section 2.2, waveport excitation requires that the port be connected to the solution box boundary. If uniform reduction in the sampling box relative to the solution box occurred in each dimension, this could cause overlap of the sampling box and the antenna, which may be undesirable. Therefore, the option for non-uniform sampling box size allows for the sampling box to be kept from overlapping with the antenna location, if desired.

The observation angles are specified by four variables, *thetaMin*, *thetaMax*, *numTheta*, and *phi*. Therefore, the far-zone fields determined by the FEM-NFFT-GO routine are always computed through a range of θ values at a constant value of φ.

The material parameters for the dielectric half-space are specified by four variables. The relative permittivity and relative permeability of the upper half-space (air for purposes of ice-penetrating radar) are specified by *e1* and *u1*, respectively.

For the lower half-space (glacial ice for purposes of ice-penetrating radar), the relative permittivity and relative permeability are specified by *e2* and *u2*, respectively.

The final two input variables are only relevant for the GO routine. The input *location* specifies the empirical constants to use for the glacial ice-density model (see Section 3.1.2.1). A value of "1" specifies usage of the Antarctic empirical constants, and a value of "2" specifies usage of the Greenland empirical constants (see Table 3.1). The last input *zDepth* is a one-dimensional Matlab row-vector specifying the various depths in meters, within the ice, at which to determine the far-zone electric field gain.

The FEM-NFFT section of the *Matlab.m* function contains calls to two sub-functions, *Equivalent_Currents* and *NFFT*. *Equivalent_Currents* performs the sampling of the near-zone electric and magnetic fields and their conversion to equivalent surface currents, and basically implements the equivalence theorem. *NFFT* performs the near-to-far-field transformation, and basically implements the reciprocity theorem. Since *Equivalent_Currents* is an intermediate step, its outputs are not listed here. However, the separation of the implementation of the equivalence and reciprocity theorems eliminates the need for re-sampling the near-zone electric and magnetic fields and converting them to equivalent currents unnecessarily. Descriptions of the *Equivalent_Currents* outputs are described in the source code.

The outputs from the *NFFT* sub-function are listed in Table 3.6. These outputs include the observation angles, intrinsic impedances of the upper and lower mediums, and the theta and phi components of the quasi-far-zone electric field in both complex and magnitude format (relative to an isotropic radiator). The variables *EthetaIN* and *EphiIN* are in magnitude format which is required for input to the sub-function that performs the GO routine.

The GO section of the *Matlab.m* function contains a call to the *Gain_Factor* sub-routine which implements the geometric-optics ray-tracing calculations. The outputs of *Gain_Factor* are listed in Table 3.7. The primary outputs

of concern are *GthetaAD* and *GphiAD* which are the theta and phi components of the far-zone electric gain. *GthetaAD* and *GphiAD* are 2D matrices that are a function of the effective look angle *aidaPrime* in the row dimension, and a function of *zDepth* in the columns dimension.

Table 3.6 – FEM-NFFT Output Parameters

Input	Description	Format
Etheta	the theta component of the quasi-far-zone electric field versus theta	complex values
Ephi	the phi component of the quasi-far-zone electric field versus theta	complex values
angleMatrix	the value of theta and phi for each pair of observation angles	radians
N1	the intrinsic impedance of the upper medium	ohms
N2	the intrinsic impedance of the lower medium	ohms
EthetaIN	the theta component of the quasi-far-zone electric field gain versus theta	magnitude relative to an isotropic radiator
EphiIN	the phi component of the quasi-far-zone electric field gain versus theta	magnitude relative to an isotropic radiator

Table 3.7 – GO Output Parameters

Input	Description	Format
GthetaAD	the theta component of the far-zone electric gain versus effective look angle and depth	magnitude relative to an isotropic radiator
GphiAD	the phi component of the far-zone electric gain versus effective look angle and depth	magnitude relative to an isotropic radiator
aidaPrime	the effective look angle	radians
Gf	the gain factor improvement matrix	number

CHAPTER 4: Far-Zone Field Results for Ice-Mounted Antennas

Far-zone field results obtained using the FEM-NFFT-GO techniques are presented in this chapter (Section 4.4). But, prior to their presentation, results validating the accuracy of the FEM-NFFT routine are presented in Section 4.1. Recall that the FEM-NFFT procedure is useful on its own for determining far-zone fields for antennas mounted above a homogeneous half-space.

4.1 FEM-NFFT Validation Tests

Four tests were performed to validate the FEM-NFFT technique for obtaining the far-zone electric fields above a dielectric half-space. The first two of these tests check the accuracy of the FEM-NFFT routine by comparing the FEM-NFFT results to theoretical predictions. The third test validates the choice of near-zone field sampling location when using the FEM-NFFT routine. The fourth test determines whether or not similar far-zone field results could have been obtained using HFSS alone, by substantially increasing the solution box size to several wavelengths.

4.1.1 The Null Field Test

A null field test was the first devised to validate the FEM-NFFT algorithm. In this test, a plane wave was incident from a source located far from the sampling box. Figure 4.1(a) depicts the original geometry and the equivalent geometry is depicted in Figure 4.1(b). Here, the fields located some distance from the air/ice interface are E_b and $H_{b,}$ and those near the air/ice interface are E_a and H_a. In Figure 4.1(b), E_a and H_a are sampled and converted to equivalent electric and magnetic source currents using Equations 2.1 and 2.2. According to the equivalence principle, the observer senses the

same fields E_b and H_b, meaning that J_s and M_s radiate null fields external to the sampling box, and the negative of E_a and H_a internal to the sampling box. So, the null-field test involved verifying whether the equivalent currents radiate null-fields external to the sampling box.

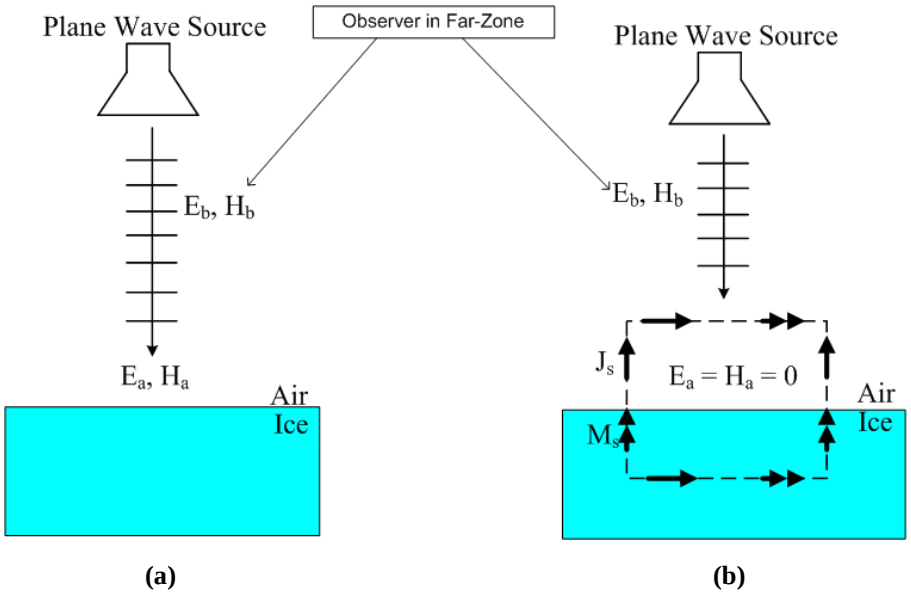

Figure 4.1 – The Null-Field Test

(a) Original Situation (b) Equivalent Situation

Table 4.1 – The Null-Field Test Cases

Test Case	Plane Wave Propagation	Plane Wave Incidence	Incident Angle	Observation Angle (Φ)	Associated Figure
1	from ice to air	Normal	0°	90°	Figure 3.7(a)
2	from ice to air	Oblique	30°	90°	Figure 3.7(b)
3	from ice to air	Oblique	30°	45°	Figure 3.7(c)
4	from air to ice	Oblique	30°	0°	Figure 3.7(d)

Four test cases involving the null-field test were performed. These test cases, outlined in Table 4.1, involve different combinations of plane wave source location (either in air or ice), plane wave angle of incidence, and observation or look angle ϕ.

For each test case, the electric far-zone fields radiated by the equivalent surface currents produced a noisy response, not at all resembling that of a plane wave. With increasing sampling resolution (points/λ, discussed in Section 3.2.1), the magnitude of the far-zone radiated fields decreased. In order to better quantify the decreasing electric field magnitude with increasing sampling resolution, the sampling box was treated as a scatterer with the following radar cross section

$$\sigma = \frac{4\pi \left| E_{\max} \right|^2}{\left| E_{inc} \right|^2} \qquad \textbf{Eq. 4.1}$$

where $E_{\max}$ is the maximum value of the electric far-zone field across all values of θ for a particular look angle ϕ. Also, E_{inc} is simply the magnitude of the incident plane wave, which was 1 V/m. Next, Equation 4.1 was normalized by dividing by the area of the ice interface, and converted to dB using the following

$$(\sigma / A)_{dB} = 10 \log\left(\frac{\sigma}{A}\right) \qquad \textbf{Eq. 4.2}$$

The results of the four test cases are shown in Figure 4.2. Note that for test case 1, only a ϕ component of the electric field was present due to the observation angle of $\phi = 90^{o}$, and for test case 2, only a θ component of the electric field was present due to the observation angle of $\theta = 0^{o}$. In each of these test cases, the amount of energy scattered by the ice decreased significantly with increasing sampling resolution, reaching nearly -25 dB in each case. Therefore, the FEM-NFFT procedure passed the null-field test, generating null fields external to the sampling surface when a plane wave is incident on the half-space of ice, as dictated by the electromagnetic reciprocity theorem. In each case, a sampling resolution between 10 to 20 pts/λ was required to achieve a normalized σ of -10 dB. As will be shown in the Hertzian dipole

test, a sampling resolution of only 10 pts/ λ is generally adequate for obtaining far-zone fields.

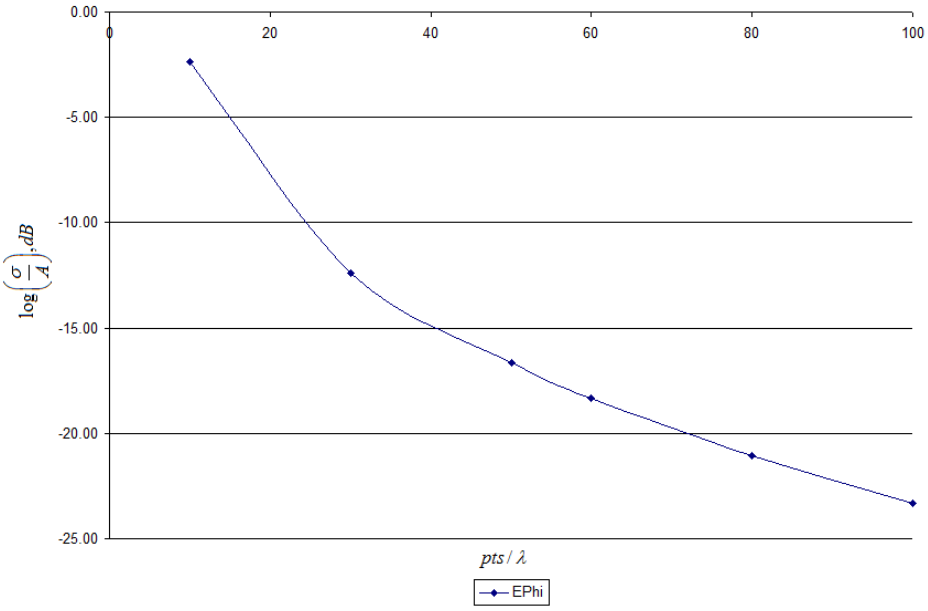

(a) Test 1

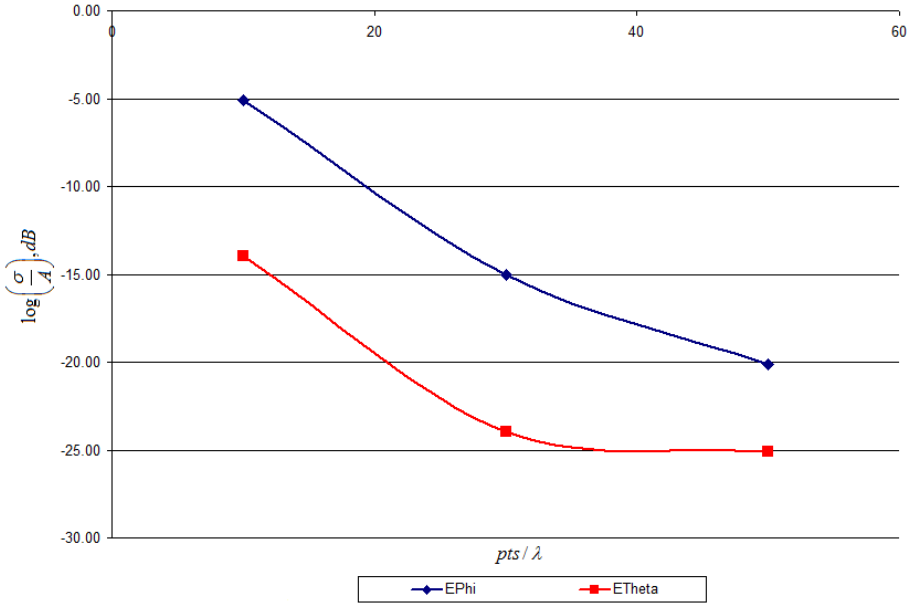

(b) Test 2

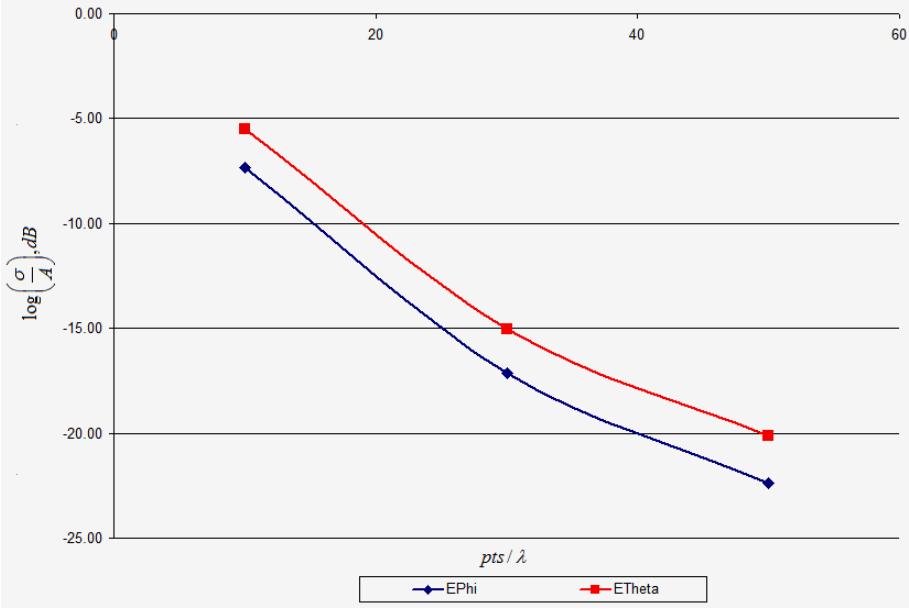

(c) Test 3

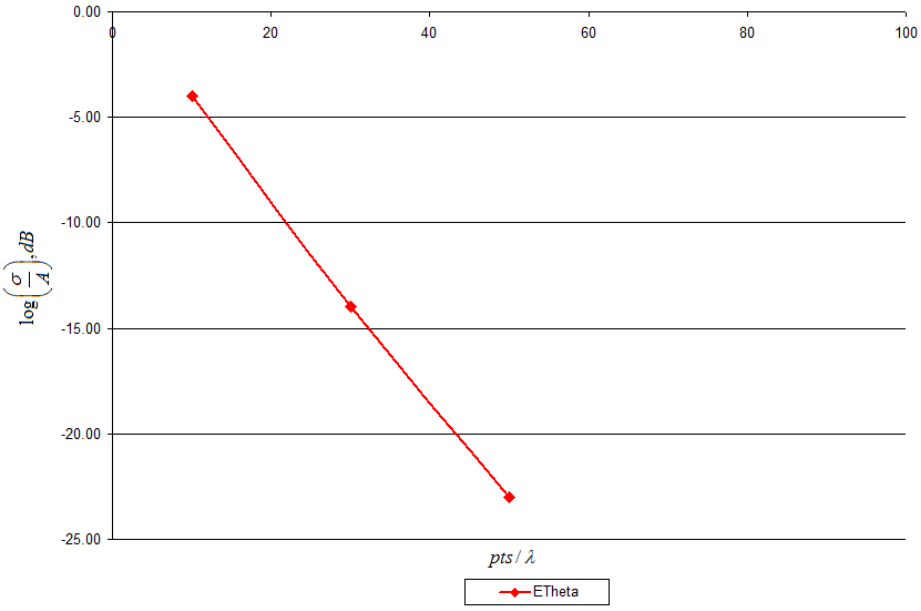

(d) Test 4

Figure 4.2 – The Null-Field Test: Four Test Cases

4.1.2 The Hertzian Dipole Test

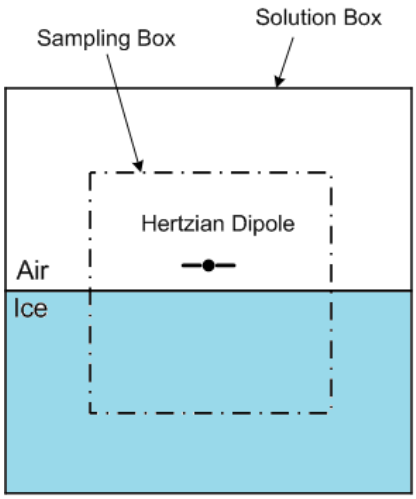

Figure 4.3 – Horizontal Hertzian Dipole

The next test of the FEM-NFFT technique was to determine the far-zone fields of a horizontal Hertzian dipole above a half-space of glacial ice, as shown in Figure 4.3. The exact result for the far-zone fields of a Hertzian dipole above a dielectric half-space are known and are presented in [41]. Due to the simplicity of the Hertzian dipole, the Green's function [44] can be determined exactly when the dipole is located above a dielectric half-space. In fact, the equivalent source currents presented earlier and used in the NFFT algorithm are nothing but Hertzian dipoles themselves.

In this test, a horizontal Hertizan (y-directed) dipole was modeled above a half-space of ice with a dielectric constant equal to that at the ice surface using HFSS. Then, the near-zone fields were sampled from HFSS and exported to Matlab for NFFT processing. Table 4.2 specifies the parameters for repeating the FEM-NFFT procedure, and obtaining the same results as presented here.

Table 4.2 – Horizontal Hertizan Dipole Test Parameters

ε_r (ice):	1.8
Antenna Height Above Ice:	λ/10
pts/λ:	10
Antenna Length:	λ/100
Solution Box Size:	2λ
Solution Box Type:	square
Sampling Box Size:	λ/2
Sampling Box Type:	square
Ice Layer Size:	λ

The far-zone field patterns obtained from the FEM-NFFT technique for both the E-plane and H-plane are shown in Figures 4.4 and Figures 4.5, respectively. Also shown in Figures 4.4 and Figures 4.5 are the corresponding "Exact" and "Free-Space" results. The exact results were obtained by using the closed form solution for the far-zone fields of a Hertzian dipole located above a half-space of glacial ice. In both Figures 4.4 and 4.5, it is seen that the FEM-NFFT and Exact results are virtually identical, indicating the accuracy of the technique. The success of the Hertzian dipole test provides confidence in using the FEM-NFFT technique for analyzing other antennas.

Also shown in Figures 4.4 and 4.5 are the free-space far-zone fields of a horizontal Hertzian dipole. Comparing the FEM-NFFT (or Exact) results with the free-space pattern reveals the effect of the ice has on the far-zone pattern. For the E-plane pattern shown in Figure 4.4, the gain increases within the ice and decreases above the ice by approximately 2 dB. Sidelobes which did not exist in the free-space pattern occur within the ice. In Figure 4.5, the H-plane changes from the isotropic free-space pattern to a much more directive one with nulls at the air/ice interface. Again, the gain within the ice increased by approximately 2 dB.

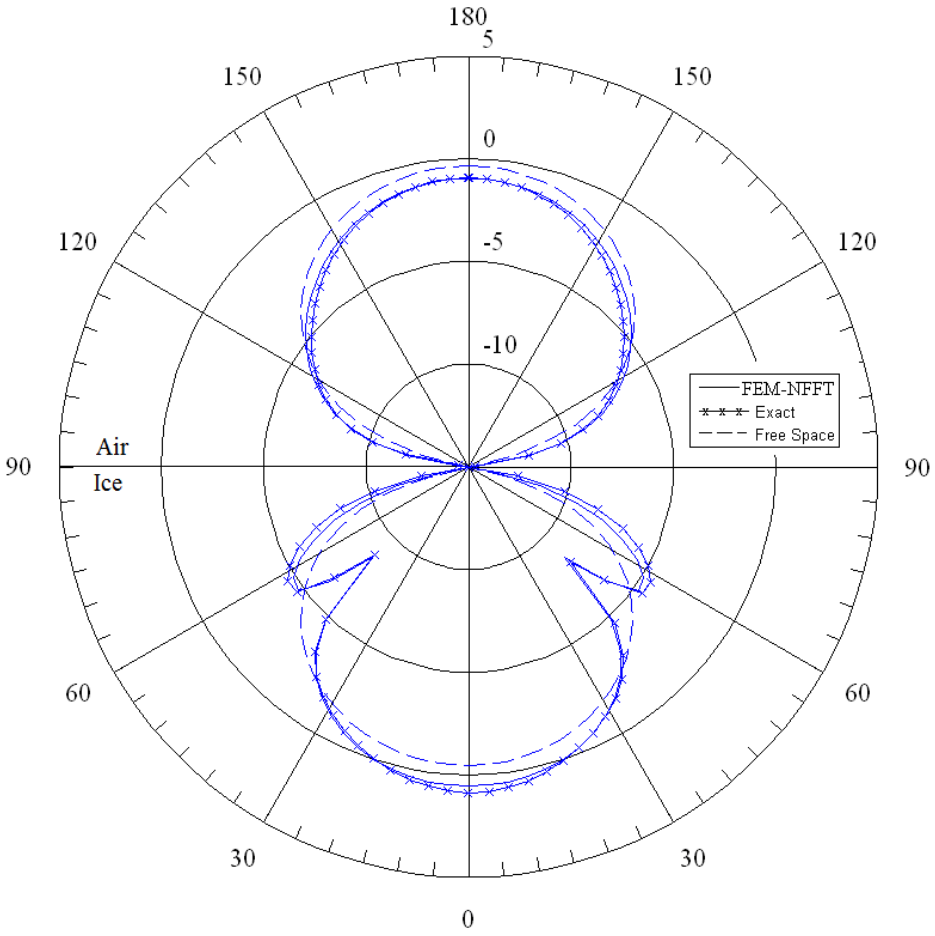

Figure 4.4 – E-Plane of Horizontal Hertizan Dipole Far-Zone Fields (dBi): FEM-NFFT, Exact, and Free Space

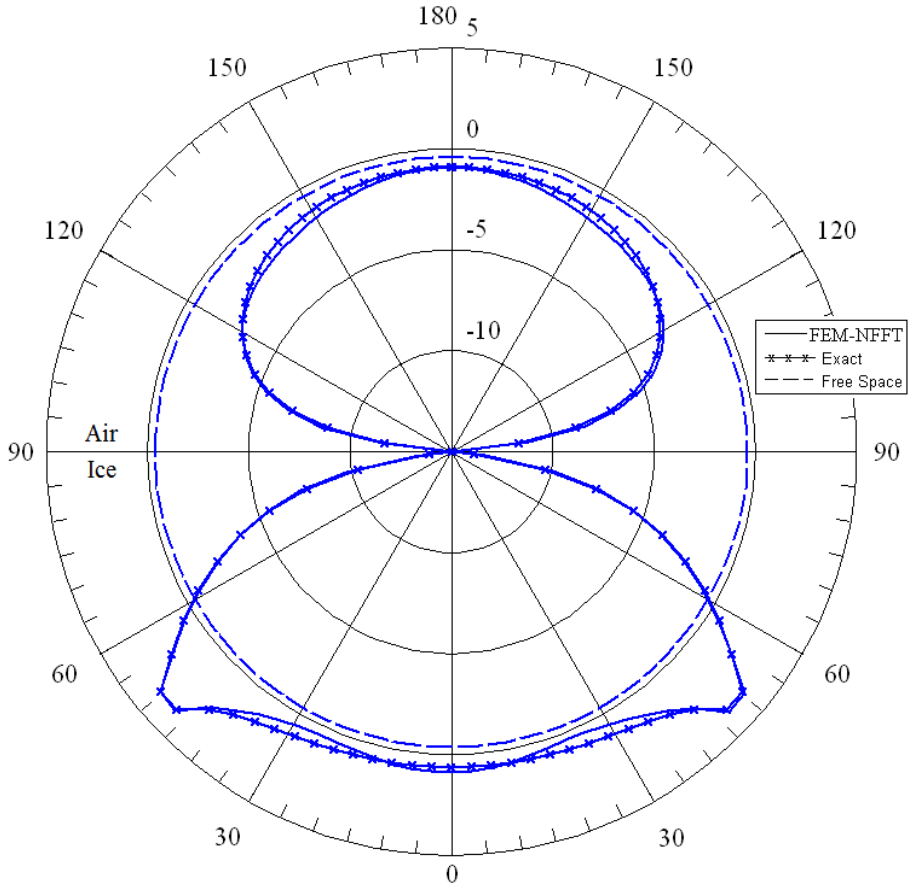

Figure 4.5 – H-Plane of Horizontal Hertzian Dipole Far-Zone Fields (dBi): FEM-NFFT, Exact, and Free Space

4.1.3 Effects of Sampling Location

The effects of near-zone field sampling location on the resulting far-zone fields produced from the FEM-NFFT routine will now be presented. The far-zone fields for a vertical Hertzian dipole above a half-space of ice (Figure 4.6) are presented here for a range of sampling box sizes. Table 4.3 presents the relevant modeling parameters.

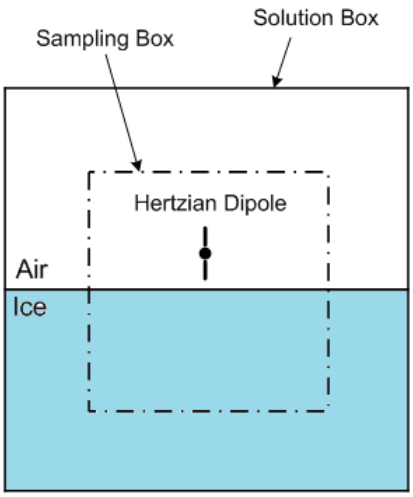

Figure 4.6 – Vertical Hertzian Dipole

Table 4.3 – Vertical Dipole Modeling Parameters

ε_r (ice):	1.8
Antenna Height Above Ice:	λ/10
pts/λ:	10
Antenna Length:	λ/100
Solution Box Size:	2λ
Solution Box Type:	square
Sampling Box Size:	λ/2
Sampling Box Type:	square
Ice Layer Size:	λ

The E-plane of the far-zone fields using both the "Exact" [41] and FEM-NFFT solutions for the vertical Hertzian dipole are presented in Figures 4.7, 4.8, and 4.9. Each figure uses a different near-zone field sampling box size. In Figure 4.7, the near-zone fields were sampled on the outer edge of the solution box (the same location used by HFSS its own NFFT routine). In this case, the Exact and FEM-NFFT results differ significantly. Then, in Figure 4.8, the sampling box size was λ, which is half the size of the solution box in this case. Notice that the Exact and FEM-NFFT results are more similar in this case, relative to Figure 4.7. Finally, in Figure 4.9, the

sampling box size was reduced to λ/2, which is one quarter the size of the solution box. Here, the Exact and FEM-NFFT results are nearly identical. Additionally, for all orientations and observation angles involving Hertzian dipoles, a sampling box one fourth the size of the solution box yielded results that compared most favorably with the Exact result. Therefore, in all future usage of the FEM-NFFT routine, a sampling box of one fourth the size of the solution box is recommended.

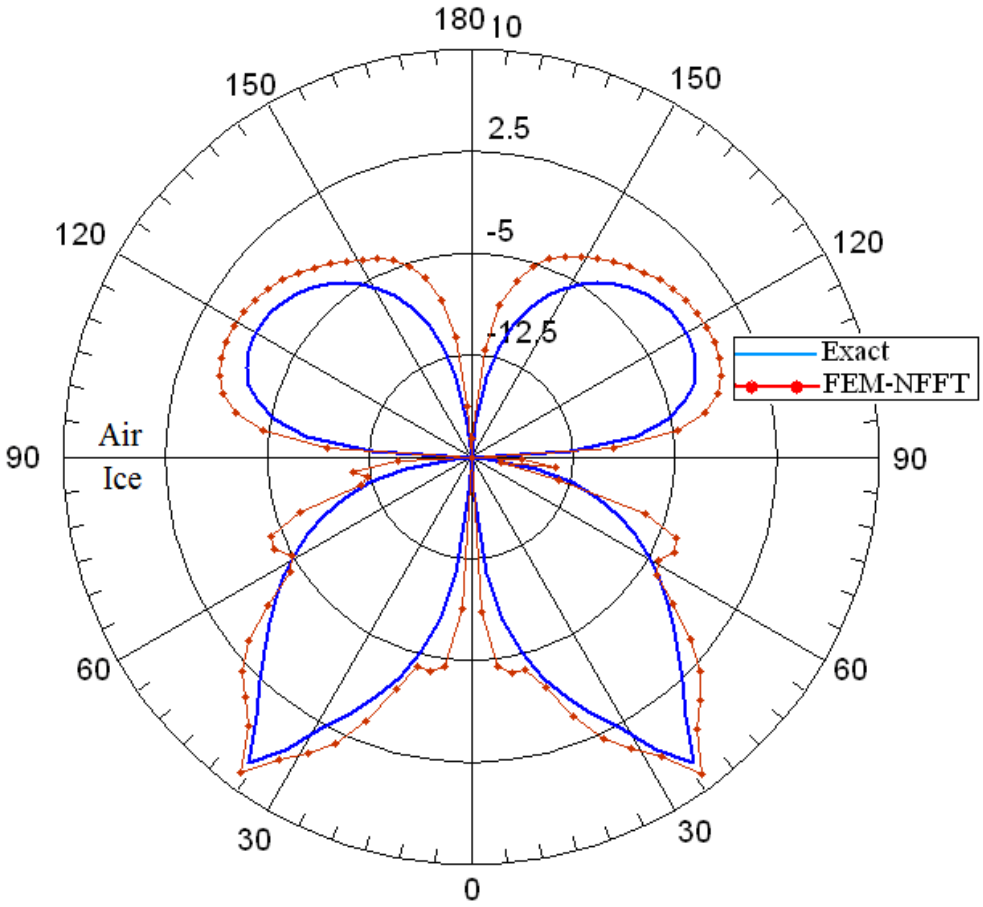

Figure 4.7 – Far-Zone E-Plane of Vertical Hertzian Dipole Above Ice (dBi): Near-Zone Fields Sampled at 2λ

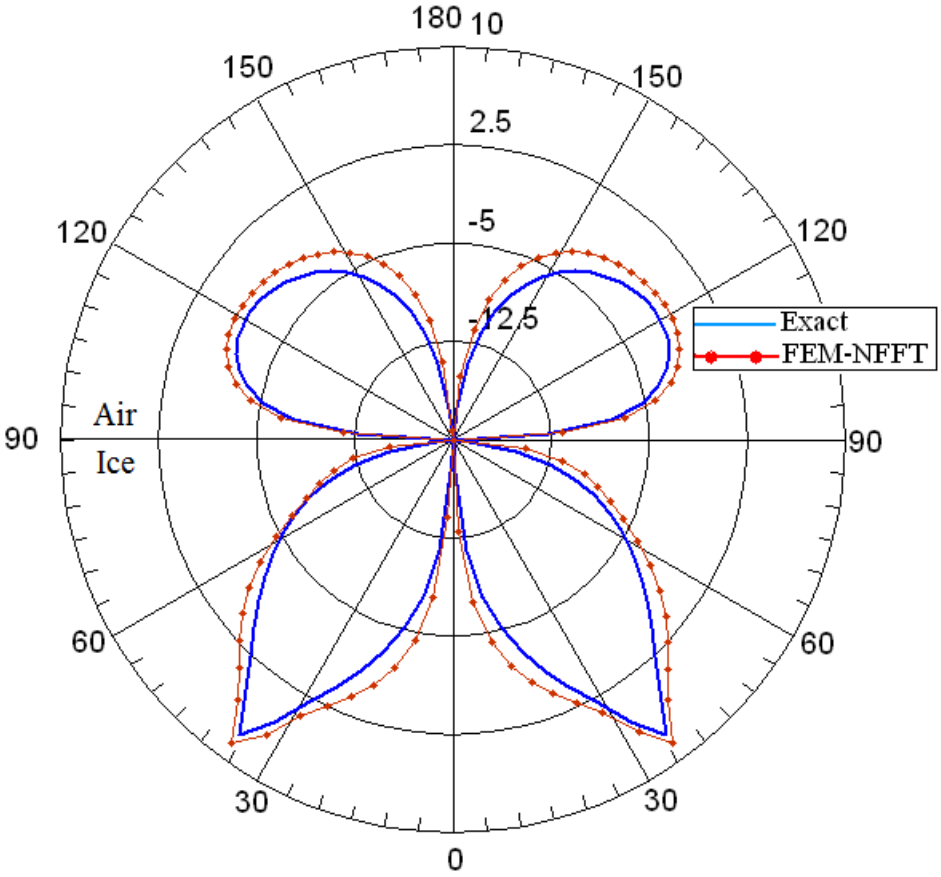

Figure 4.8 – Far-Zone E-Plane of Vertical Hertzian Dipole Above Ice (dBi): Near-Zone Fields Sampled at λ

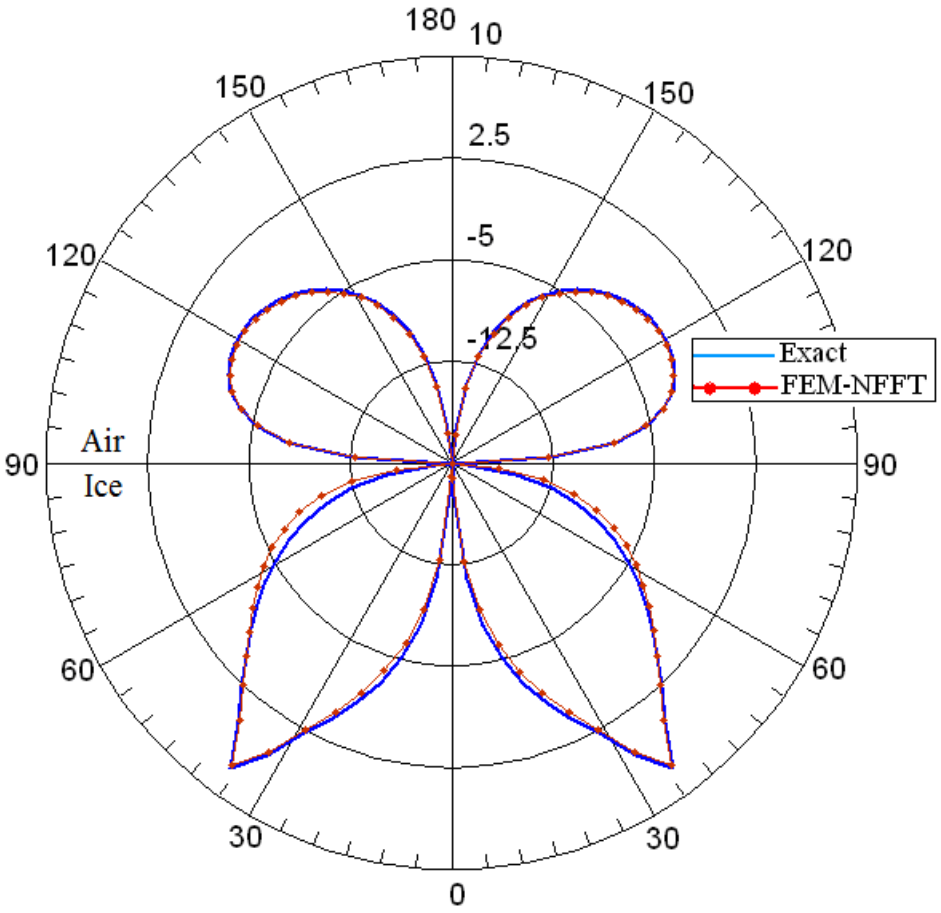

Figure 4.9 – Far-Zone E-Plane of Vertical Hertzian Dipole Above Ice (dBi): Near-Zone Fields Sampled at 0.5λ

4.1.4 Comparing FEM-NFFT Results with HFSS Near-Zone Results

A question that arises when using HFSS is whether the solution box can be made large enough to where the calculated near-zone fields are actually in the far-zone, thus making them far-zone fields. In order to test this idea, an HFSS simulation was performed for a horizontal Hertzian dipole, as shown in Figure 4.2 but using the parameters outlined in Table 4.4. The near-zone fields calculated on a sphere with a diameter equal to the square solution box width were determined and compared with the results obtained from the FEM-NFFT procedure. In this case, the solution box

size was 4λ, which is large enough for the outer edge of the solution box to be in the far zone [5].

Table 4.4 – HFSS Near-Zone Field Parameters

ε_r (ice):	1.8
Antenna Height Above Ice:	λ/10
Antenna Length:	λ/100
Solution Box Size:	4λ
Solution Box Type:	square
Ice Layer Size:	2λ
Near-Zone Calculation Sphere Diameter:	4λ

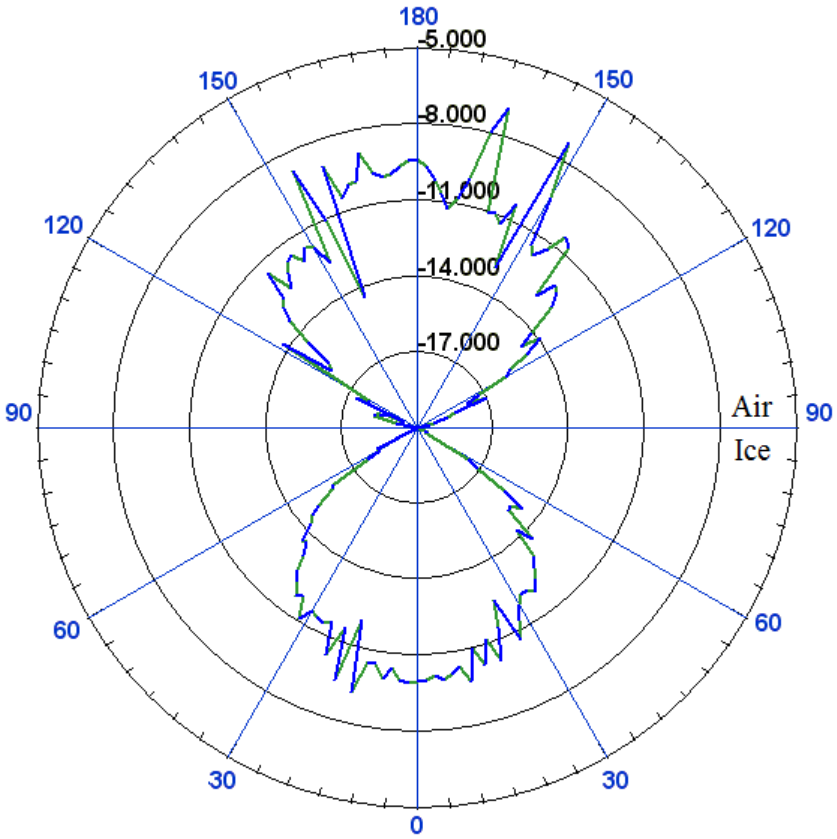

Figure 4.10 – E-Plane of Horizontal Hertzian Dipole Far-Zone Fields (dBi): From HFSS Near-Field Calculator

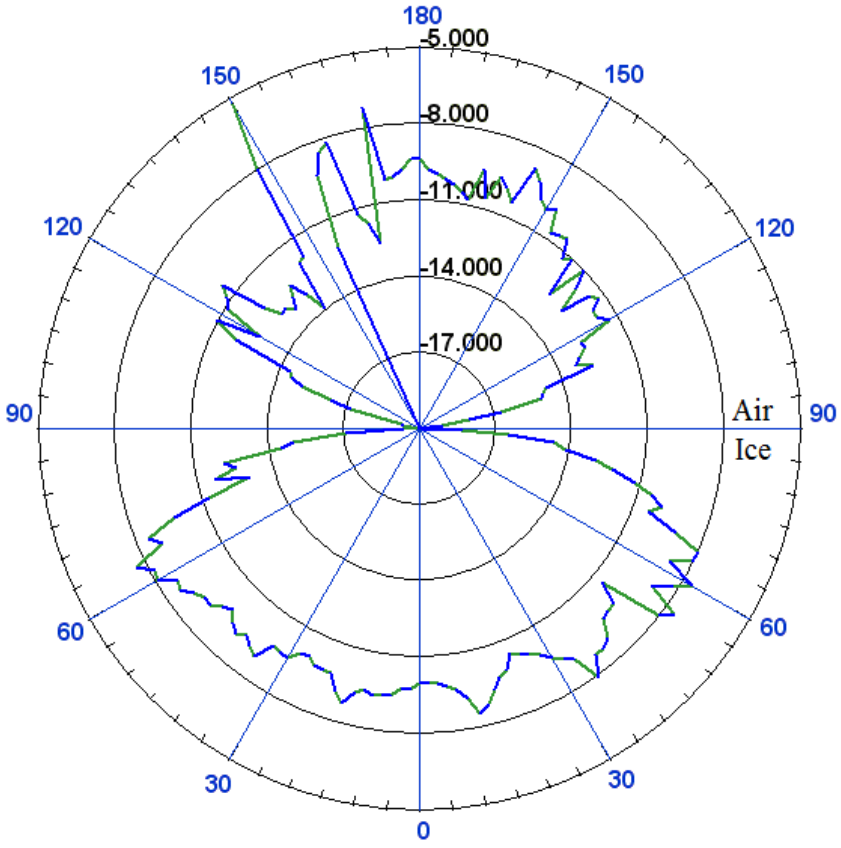

Figure 4.11 – H-Plane of Horizontal Hertzian Dipole Far-Zone Fields (dBi): From HFSS Near-Field Calculator

The E-plane and H-plane obtained from the HFSS near-zone field calculator are shown in Figures 4.10 and 4.11, respectively. Comparing the E-plane obtained from HFSS (Figure 4.10) with the E-plane obtained from the FEM-NFFT procedure (Figure 4.4), it can be seen that although the two results are somewhat similar in shape, the result from HFSS is in fact quite different. Notice the lack sidelobes in Figure 4.10 for the pattern directed towards the ice, and that the pattern is extremely jagged and asymmetrical. Additionally, the magnitude of the E-plane obtained from HFSS is over 10 dB less than that obtained by the FEM-NFFT algorithm. Clearly, the HFSS result for the E-plane is incorrect. Similarly, the H-plane obtained from HFSS (Figure 4.11) is similar in shape to the correct result obtained from the FEM-NFFT algorithm (Figure 4.5). However, as with the E-plane result, the asymmetry,

jaggedness, and incorrect magnitude make the H-plane result obtained from HFSS incorrect.

To conclude, HFSS can not be used to determine far-zone field patterns for ice-mounted antennas. Even increasing the solution box to the enormous size of 4λ, which introduces significant computational consequences, proved unavailing.

4.2 Combined FEM-NFFT-GO Results

The far-zone antenna gain at any depth for ice-mounted antennas, obtained via the FEM-NFFT-GO technique, is presented in this section. Results for two different antennas are shown, including a horizontal Hertzian dipole and a printed-circuit board tapered slot antenna (Vivaldi). Also presented are the free-space pattern and FEM-NFFT result for the Vivaldi antenna, primarily to provide a basis for evaluating the FEM-NFFT-GO results. Recall that the free-space pattern and FEM-NFFT result for the horizontal Hertzian dipole were previously presented in Section 4.1.2, where it was used as a test of the FEM-NFFT routine's accuracy.

The Vivaldi antenna, shown in Figure 4.12, is a complex antenna developed at CReSIS (Center for Remote Sensing of Ice Sheets) by Ben Panzer [33]. It was designed to be lightweight, wideband, and be multipurpose [33]. The lightweight constraint arises from its intended usage on an unmanned aerial vehicle (UAV). The antenna has a very wide bandwidth, operating from 162 MHz to 1.121 GHz. At the lower end of its band (162-250 MHz), it is suitable for ice depth-sounding. Also, from 600-900 MHz, it will be used for an accumulation radar, which shows the detailed year-by-year ice layering up to 200 meters with very fine resolution. At 214 MHz, the Vivaldi has a free-space pattern shown in Figure 4.13. The Vivaldi antenna was modeled using the parameters outlined in Table 4.5.

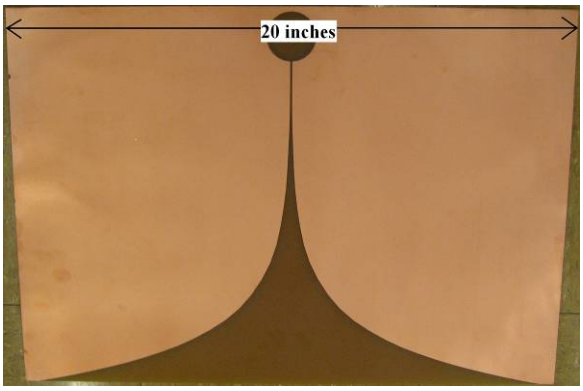

Figure 4.12 – Tapered Slot Antenna (Vivaldi)

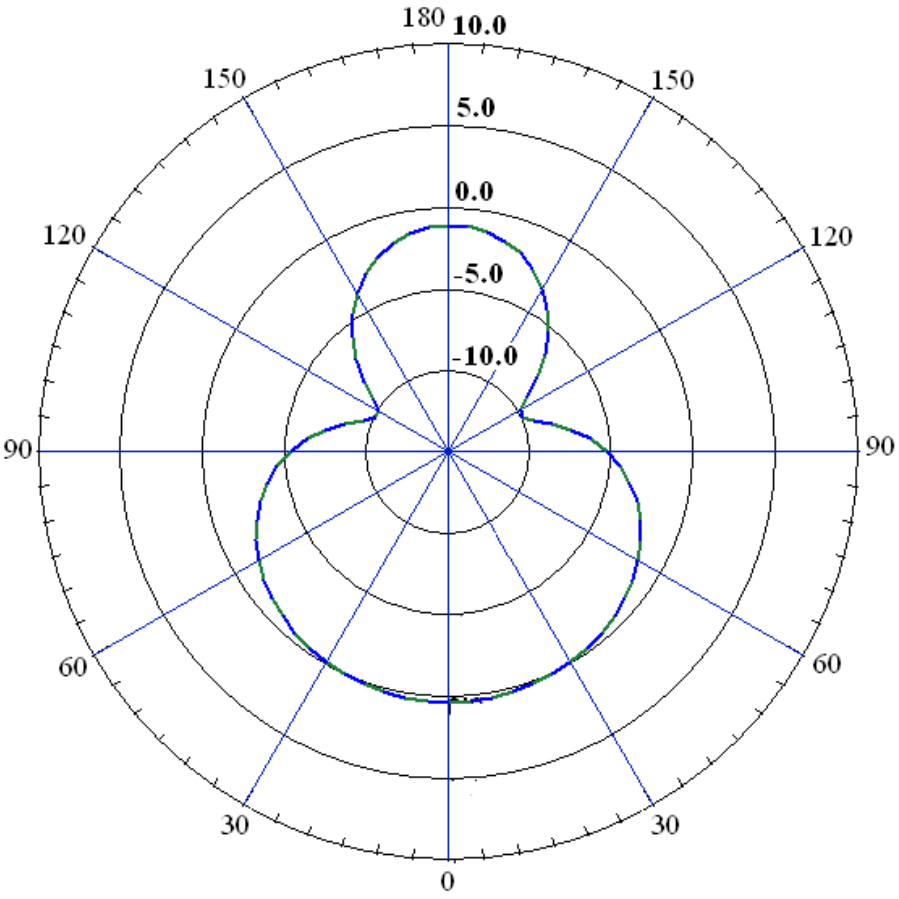

Figure 4.13 – Vivaldi Free-Space Pattern (dBi) – E-Plane

(nadir is 0^{o})

Table 4.5 – Vivaldi Modeling Parameters

ε_r (ice):	1.8
Antenna Height Above Ice:	λ/10
pts/λ:	10
Antenna Length:	λ/100
Solution Box Size:	2λ
Solution Box Type:	square
Sampling Box Size:	λ/2
Sampling Box Type:	square
Ice Layer Size:	λ

Using the FEM-NFFT routine, the far-zone antenna gain shown in Figure 4.14 was produced for a Vivaldi antenna mounted on glacial ice. Recall that in relation to the entire FEM-NFFT-GO technique the FEM-NFFT result is called the quasi-far-zone field. This is because in the FEM-NFFT-GO technique, the FEM-NFFT result is an intermediate step. Comparing the pattern directed towards 0^o in Figure 4.14 (ice is present) to that in Figure 4.13 (free-space), it is obvious that the ice significantly alters the gain pattern. The gain of the main lobe in the presence of the ice has increased by nearly 5 dB relative to the free-space pattern. Also, sidelobes are present for the pattern in the presence of ice, which were note present in the free-space pattern.

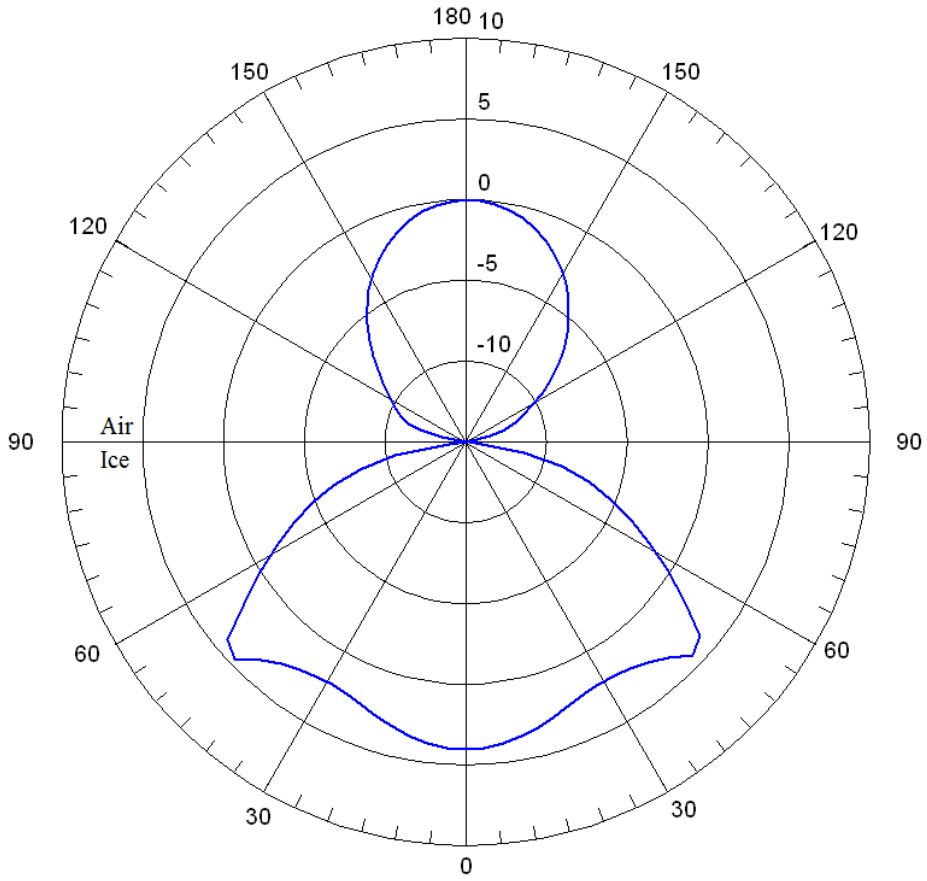

Figure 4.14 – Vivaldi FEM-NFFT Result – E-Plane Gain (dBi)

Next, using the quasi-far-zone gain (G_o from Section 3.1.2) shown in Figure 4.14, as the "input" to the GO technique, the gain patterns shown in Figure 4.15 were produced. Since the GO technique only has relevance for patterns within the ice that is all that is presented here. The gain at three separate depths is shown in Figure 4.15 and antenna gain both narrows and increases in maximum gain as the depth increases.

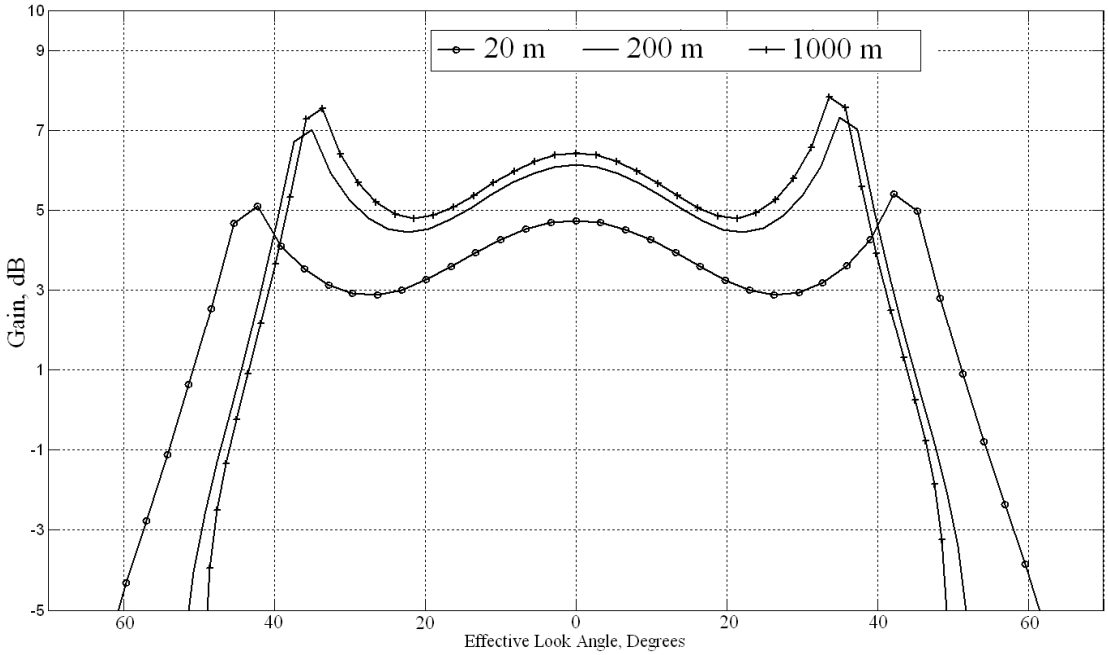

Figure 4.15 – Gain Pattern at Various Depths for Vivaldi Antenna (E-Plane)

Also presented is the far-zone gain versus depth for a horizontal Hertzian dipole. This is the same Hertzian dipole presented in Section 4.1.2. Figure 4.16 shows the Hertzian dipole gain for three separate depths. The gain pattern narrows and increases in maximum gain as the depth increases.

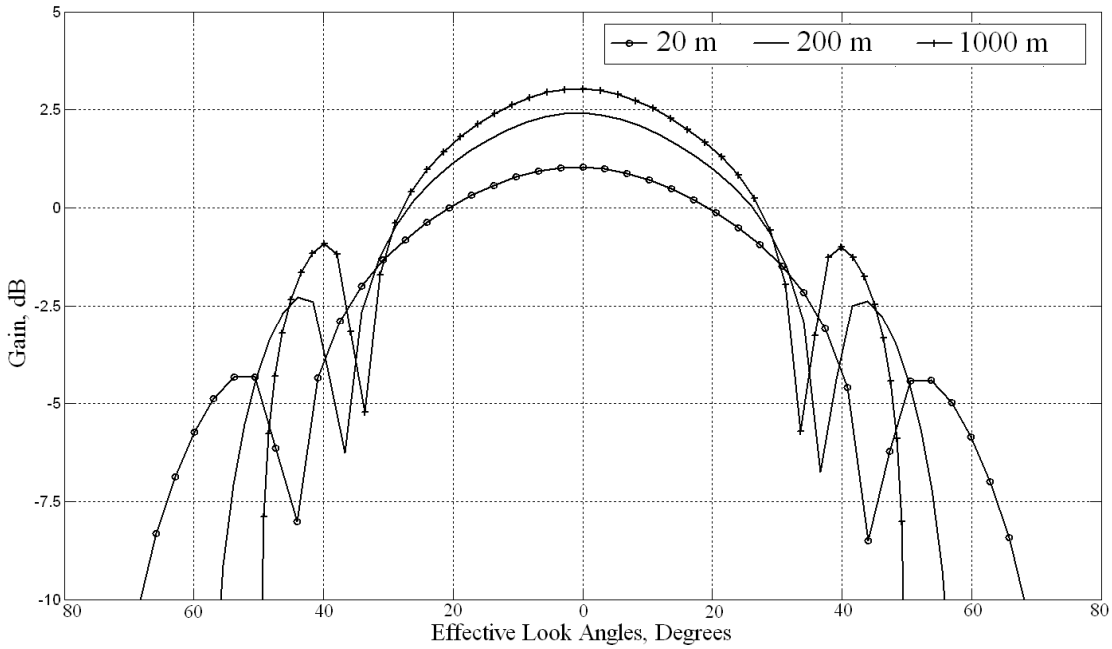

Figure 4.16 – Gain Pattern at Various Depths for Hertzian Dipole (E-Plane)

An important fact regarding the GO technique is that the focusing effect of the glacial ice density profile is independent of antenna pattern. For a given range of angles and range of depths, the same decrease in the angular extent of the gain pattern and increase in gain of the gain pattern will occur, regardless of the gain pattern input to the GO routine.

CHAPTER 5: Glacial Ice Temperature Extraction from Attenuation Measurements

Ice attenuation can be measured from radar returns using a surface-based bistatic radar system, such as that presented in Section 1.2. Two common mid-point (CMP) antenna configurations are utilized in the data attainment: one where transmit and receive antennas are at a fixed distance from each other, and another where the transmit and receive antennas are at a fixed incident and reflected angle with respect to each other. Results from these two arrangements are then combined to measure attenuation as a function of depth.

The ultimate goal of obtaining ice attenuation as a function of depth is to determine the ice temperature as a function of depth. However, prior to relating attenuation to ice temperature, the basic causes of attenuation within glacial ice must be considered, which are presented in Sections 5.1 and 5.2. Also, in Section 5.3 existing temperature profile data is presented for glaciers in Antarctica and Greenland. These data reveal the range of temperatures typically encountered in glacial ice. Next, in Section 5.4, the relationship between loss mechanisms and the attenuation constant is presented. The method for measuring glacial ice attenuation from radar echoes is presented in Section 5.5. Then, the algorithm for extracting temperature from attenuation measurements is presented in Section 5.6. Finally, in Section 5.7, simulated results are presented that highlight the capabilities of the technique for extracting glacial ice temperature from radar echoes.

5.1 Causes of Attenuation in Glacial Ice

Two loss (attenuation) mechanisms can occur in glacial ice: conduction loss, and polarization loss. Conduction losses occur when the conductivity σ is greater than zero, and results in conduction current defined by the following

$$\bar{J}_C = \sigma \bar{E} \qquad \textbf{Eq. 5.1}$$

The conduction current causes some of the energy transmitted from the radar to be converted to heat within the ice.

Polarization losses are due to displacement current within lossy media. Displacement current results within any dielectric exposed to a time-varying electric field, and is described by the following

$$\bar{J}_D = j\omega\varepsilon\bar{E} \qquad \textbf{Eq. 5.2}$$

where ω is the frequency in radians per second. For materials with a real permittivity (i.e. lossless dielectric), equal amounts of energy are stored and released upon each cycle, meaning that $\bar{J}_D$ results in no loss. However, when the permittivity is complex, as with glacial ice, $\bar{J}_D$ causes some of the incident energy to be converted to heat.

Therefore, the causes of loss in glacial ice are due to conductivity σ and a complex permittivity. Generally, these two loss mechanisms are combined into a single imaginary component of the permittivity, where

$$\varepsilon = \varepsilon' - j(\varepsilon'' + \sigma/\omega) \qquad \textbf{Eq. 5.3}$$

Equation 5.3 can be simplified to the following

$$\varepsilon = \varepsilon_o(\varepsilon_r' - j\varepsilon_r'') \qquad \textbf{Eq. 5.4}$$

where ε_o is the free-space permittivity (8.854 x 10^{-12} F/m), the real part of the permittivity is

$$\varepsilon_r^{'} = \frac{\varepsilon^{'}}{\varepsilon_o} \qquad \textbf{Eq. 5.5}$$

and the imaginary part is

$$\varepsilon_r^{"} = \frac{\varepsilon^{"} + \sigma / \omega}{\varepsilon_o} \qquad \textbf{Eq. 5.6}$$

At depth-sounding frequencies in glacial ice, the loss is dominated by σ [28] and therefore, the imaginary part of ε can be simplified to

$$\varepsilon_r^{"} = \frac{\sigma / \omega}{\varepsilon_o} \qquad \textbf{Eq. 5.7}$$

which neglects contributions to loss arising from $\varepsilon^{"}$. However, Equation 5.7 is only applicable for frequencies below 700 MHz, since above this frequency, $\varepsilon^{"}$ (polarization loss term) increases with frequency and becomes very large. Equation 5.7 allows the conductivity and loss within ice to be entirely described by the permittivity ε. Since σ is the primary cause of loss in glacial ice, a further discussion of the causes of conductivity is warranted.

5.2 Conductivity in Glacial Ice

Radar signal attenuation within glacial ice is proportional to conductivity, which in turn depends on a number of factors, including impurity concentrations as well as the ice temperature [28]. Pure ice conductivity is due to the polarization of individual water molecules (H_2O), hydronium (H_3O^+) and hydroxyl (OH^-) ionic defects, and Bjerrum defects in the presence of high-frequency (0.1 to 300 MHz)

electric fields [35], which is the frequency range typically used for ice depth-sounding [15]. For impure ice, the conductivity also depends on the concentrations of acid ($[H^+]$), sea-salt chloride ([ss Cl^-]), and ammonium ($[NH_4^+]$). Since glacial ice is impure, its conductivity is dependent on each of the contributions mentioned above.

Each contributor to ice conductivity follows an Arrhenius-type temperature dependence. But, NH_4^+ can be neglected, since the product of its molar concentration (mol L^{-1}) and molar conductivity (S L m^{-1} mol^{-1}) is over an order of magnitude smaller than that for H^+ or Cl^- [28]. Therefore, the Arrhenius-type conductivity model can be represented by the following relation

$$\sigma = \sigma_p e^{\left[\frac{E_p}{k_B}\left(\frac{1}{T_r}-\frac{1}{T}\right)\right]} + \sigma_H \left[H^+\right] e^{\left[\frac{E_H}{k_B}\left(\frac{1}{T_r}-\frac{1}{T}\right)\right]} + \sigma_{Cl} \left[Cl^-\right] e^{\left[\frac{E_{Cl}}{k_B}\left(\frac{1}{T_r}-\frac{1}{T}\right)\right]} \qquad \textbf{Eq. 5.8}$$

where σ_p, σ_H, and σ_{Cl} are the molar conductivities of pure water, H^+, and Cl^-, respectively. Also, E_p, E_H, and E_{Cl} are the activation energies for pure water, H^+, and Cl^-. Also, k_B is Boltmann's constant and T_r is a reference temperature equal to 251 K.

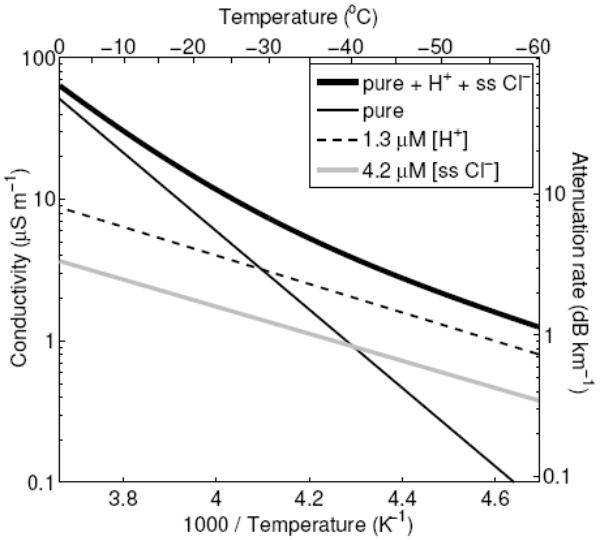

Figure 5.1 – Glacial Ice Conductivity Contributions [28] (For frequencies between 0.1 to 300 MHz)

Figure 5.1 compares the conductivity contributions from pure ice, H^+, and Cl for Siple Dome in Antarctica [28], within the frequency range typically used for radar depth-sounding (0.1 to 300 MHz). The pure ice component is dominate above -30^o C, and dominates more as the temperature is increased. Figure 5.1 assumes impurity concentrations of 1.3 μM for H^+ and 4.2 μM for Cl^-. Higher impurity concentrations would increase the temperature at which the pure component dominates conductivity.

Recall from earlier that attenuation is proportional to conductivity. Therefore, as the glacial ice temperature increases above -30^o C, the assumption that the ice attenuation profile is due to temperature changes with depth, and not impurity concentrations, becomes more reasonable. Assuming that the ice conductivity (and thus attenuation) is due solely to ice temperature leads to the following

$$\sigma = \sigma_p e^{\left[\frac{E_p}{k_B}\left(\frac{1}{T_r}-\frac{1}{T}\right)\right]} \qquad \textbf{Eq. 5.9}$$

One important consideration in validating the assumption that ice attenuation is solely a function of temperature is to consider the factors affecting ice temperature, as well as known temperature profiles from various glacial ice cores. Thus, it is important to determine the likeliness of encountering glacial ice temperatures greater than -30^o C.

5.3 Measured Glacial Temperature Profiles

Several factors contribute to the glacial ice temperature, including the surface temperature, the rate of geothermal heat influx from the base, and the vertical and horizontal components of velocity within the glacier [42 and 34]. The surface temperature of glacial ice is determined by climate, which includes elevation and seasonal effects, in addition to any global climate trends. Also, although glacial temperature distributions are not linear with depth, the temperature typically increases with increasing depth [31] due to a combination of increasing pressure with depth,

friction due to velocity gradients, and geothermal heat influx from the base. The degree of non-linearity in the temperature profile increases with increasing vertical velocity vectors [34].

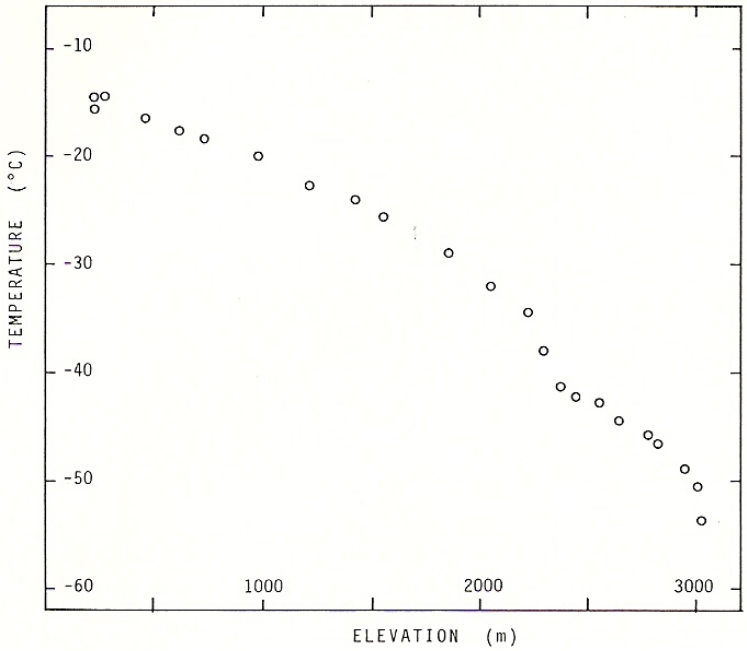

Figure 5.2 – Glacial Ice Temperature at 10 m Depth vs. Elevation [41]

Elevation above sea level has a profound effect on glacial ice temperatures [42], which can be attributed to increased ambient air temperature with elevation. The usual parameter used for indicating surface temperature is the temperature at a depth of 10 m, since it avoids seasonal temperature variations [42] which only immediately affect the first 10 m of ice. Figure 5.2 displays the glacial ice temperature as a function of elevation above sea level along a flow line in Terre Adelie in Antarctica [42]. It can be seen that the surface temperature decreases markedly with increasing elevation. Any glacier exceeding roughly 1900 m in elevation seems to have a surface temperature beneath the -30^{o} C mark. Recall that at temperatures above -30^{o} C, ice temperature is the primary contributor to ice conductivity. However, the surface

temperature is typically the coldest temperature within the glacier, since the glacier temperature increases with depth.

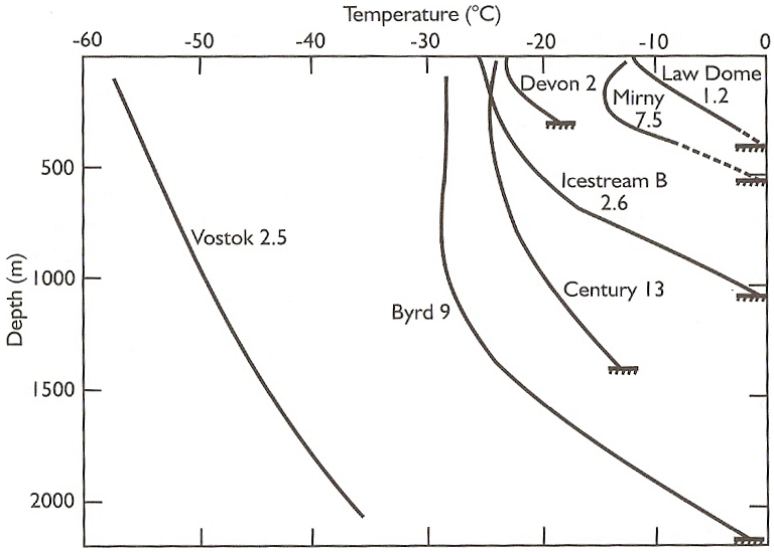

Figure 5.3 – Measured Temperature Profiles from Antarctica
The data was taken from accumulation areas. [34]

Figure 5.3 displays temperature profiles measured from ice cores in Antarctica. Also, Figure 5.4 displays an ice temperature profile from the GISP2 ice core from Summit Station in Greenland [14]. Each of these ice cores were obtained from accumulation areas, which are defined as areas with a net gain in ice mass over time. Accumulation areas are usually located further inland on an ice sheet [34]. In contrast, an ablation area is defined as having a net loss of ice mass over time. Ablation areas are usually located closer to the coast on an ice sheet [34].

From Figures 5.3 and 5.4, it can be seen that with the exception of Vostok, each of the temperature profiles are well above -30^{o} C. Vostok is the exception since it is located near the South Geomagnetic Pole at an elevation above sea level of 3488 m. Also, with an average winter temperature of -65^{o} C, the coldest recorded temperature on Earth of -89.2^{o} C was recorded at Vostok. In contrast, Summit Station in Greenland, at an elevation above sea level of 3200 m, is located at the highest point

in the Arctic, yet has a significantly warmer temperature profile than Vostok. Therefore, with the exception of areas near Vostok and the South Pole, the majority of glacial ice temperatures are near or below -30^{o} C, at least during summer months, at which time field research is usually conducted.

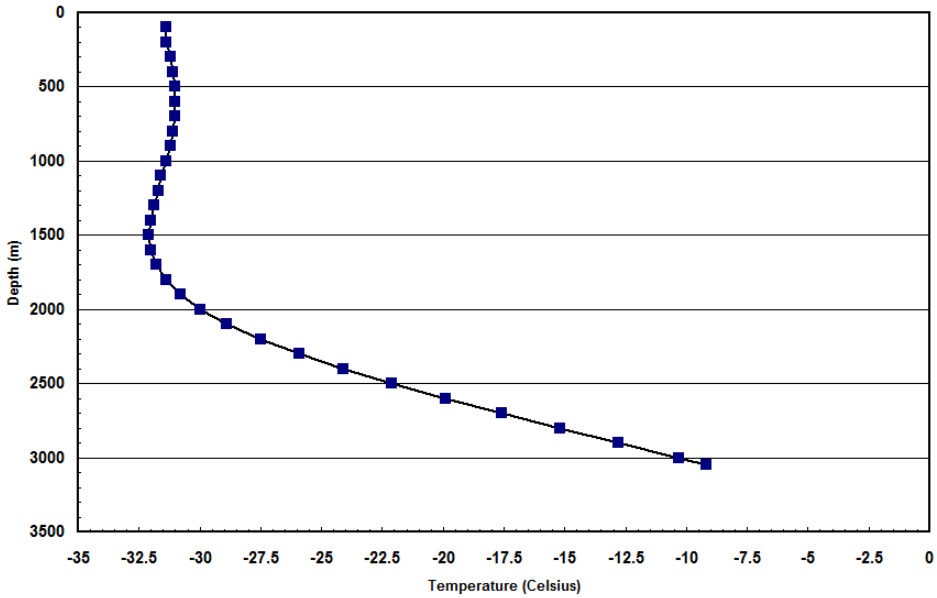

Figure 5.4 – Measured Temperature Profile from Greenland
The data was taken from the GISP2 ice core from Summit Station [2]

As shown throughout this section, for the majority of cases, the assumption that conductivity is temperature driven is reasonable. Conductivity is the primary cause of loss within glacial ice, and can be accounted for by the complex permittivity ε, as shown in Equation 5.7. Now, it is necessary to present the temperature dependence of ε and how it relates to attenuation.

5.4 Relation of Attenuation to Ice Permittivity and Temperature

The majority of the material in Section 5.4 was originally presented by Li, Xie, and Dobbs in [27].

The attenuation (loss) within glacial ice can be entirely accounted for by the complex permittivity ε as shown in Equation 5.7. Both the real and imaginary parts of ε exhibit temperature dependence. Based on the work in [29],

$$\varepsilon_r^{'}(T) = 3.1884 + (0.00091)T \qquad \textbf{Eq. 5.10}$$

where T is the temperature in degrees Celsius. Also, as shown in [1]

$$\varepsilon_r^{''}(f,T) = \frac{1}{10f} 10^{-2.02+0.025T} \qquad \textbf{Eq. 5.11}$$

where f is the operating frequency of the radar system in GHz.

Generally, for lossy media, the wavenumber is complex and is represented by

$$k = \sqrt{-j\omega\mu(\sigma + j\omega\varepsilon)} \qquad \textbf{Eq. 5.12}$$

where μ equals the free-space magnetic permeability (4π x10^{-7} H/m), since glacial ice is non-magnetic. However, since conductivity was accounted for by $\varepsilon_r^{''}$ in Equation 5.7, k can be simplified to

$$k = \omega\sqrt{\mu\varepsilon} \qquad \textbf{Eq. 5.13}$$

The complex propagation constant is related to k via the following

$$\gamma = jk = \alpha + j\beta \qquad \textbf{Eq. 5.14}$$

where α is the attenuation constant (Np/m) and β is the phase constant (rad/m). Taking the real and imaginary parts of *jk* and doing some rearrangement results in

$$\alpha = 2\pi f \left[\frac{\mu_o \varepsilon_o \varepsilon_r^{'}}{2} \left(\sqrt{1 - \tan^2 \delta} - 1 \right) \right]^{1/2} \qquad \textbf{Eq. 5.15}$$

and

$$\beta = 2\pi f \left[\frac{\mu_o \varepsilon_o \varepsilon_r^{'}}{2} \left(\sqrt{1 - \tan^2 \delta} + 1 \right) \right]^{1/2} \qquad \textbf{Eq. 5.16}$$

where $\tan\delta$ is the loss tangent described by

$$\tan\delta = \frac{\varepsilon_r^{''}}{\varepsilon_r^{'}} \qquad \textbf{Eq. 5.17}$$

Equation 5.15 relates the attenuation α to the complex permittivity ε of the ice, which is itself a function of temperature. Therefore, the ability to measure attenuation at each depth within glacial ice should enable the determination of temperature at each depth. The measurement of attenuation at each depth using radar echoes from the two CMP configurations is discussed next.

5.5 Attenuation Extraction from Radar Echoes

The majority of the material in Section 5.5 was originally presented by Li, Xie, and Dobbs in [27].

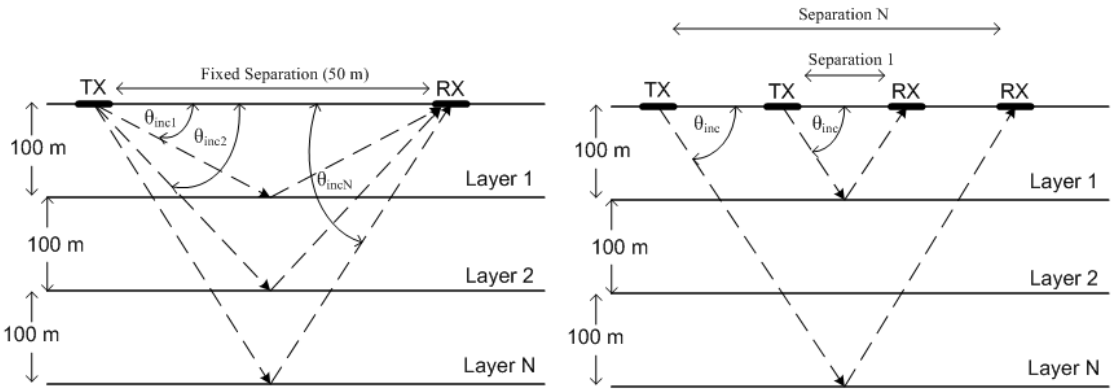

Figure 5.5 – Bistatic-Radar Common Midpoint Configurations

(a) Configuration 1 – Fixed Separation (b) Configuration 2 – Fixed Incident Angle

In order to determine the ice attenuation as a function of depth, two different transmit and receive antenna common mid-point radar geometries are used: one incorporating a fixed antenna separation at each depth (configuration 1) as shown in Figure 5.5(a), and one incorporating a fixed incident angle at each depth (configuration 2), as shown in Figure 5.5(b). Figure 5.5 generalizes the two radar configurations to *N* layers, with a fixed layer separation of 100 m in each configuration.

In order to clarify the radar configurations in deriving the ice attenuation from radar returns, Figure 5.6 is used. This figure presents the geometric variables associated with extracting attenuation from a single layer.

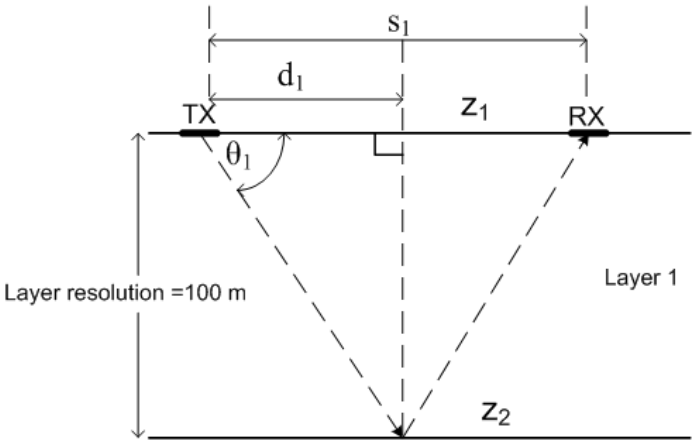

(a) Configuration 1

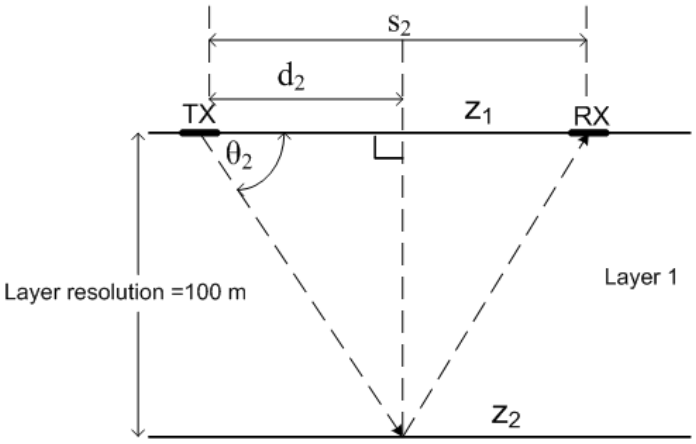

(b) Configuration 2

Figure 5.6 – Common Mid-Point Radar Set-Ups for Layer 1

The radar equations for the common mid-point sounding geometry are

$$P_{r1}(z) = \frac{P_t G^2(z,\theta_1)\lambda^2 \Gamma_{ice}}{L_1(z,\theta_1)[8\pi R_1(z,\theta_1)]^2} \qquad \textbf{Eq. 5.18}$$

$$P_{r2}(z) = \frac{P_t G^2(z,\theta_2)\lambda^2 \Gamma_{ice}}{L_2(z,\theta_2)[8\pi R_2(z,\theta_2)]^2} \qquad \textbf{Eq. 5.19}$$

where Equation 5.18 is associated with configuration 1 and Equation 5.19 is associated with configuration 2. The loss incurred by the received signal in each configuration is related to the attenuation $\alpha(z)$ by

$$L_1(z,\theta_1) = e^{2\int_0^z \alpha(z')\sec\theta_1 dz'} \quad \textbf{Eq. 5.20}$$

$$L_2(z,\theta_2) = e^{2\int_0^z \alpha(z')\sec\theta_2 dz'} \quad \textbf{Eq. 5.21}$$

Also, the incident angles and ranges shown in Figure 5.6 are determined by

$$\theta_1(z,d_1) = \tan^{-1}\left(\frac{d_1}{z}\right) \quad \textbf{Eq. 5.22}$$

$$\theta_2(z,d_2) = \tan^{-1}\left(\frac{d_2}{z}\right) \quad \textbf{Eq. 5.23}$$

$$R_1(z,\theta_1) = \frac{z}{\cos\theta_1} \quad \textbf{Eq. 5.24}$$

$$R_2(z,\theta_2) = \frac{z}{\cos\theta_2} \quad \textbf{Eq. 5.25}$$

Dividing Equation 5.19 by 5.18, assuming Γ_{ice} is specular, and doing some rearrangement results in

$$\frac{L_1(z,\theta_1)}{L_2(z,\theta_2)} = \frac{G^2(z,\theta_1)P_{r2}(z)R_2^2(z,\theta_2)}{G^2(z,\theta_2)P_{r1}(z)R_1^2(z,\theta_1)} = \frac{G^2(z,\theta_1)P_{r2}(z)\cos^2\theta_1}{G^2(z,\theta_2)P_{r1}(z)\cos^2\theta_2} \quad \textbf{Eq. 5.26}$$

Next, dividing Equations 5.20 by 5.21 results in

$$\frac{L_1(z,\theta_1)}{L_2(z,\theta_2)} = e^{2\int_0^z \alpha(z')(\sec\theta_1 - \sec\theta_2)dz'} \quad \textbf{Eq. 5.27}$$

Equation 5.27 can be rearranged to the following

$$\int_0^z \alpha(z')dz' = \ln\left[\frac{L_1(z,\theta_1)}{L_2(z,\theta_2)}\right]\left[\frac{1}{2(\sec\theta_1 - \sec\theta_2)}\right] \qquad \textbf{Eq. 5.28}$$

Plugging Equation 5.26 into Equation 5.28 yields a relationship between the accumulated attenuation over a depth *z* and the power received from that depth

$$\int_0^z \alpha(z')dz' = \ln\left[\frac{G^2(z,\theta_1)P_{r2}(z)\cos^2\theta_1}{G^2(z,\theta_2)P_{r1}(z)\cos^2\theta_2}\right]\left[\frac{1}{2(\sec\theta_1 - \sec\theta_2)}\right] \quad \textbf{Eq. 5.29}$$

The ice attenuation over a single resolution layer Δz at a depth z_i can be obtained by subtracting the contributions from all layers previous to z_i from the accumulated attenuation

$$\alpha(z_i) = \int_0^{z_i} \alpha(z')dz' - \Delta z\sum_{k=1}^{i-1}\alpha(z_k) \qquad \textbf{Eq 5.30}$$

Equations 5.30 and 5.29 can be used to determine the attenuation at any depth within glacial ice from knowledge of the received power, incident angles, and far-zone antenna gain. The next section deals with relating the measured attenuation to temperature.

5.6 Temperature Extraction from Measured Attenuation

The majority of the material in Section 5.6 was originally presented by Li, Xie, and Dobbs in [27].

Extraction of temperature from measured attenuation involves representing $\alpha(z)$ from Equation 5.15 in terms of the temperature-dependent complex

permittivity ε. However, prior to doing so, for low-loss dielectrics ($\tan\delta << 1$), the following simplification can be made for $\alpha(z)$ [11]

$$\alpha(z) = \frac{\pi f \sqrt{\varepsilon_r^{'}} \tan\delta}{c} = \frac{\pi f \varepsilon_r^{''}}{c\sqrt{\varepsilon_r^{'}}} \qquad \textbf{Eq. 5.31}$$

To see if the low-loss approximation of Equation 5.31 is acceptable for glacial ice, consider σ of 0.00001 S/m [2] at a frequency *f* of 200 MHz (frequency used in ice-penetrating radar), and a dielectric constant $\varepsilon_r^{'}$ of 3.2 (that of fully compressed ice). Determining $\varepsilon_r^{''}$ using the above information and Equation 5.7 yields a loss tangent $\tan\delta$ of 0.00028, which is much less than 1.

Plugging Equations 5.11 and 5.12 into 5.31 yields

$$\alpha(z) = \frac{\pi 10^{-2.02+0.025T}}{3\left(3.1884 + (0.00091)T\right)^{1/2}} \qquad \textbf{Eq 5.32}$$

Rearranging Equation 5.32 and squaring both sides results in the following transcendental equation relating temperature *T(z)* to attenuation $\alpha(z)$

$$\left[\frac{3\alpha(z)}{\pi}\right]^2 \left[3.1884 + (0.00091)T(z)\right] - 10^{-4.04+0.05T(z)} = 0 \qquad \textbf{Eq. 5.33}$$

Equation 5.33 can be solved numerically to determine the temperature as a function of depth within glacial ice. The next section presents resulting temperature profiles obtained using Equation 5.33 and simulated data.

5.7 Simulated Temperature Profile Results

Four sets of simulated results were calculated from using three measured temperature profiles [2]. The temperature profiles, shown in Figure 5.7, include one from the GRIP [16] ice core, and two hypothetical profiles, called Hypothetical 1 (Hypo. 1) and Hypothetical 2 (Hypo. 2). From these measured temperature profiles, received power was simulated. Then, from the simulated received power, temperature profile extraction was simulated. In the first set of simulated results, temperature profiles were extracted assuming ideal conditions (no gain estimation error). In the second set, temperature was extracted while neglecting the depth-dependent refractive properties of glacial ice. The third set involved extracting temperature while assuming an error in the ice density profile model. Finally, in the fourth set, temperatures were extracted using a Hertzian dipole in free-space for the estimated antenna gain. All of the results obtained in this section where produced using the *IceTemp.m* Matlab script, which is shown in Appendix C.

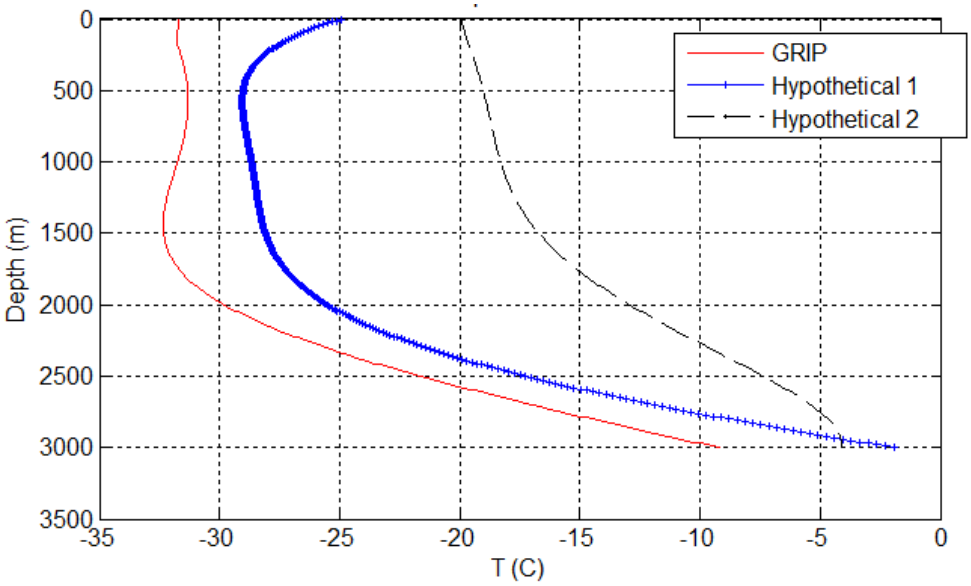

Figure 5.7 – Measured Temperature Profiles used for Simulation

Each of the three simulated sets of results involved an identical procedure for simulating received power. The equations used for simulating received power are presented in Section 5.6, but are repeated here for clarity. First, from the measured temperature profiles, real and imaginary permittivites were calculated for each depth using the following

$$\varepsilon_r^{'}(z) = 3.1884 + (0.00091)T(z) \qquad \textbf{Eq. 5.34}$$

$$\varepsilon_r^{''}(z) = \frac{1}{10f} 10^{-2.02+0.025T(z)} \qquad \textbf{Eq. 5.35}$$

Then, from the calculated values of $\varepsilon_r^{'}(z)$ and $\varepsilon_r^{''}(z)$, the attenuation at each depth was calculated using

$$\alpha(z) = 2\pi f \left[\frac{\mu_o \varepsilon_o \varepsilon_r^{'}(z)}{2} \left(\sqrt{1 - \tan^2 \delta(z)} - 1 \right) \right]^{1/2} \qquad \textbf{Eq. 5.36}$$

The attenuation is related to the total loss incurred by the received power from each depth by

$$L_1(z, \theta_1) = e^{2\int_0^z \alpha(z') \sec\theta_1 dz'} \qquad \textbf{Eq. 5.37}$$

$$L_2(z, \theta_2) = e^{2\int_0^z \alpha(z') \sec\theta_2 dz'} \qquad \textbf{Eq. 5.38}$$

Knowing the accumulated loss at each depth from Equations 5.37 and 5.38, and using the appropriate formulas from Section 5.6 for describing the geometries of radar configurations 1 and 2, allows the received power to be simulated using

$$P_{r1}(z) = \frac{P_t G^2(z,\theta_1)\lambda^2 \Gamma_{ice}}{L_1(z,\theta_1)[8\pi R_1(z,\theta_1)]^2} \quad \textbf{Eq. 5.39}$$

$$P_{r2}(z) = \frac{P_t G^2(z,\theta_2)\lambda^2 \Gamma_{ice}}{L_2(z,\theta_2)[8\pi R_2(z,\theta_2)]^2} \quad \textbf{Eq. 5.40}$$

Once the received power is known and the antenna gain at each depth is estimated, the attenuation at each depth can be extracted using

$$\int_0^z \alpha(z')dz' = \ln\left[\frac{G^2(z,\theta_1)P_{r2}(z)\cos^2\theta_1}{G^2(z,\theta_2)P_{r1}(z)\cos^2\theta_2}\right]\left[\frac{1}{2(\sec\theta_1 - \sec\theta_2)}\right] \quad \textbf{Eq. 5.41}$$

$$\alpha(z_i) = \int_0^{z_i} \alpha(z')dz' - \Delta z \sum_{k=1}^{i-1} \alpha(z_k) \quad \textbf{Eq. 5.42}$$

Note that the Vivaldi antenna (Chapter 4) was used for calculating antenna gain in Equations 5.39, 5.40, and 5.41. Once the attenuation at each depth has been extracted, the temperature at each depth can be extracted using

$$\left[\frac{3\alpha(z)}{\pi}\right]^2 \left[3.1884 + (0.00091)T(z)\right] - 10^{-4.04+0.05T(z)} = 0 \quad \textbf{Eq. 5.43}$$

The purpose of the simulations in Section 5.7 was to explore the effect of antenna-gain estimations on the ability to extract glacial-ice temperature profiles. There are other possible sources of error in determining glacial-ice temperature profiles that are not investigated in this work. These include possible inaccuracies in the temperature extraction algorithm, the possibility of the internal ice reflectivity being a function of polarization and incident angle, and the signal to noise ratio. Since in these temperature profile extraction simulations, the same algorithm was used to simulate received power, as was used to extract temperature, inaccuracies in the temperature extraction algorithm could not be explored in this work. The effect of

polarization and incident angle could have been explored in this work, but that in of it self would involve internal layering assumptions. The effect of noise was explored in [27], and is therefore not repeated here.

5.7.1 Simulated Temperature Extraction under Ideal Conditions

The majority of the material in Section 5.7.1 was originally presented by Li, Xie, and Dobbs in [27].

In this idealized simulation, there was no antenna gain estimation error. Also, since the same antenna gain was used to simulate values of P_r, as was used to extract $\alpha(z)$, the antenna gain had no effect on the results. Table 5.1 lists the parameters used to perform this simulation. The fixed value of θ_I in Configuration 2 is half the critical angle [11] determined using a value of 3.2 for the ice dielectric constant. This incident angle insures that the critical angle is never exceeded.

Table 5.1 - Ideal Temperature Profile Extraction Simulation Parameters

Variable	Configuration 1	Configuration 2	Description
P_t	800 W	800 W	Transmitted Power
Z_r	100 m	100 m	Depth Resolution
θ_I	variable	18.7 degrees	Incident Angle
R	50 m	variable	separation between transmit and receive antennas
Γ	-80 dB	-80 dB	reflectivity between layers
f	210 MHz	210 MHz	frequency

Figure 5.8 compares the measured temperature profiles to the simulated results obtained assuming ideal conditions. Although the measured and simulated results in Figure 5.8 are not identical, they are very similar.

Figure 5.9 quantifies the error between simulated and measured temperature profiles. The hypothetical 2 profile performed the best, with the error being constrained to within -0.5^o C. The GRIP and hypothetical 1 profiles did not perform as well, with the error exceeding -1^o C for depths below 2500 m.

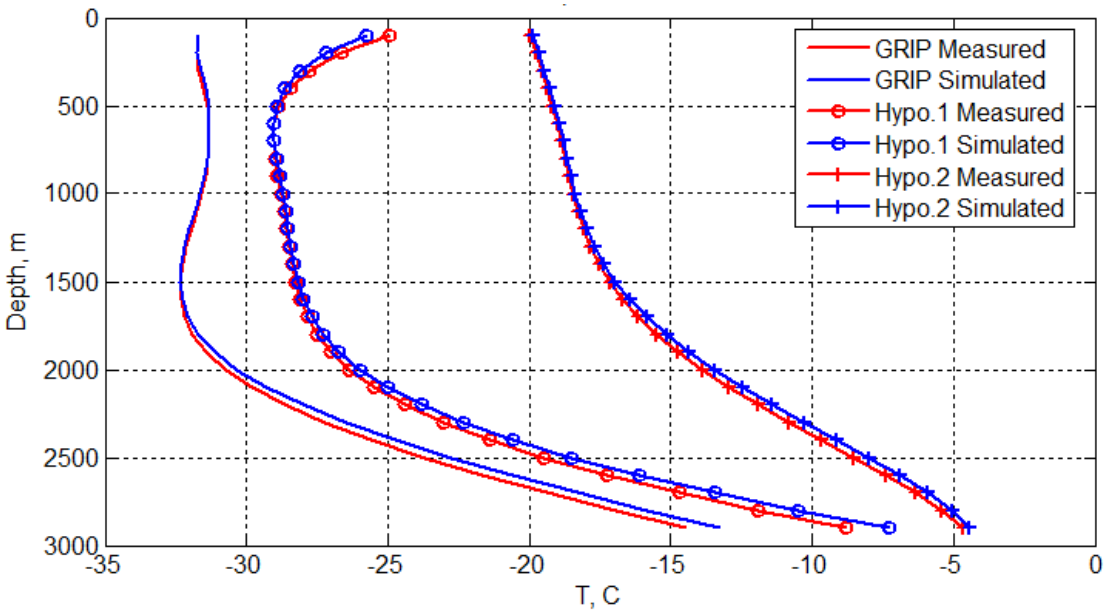

Figure 5.8 –Measured/Simulated Temperature Profiles (Ideal Case)

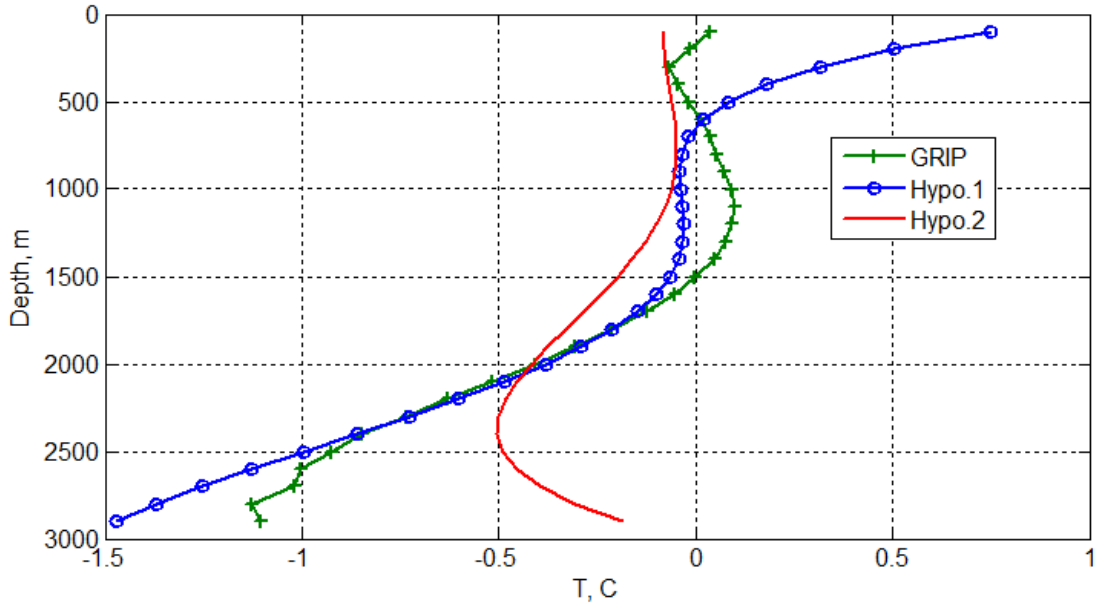

Figure 5.9 – Temperature Extraction Error (Ideal Case)

Results comparing the measured and simulated attenuation are also presented. Figure 5.10 compares the measured and simulated attenuation profiles, and Figure

5.11 displays the error between measured and simulated attenuation profiles. In Figure 5.11, there is good agreement between measured and simulated attenuation profiles, which mimics the agreement for temperature profiles shown in Figure 5.8. In Figure 5.11, the error is constrained between 0 and 1.5 x 10^{-4} Np/m for most of the data points. Only the hypothetical 1 profile has error values significantly exceeding this range.

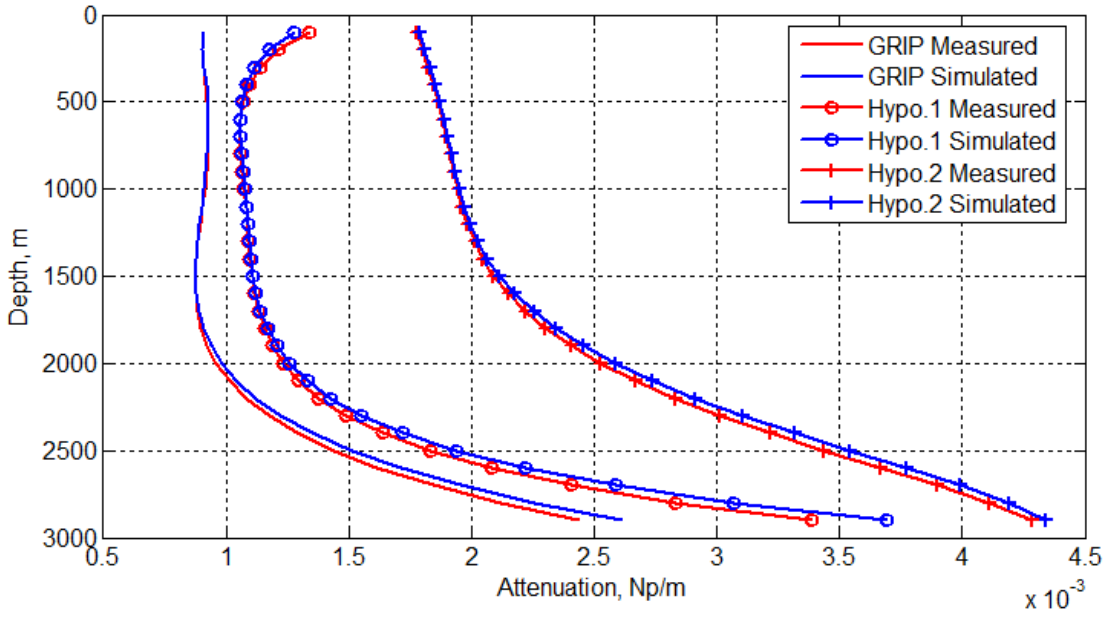

Figure 5.10 – Measured/Simulated Attenuation Profiles (Ideal Case)

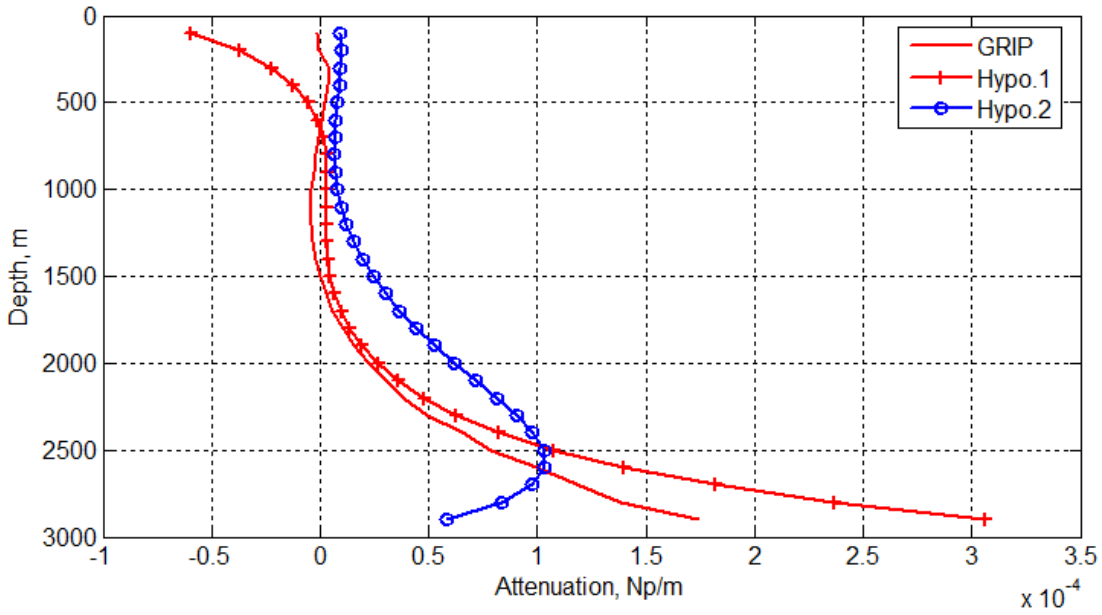

Figure 5.11 – Attenuation Extraction Error (Ideal Case)

5.7.2 Effect of Neglecting Refractive Gain on Temperature Extraction

In this simulation, the ice was treated as a homogeneous half-space in regards to extracting ice temperature profiles. Therefore, the refractive gain of the ice was neglected. Figure 5.12(a) shows the error between simulated and measured temperature profiles. The error is extreme for the first 500 m, with the error magnitude exceeding 50^{o}C at one depth. But, the error does become less significant below 800 m. Figure 5.12(b) provides a zoomed in version of Figure 5.12(a), and only displays depths from 700 m and deeper. From Figure 5.12(b), it can be seen that the magnitude of the error is constrained to within 2^{o}C below 900 m. Also, Figure 5.13 compares the measured and simulated temperature profiles.

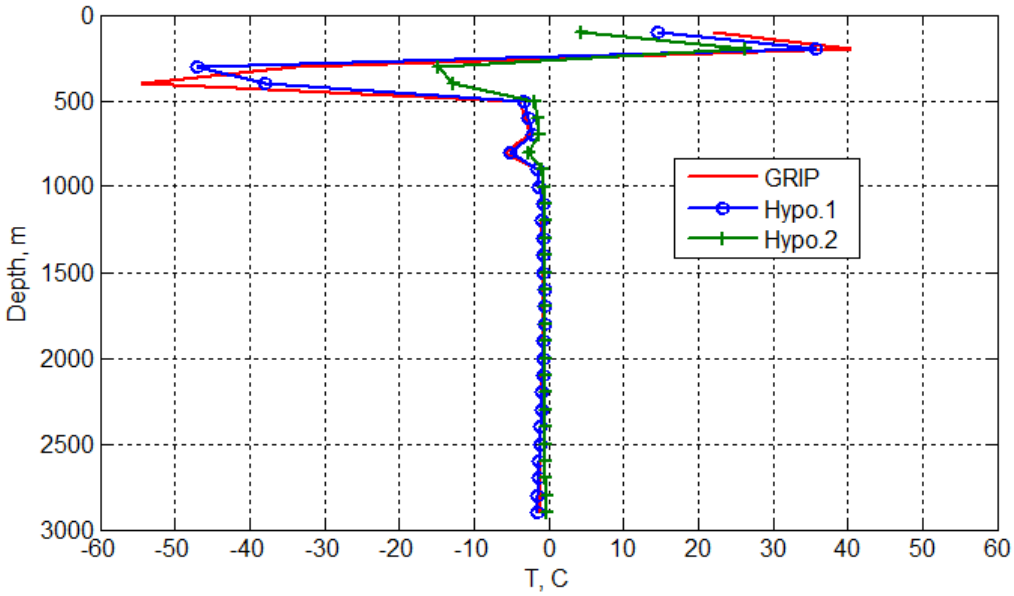

(a)

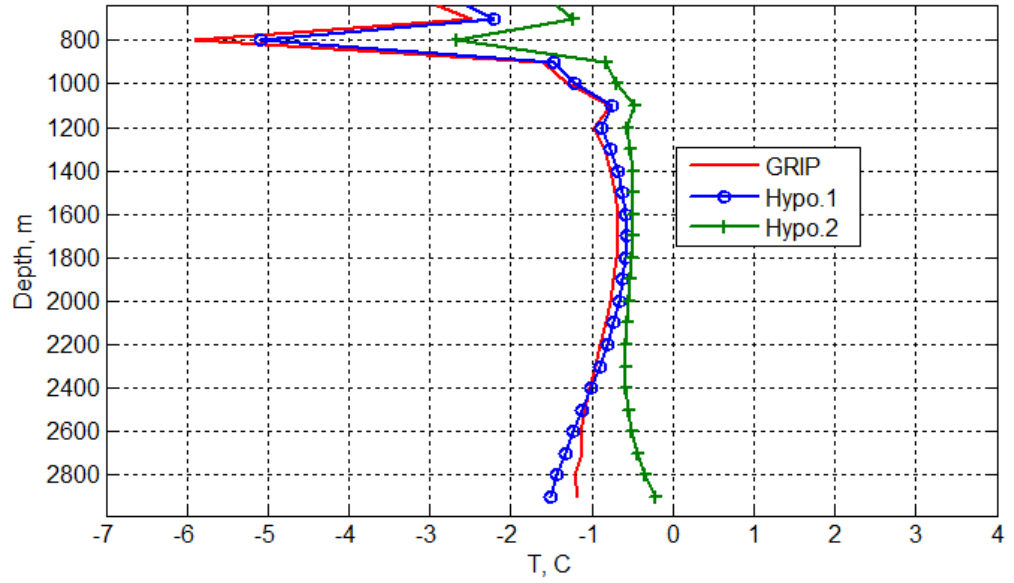

(b)

Figure 5.12 – Error between Simulated/Measured Temperature Profiles (Ignoring Refractive Gain)

(a) All Depths (b) Zoomed In

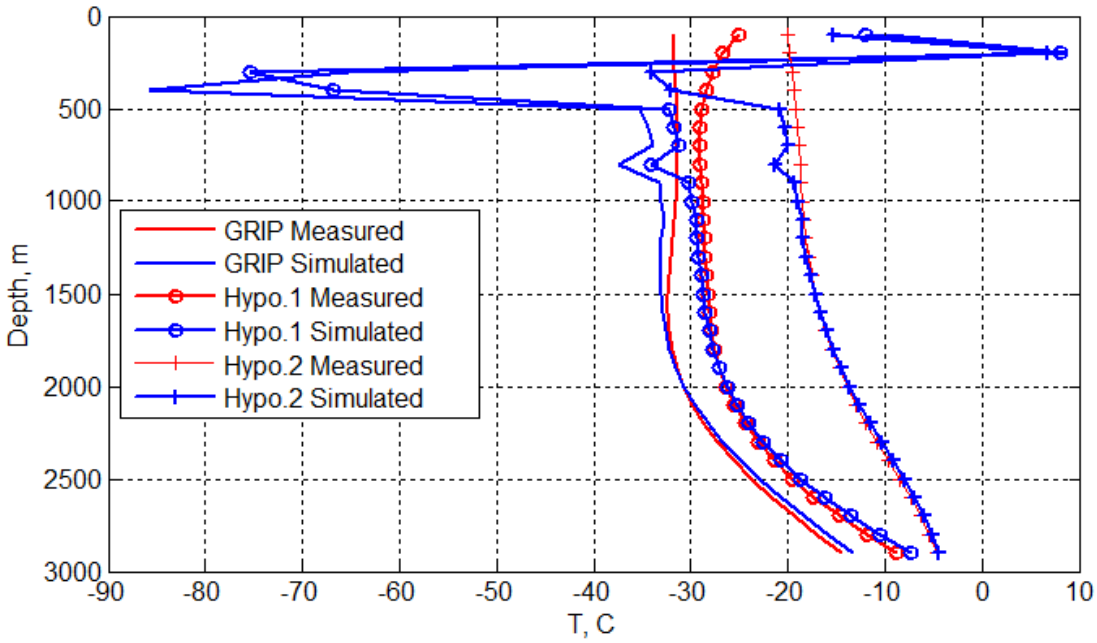

Figure 5.13 – Measured/Simulated Temperature Profiles (Ignoring Refractive Gain)

From Figures 5.12 and 5.13, it is apparent that neglecting the refractive gain of glacial ice when estimating antenna gain severely affects the ability to accurately extract temperature profiles using radar, at least at shallower depths. This is because the more the density profile changes with depth, the more the antenna gain pattern changes spatially with depth. Eventually, a depth is reached (800 m in this case), at which the gain estimation error for each radar configuration is essentially constant as a function of depth. The usage of 2 radar configurations nearly cancels out the effects of any magnitude-only error in antenna gain estimation (see Equation 5.41 and 5.42). Only spatial variations in the antenna gain, which occur at shallower depths, significantly affect the accurate calculation of ice attenuation via Equation 5.41 and 5.42, and thus the extraction of temperature as a function of depth. Figure 5.14 plots the antenna-gain estimation error as a function of depth in dB. Here the gain error can basically be considered as additive noise. The error is less than -25 dB for depths greater than 800 m in this case.

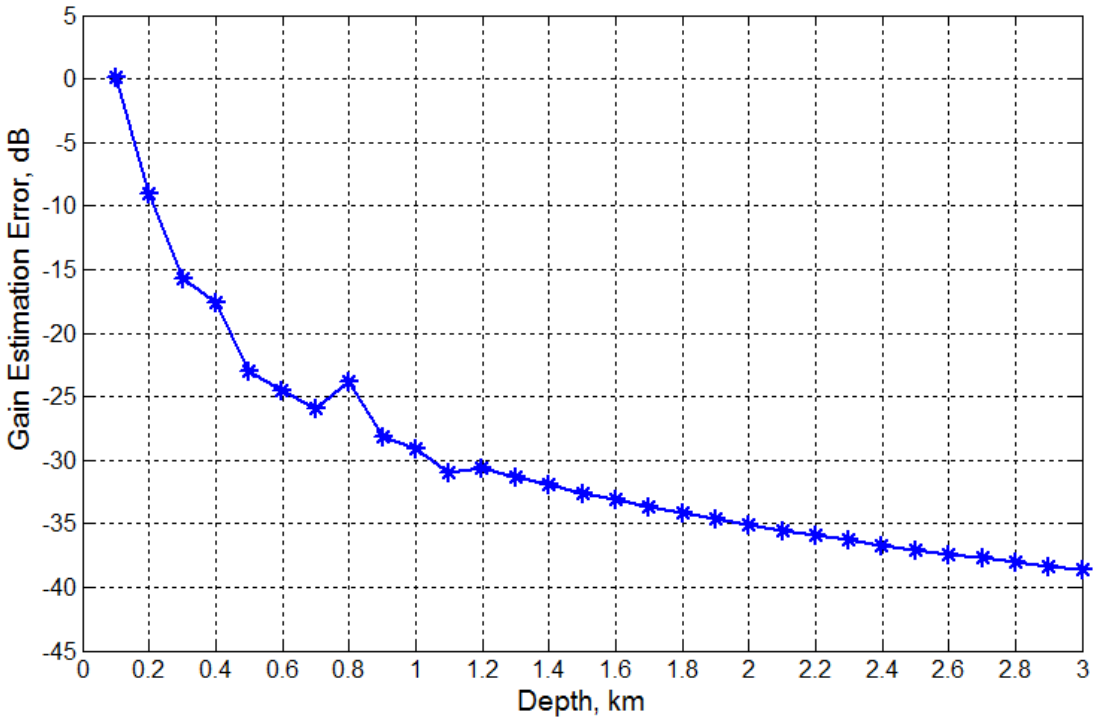

Figure 5.14 – Antenna-Gain Estimation Error in dB (Ignoring Refractive Gain)

5.7.3 Effect of Ice Density Profile Error on Temperature Extraction

In this simulation, an incorrect ice density profile was used to estimate antenna gain, when extracting ice temperature profiles. The received power is simulated using antenna gain obtained from the Greenland density profile model, and the glacial ice temperature is extracted using antenna gain obtained from either the Profile 1 or Profile 2 density profile models discussed below.

Table 5.2 – Density Profile Empirical Constants

	Antarctica	Greenland	Profile 1	Profile 2
V:	0.52	0.55	0.52	0.55
R:	-0.033	-0.022	-0.04	-0.018

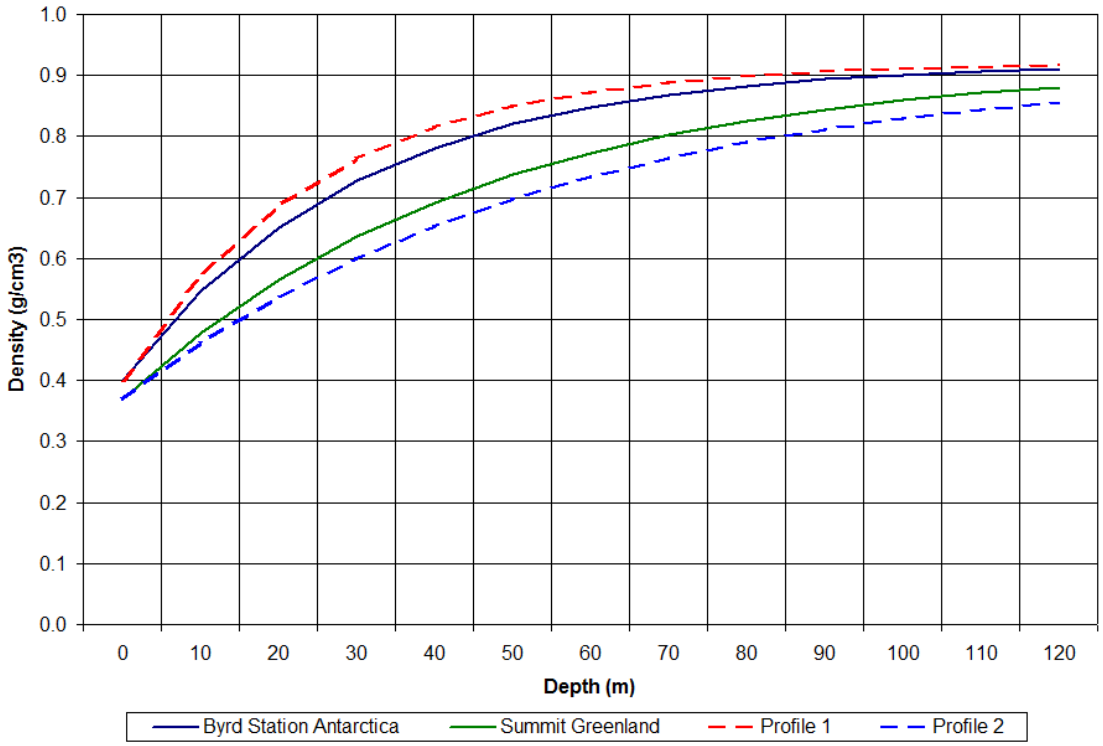

Figure 5.15 – Density Profiles

Profile 1 and Profile 2 were created using the empirical constants shown in Table 5.2. Figure 5.15 compares the two hypothetical density profiles with the Antarctic and Greenlandic density profiles discussed in Chapter 3. From Table 5.2 and Figure 5.15, it can be seen that Profile 1 is similar to the Antarctic density profile, but has a slightly increased exponential growth. Also, Profile 2 is similar to the Greenlandic density profile, but has a slightly decreased exponential growth.

Figure 5.16 shows the temperature extraction error obtained when using the Profile 2 density model. The error is large for depths of roughly 250 m and less. However, below 250 m, the error is approximately the same as that obtained under ideal conditions (Figure 5.9). The error is greatest at shallower depths, because that is where the ice density, and thus the antenna gain, varies the most.

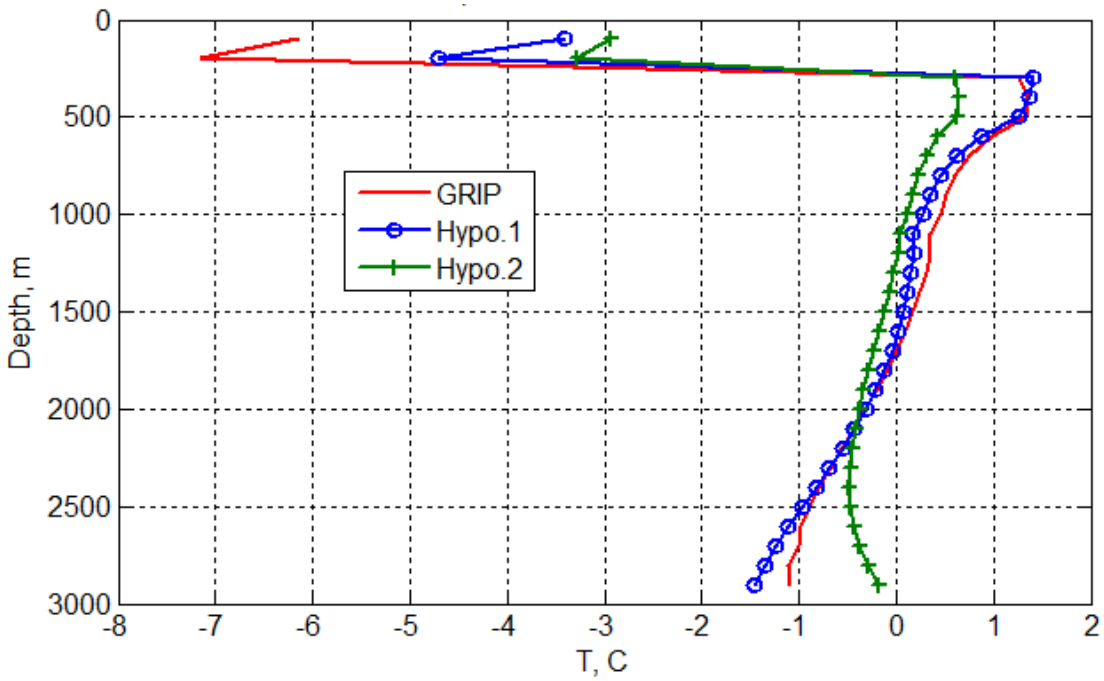

Figure 5.16 – Temperature Extraction Error (Profile 2 Density Model)

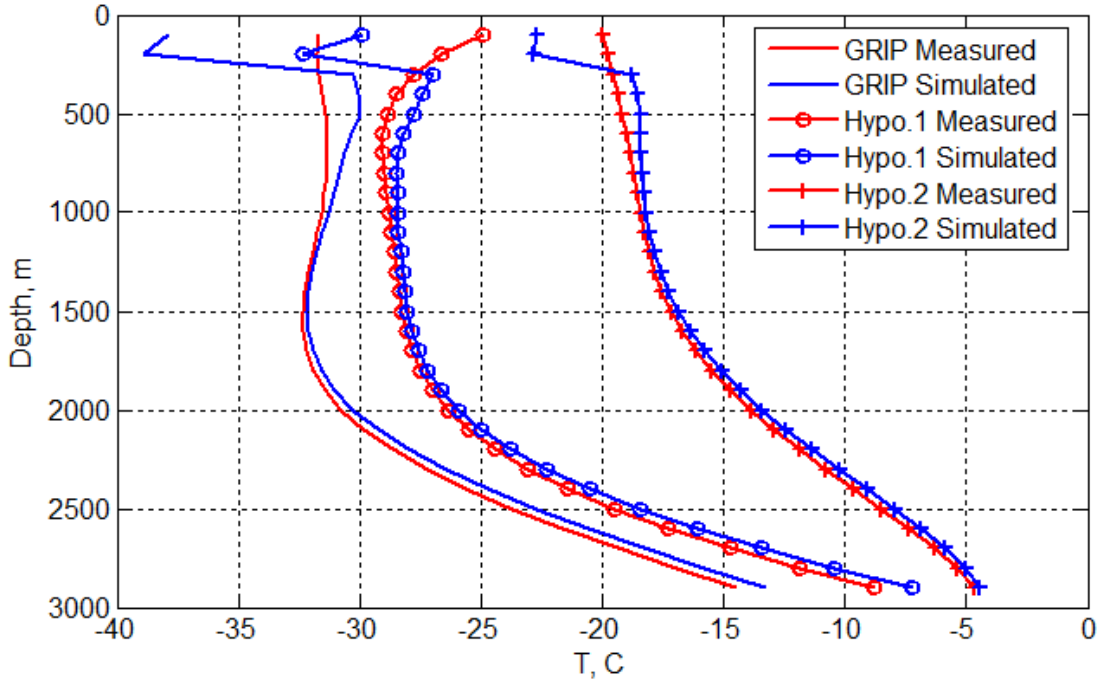

Figure 5.17 – Measured/Simulated Temperature Profiles (Profile 2 Density Model)

Figure 5.17 compares the measured temperature profiles with those temperature profiles obtained using the Profile 2 density model. The simulated temperature is underestimated at depths shallower than 250 m. Also, based on previously presented temperature profiles (Figures 5.3 and 5.4); the simulated profiles in Figure 5.17 seem to have an unnatural slope at depths shallower than 250 m. Therefore, it appears that incorrect density profile usage could be predicted if such unnatural looking temperature profile results are obtained in practice.

Temperature profile results were also simulated using the Profile 1 density model. As shown in Figure 5.15, the Profile 1 density profile is drastically different than the Greenland profile, so errors should be greater than those shown in Figure 5.16. Figure 5.18 displays the temperature extraction error obtained when using the Profile 1 density profile. The error exceeds 10^{o}C near the ice surface. As the depth increases, the error is reduced. Again, this is because the density profile changes the most near the surface, and the density becomes nearly constant below 100 m.

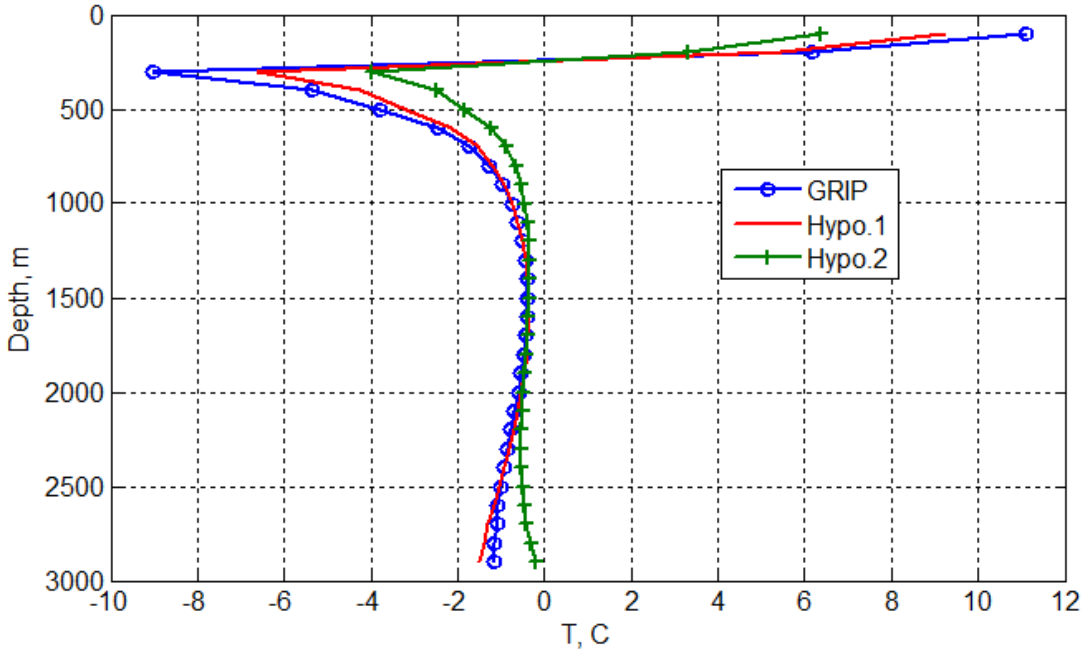

Figure 5.18 - Temperature Extraction Error (Profile 1 Density Model)

Figure 5.19 compares the measured temperature profiles with those temperature profiles obtained using the Profile 1 density model. The measured and simulated results are significantly different for the first 400 m. But, again the simulated results look unnatural at these depths based on known temperature profiles. Therefore, the error could be predicted in practice.

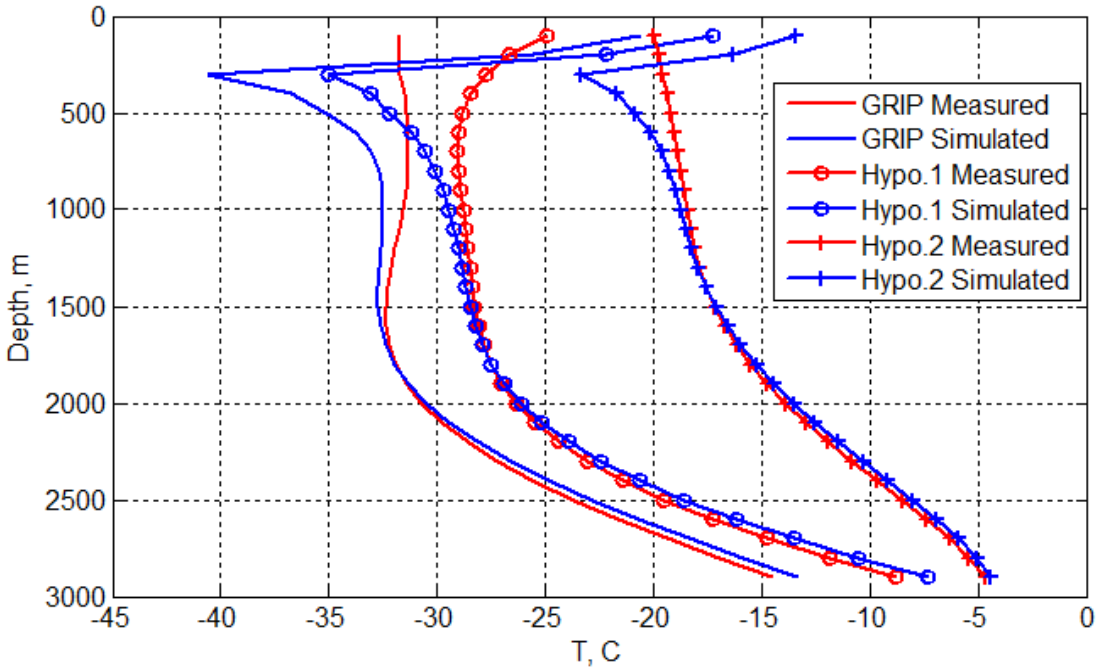

Figure 5.19 – Measured/Simulated Temperature Profiles (Profile 1 Density Model)

From the simulated temperature profile results shown in Figures 5.16 through 5.19, it can be seen that accurate predictions of density profiles are necessary in order to accurately extract temperature profiles. But, the effect of the usage of inaccurate density profiles is most pronounced within the first 400 m of ice. This is because the more the density profile changes with depth, the more the antenna gain pattern changes spatially with depth. At depths greater than 250 m, the antenna gain reaches a nearly constant pattern that is roughly the same regardless of the density profile used. Therefore, any error in the antenna gain estimation for radar configurations 1 and 2 is

an approximately constant value that is essentially eliminated through the mathematics of Equation 5.41 and 5.42.

Figure 5.20 plots the antenna-gain estimation error as a function of depth, for antenna gain obtained using both the Profile 2 and Profile 1 ice-density models. The antenna-gain estimation error is smaller for the gain estimated using the Profile 2 density model, since it is more similar to the Greenland density model (which was used to simulate received power) than is Profile 1.

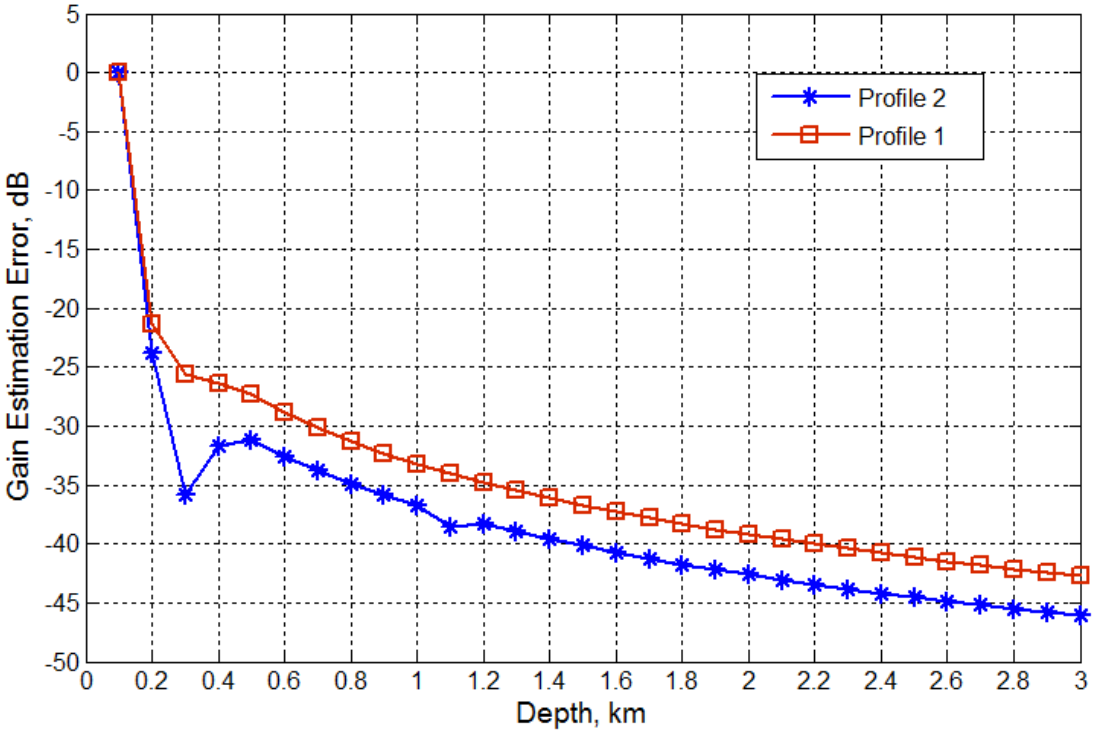

Figure 5.20 – Antenna-Gain Estimation Error in dB (Incorrect Density Profile)

Even though inaccurate ice density profile usage is not ideal, the usage of a reasonable, if not exact density profile, is superior than neglecting the refractive gain of ice altogether. The temperature extraction errors shown in Figures 5.16 and 5.18 (usage of incorrect density profile) are much less than that shown in Figure 5.12(a), where the density profile of ice is neglected entirely. Correspondingly, the antenna-

gain estimation error reaches a value of less than -25 dB at a depth of only 300 m when the reasonable Profile 2 and Profile 1 ice-density models were used, whereas an error of less than -25 dB was not reached until a depth of 800 m when the ice refractive gain was neglected.

5.7.4 Effect of Using a Free-Space Hertzian Dipole as Estimated Antenna Gain

In this simulation, the estimated antenna gain used for temperature extraction was that from a Hertzian dipole in free-space. As before, the received power was simulated using antenna gain obtained from the Vivaldi antenna and using the Greenland density profile model.

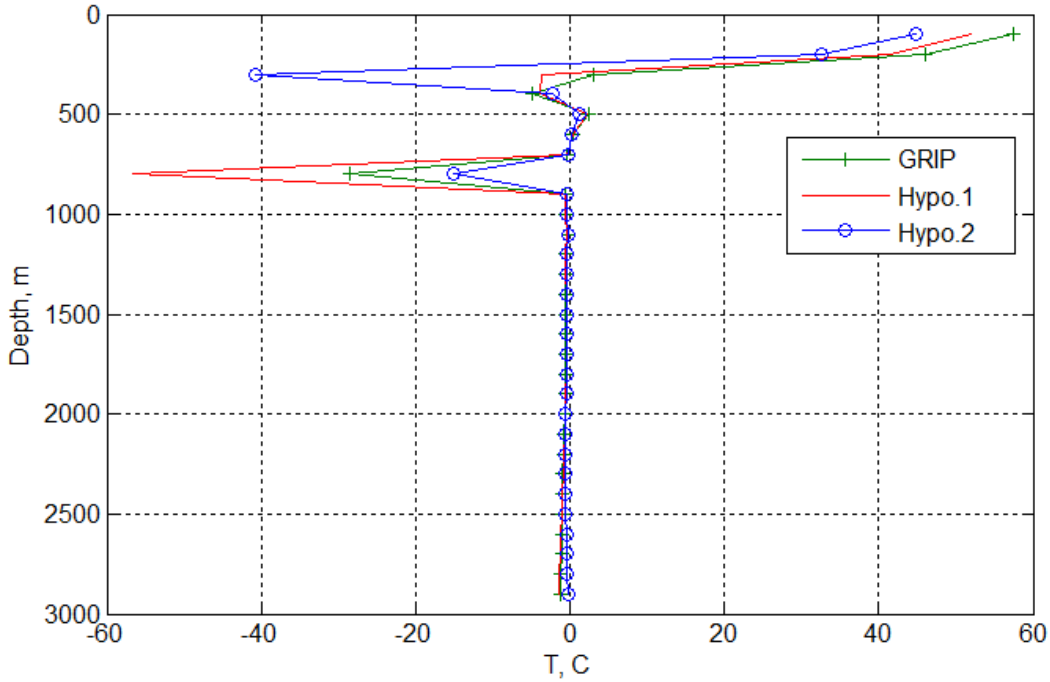

Figure 5.21 – Temperature Extraction Error (Free-Space Hertzian Dipole)

Figure 5.21 shows the temperature extraction error obtained when estimating antenna gain using a free-space Hertzian dipole. The error is large for depths of

roughly 1000 m and less. However, below 1000 m, the error is approximately the same as that obtained under ideal conditions (Figure 5.9). Again, the error is greatest at shallower depths, because that is where the ice density, and thus the antenna gain, varies the most. Also, Figure 5.22 compares the measured and simulated temperature profiles. The measured and simulated profiles compare favorably at depths greater than 1000 m.

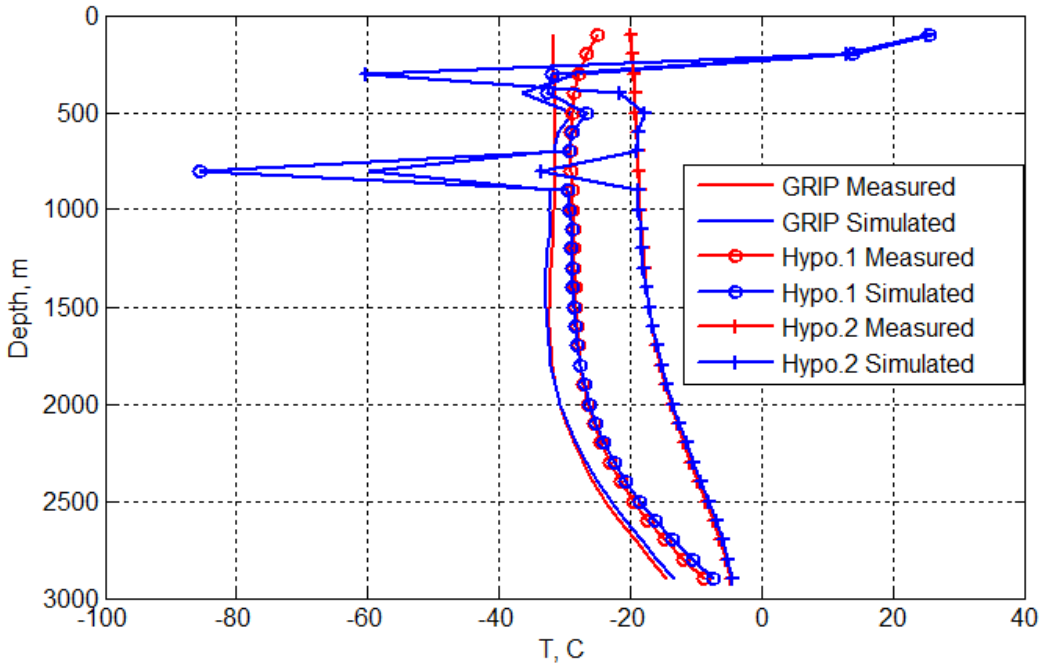

Figure 5.22 – Measured/Simulated Temperature Profiles (Free-Space Hertzian Dipole)

Figure 5.23 plots the antenna-gain estimation error as a function of depth, for antenna gain estimated from a Hertzian dipole in free-space. As with the other two cases of induced error, the estimation error decreases with increasing depth.

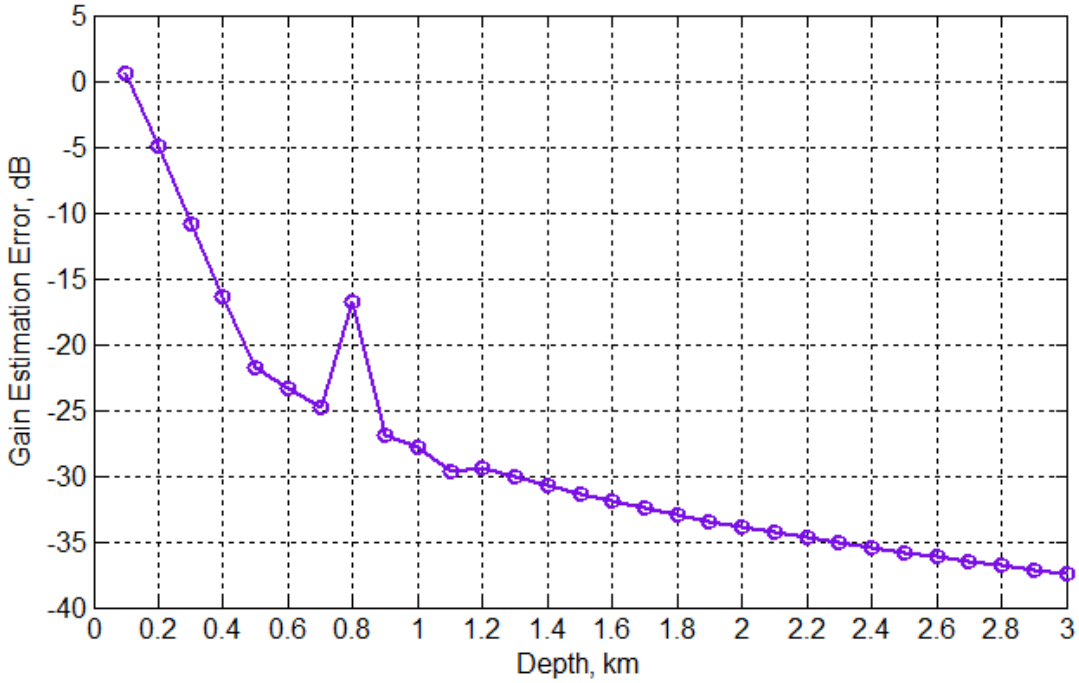

Figure 5.23 – Antenna-Gain Estimation Error in dB (Free-Space Hertzian Dipole)

5.8 Chapter 5 Results Summary

The effect of antenna-gain estimation error on temperature-extraction accuracy was explored in Section 5.7 of this chapter. Four different sources of antenna-gain estimation error were used, including: assuming homogeneous ice, using two different incorrect glacial-ice density profiles, and using a free-space Hertzian dipole as the antenna gain source. Each of these error sources yielded the surprising result that antenna-gain estimation has little effect on temperature-extraction accuracy deep within the ice. This is due to the eventual nearly-constant antenna gain patterns occurring within the ice at deep depths, and the mathematics of the attenuation extraction algorithm (see Equations 5.41 and 5.42). Usage of the two radar configurations provides two independent views at each depth-resolution layer, which significantly reduces the effects of any uncertainties in antenna gain.

Figure 5.24 plots the antenna-gain estimation error as a function of depth for each of the four induced-error scenarios. Each of the four curves in Figure 5.24

follows the same general trend. But, the curves produced for more accurate antenna-gain estimations yield the smallest error. The antenna-gain estimation error can be considered to be additive noise, affecting the attenuation measurement accuracy, and thus the temperature extraction accuracy.

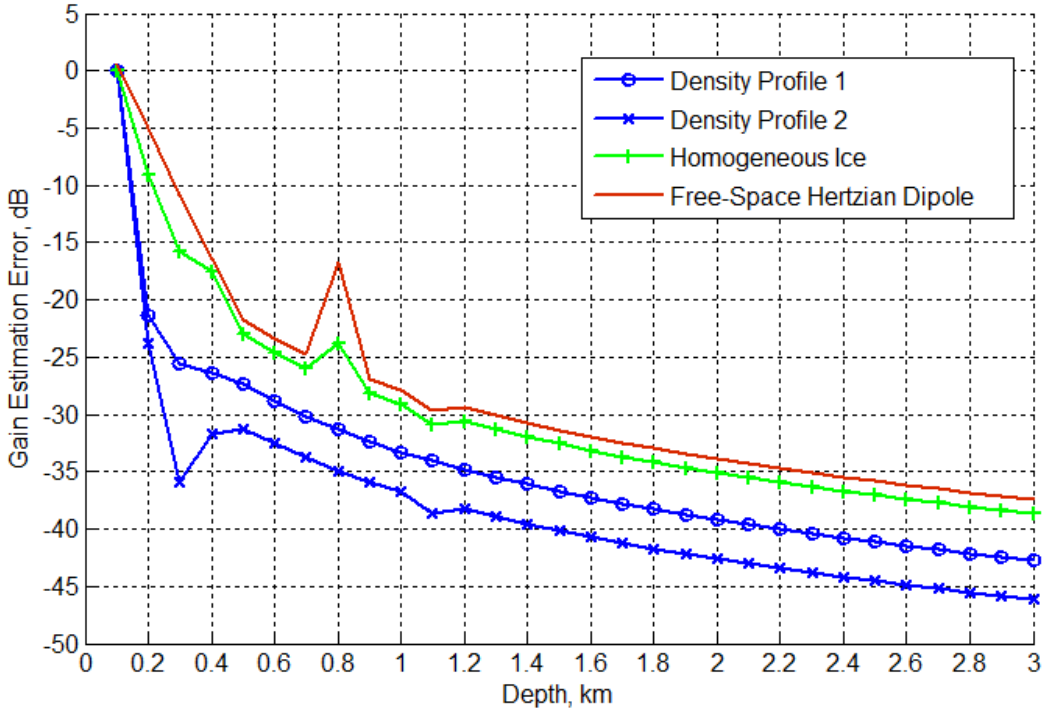

Figure 5.24 – Antenna-Gain Estimation Error in dB (All Error Sources)

Table 5.3 compares the four sources of antenna-gain estimation error, where usage of "Density Profile 2" yielded the most accurately-estimated antenna gain, and usage of "Free-Space Hertzian Dipole" yielded the least accurately-estimated antenna gain. The depth at which the antenna gain error begins to mimic that obtained under ideal conditions (Section 5.7.1) is listed. So, the more accurate the estimated antenna gain, the shallower is the depth at which extracted temperatures are as accurate as the ideal case.

Table 5.3 – Gain Estimation Error Comparison

Error Source	*Relative Approximation of Actual Gain	Depth at Which Gain Error is Similar to the Ideal Case
Density Profile 2	1	250 m
Density Profile 1	2	400 m
Homogeneous Ice	3	800 m
Free-Space Hertzian Dipole	4	1000 m
* 1 indicates it is most like the actual antenna gain		

CHAPTER 6: Summary/Conclusions/Future Work

The thesis work began under the assumption that accurate far-zone antenna-gain estimates are required in order to use ice-penetrating radar to accurately measure glacial ice temperature profiles. Therefore, this work set out to determine a method of accurately estimating the antenna-gain of ice-mounted antennas. First, the possible usage of commercial codes was explored, but it was found that although commercial codes are often used to determine far-zone antenna gain in free-space, these codes are incapable of doing so for ice-mounted antennas, due to the inhomogeneous dielectric constant of glacial ice. So, after some deliberation, a three-part hybrid numerical technique, called the FEM-NFFT-GO, was devised for accurately estimating the far-zone antenna gain within glacial ice. The FEM-NFFT-GO technique uses the FEM (finite element method) to calculate near-zone fields of the antenna, a dual-dielectric NFFT (near-to-far-field transformation) to determine the far-zone fields in the upper region of glacial ice, and the GO (geometric optics ray-tracing) technique to determine the far-zone fields at any depth within glacial ice. Results were presented that both validate the FEM-NFFT-GO technique, and highlight its ability to determine far-zone gain for complex ice-mounted antennas. Then, the glacial-ice temperature extraction algorithm was presented, as well as results relating the effects of antenna-gain estimation error on temperature profile extraction accuracy. Surprisingly, it was found that antenna-gain estimation errors only have a significant effect on temperature extraction at shallow depths within the ice. Regardless of the necessity of accurate antenna-gain estimations to extract glacial-ice temperatures, a powerful antenna-gain estimation technique was developed that should prove useful in many applications.

6.1 Antenna-Gain Estimation Summary

The FEM-NFFT-GO technique provides an invaluable tool with which to estimate far-zone antenna gain for ice-mounted antennas. This ability should prove to be a huge benefit to future glaciological research. The technique is easy to use, and is essentially a post-processing feature on top of the widely used HFSS antenna-analysis software.

Also, the FEM-NFFT-GO antenna gain estimation technique is useful for analyzing radiating structures in general, regardless of whether glacial ice is involved. The FEM-NFFT technique can be used alone to analyze radiating structures above an arbitrary half-space, which may be useful for ground-penetrating radar. Also, the GO portion of the technique can be adjusted to use refractive indexes following any mathematical trend.

The FEM-NFFT-GO technique relies on two assumptions in order to predict far-zone antenna gain accurately. First, this technique assumes that far-zone fields within the ice are planar prior to the ice dielectric constant changing significantly. Although this is a good approximation, it may not be entirely accurate. Field experiments will be required to determine the accuracy of this assumption. Second, the technique assumes that the glacial ice density profile is known with a high degree of accuracy. However, a reasonable approximation will suffice in most cases.

6.2 Effects of Antenna-Gain Estimation on Ice-Temperature Extraction Summary

As shown in Chapter 5, antenna-gain estimation error was shown to only have a significant effect on temperature extraction accuracy at shallow depths, where the definition of shallow depended upon the accuracy of the antenna-gain estimation. When the most accurate antenna-gain estimation error was used (a slight alteration to the glacial-ice density profile), the extracted temperatures were found to be nearly as

accurate as the ideal case for depths below 250 m. When the least accurate antenna-gain estimation error was used (gain estimated from free-space Hertzian dipole), the extracted temperatures were found to be nearly as accurate as the ideal case for depths below 1000 m.

The most probable source of error explored in Chapter 5 was the usage of an incorrect ice density profile for estimating far-zone antenna. This was found to adversely affect the temperature extraction accuracy, but again, only at shallow depths. Even when a significantly different density profile was used, the results were still favorable, and the extracted temperatures were found to be nearly as accurate as the ideal case for depths below 400 m.

6.3 Conclusions

The combination of the FEM-NFFT-GO antenna gain estimation technique along with the bistatic radar configurations discussed in Chapter 5 should enable glacial ice temperature profiles to be measured using ice-penetrating radar. Depending on the accuracy of the antenna-gain estimation, extracted temperatures will be accurate throughout most or all of the ice depth. However, if accurate ice temperatures are required only at very deep depths, accurate antenna-gain estimations are unnecessary.

This ability to measure glacial ice temperature via radar will make obtaining these profiles much easier, since ice-core drilling will no longer be required. The resulting potential increase in the availability of such data should further the science of glaciology, since ice temperature is fundamental in a variety of glacial processes [31]. An increased understanding of glacial processes will further science's understanding of how glaciers relate to the global climate.

6.4 Future Work

There is some future work to be carried out regarding both antenna-gain estimation for ice-mounted antennas and glacial-ice temperature extraction. To verify the accuracy of the FEM-NFFT-GO technique, field experiments need to be conducted to measure actual antenna patterns within glacial ice. This could be accomplished using a bistatic system and a calibration target.

Regarding temperature extraction, the effect of non-specular reflectivity and the accuracy of the temperature-extraction algorithm need to be investigated. As for non-specular reflectivity, the use of two independent measurements (combination of two radar configurations) at each depth-resolution layer should reduce any errors associated with non-specular reflectivity, provided the incident angles at the depth of interest are roughly the same for both radar configurations. This error reduction associated with non-specular reflectivity would be similar to what occurred with the antenna-gain estimation error.

The accuracy of the temperature-extraction algorithm can only be investigated by taking field measurements, using the temperature-extraction radar set-up, in regions with known temperature profiles. Then, the extracted temperature profiles from radar measurements can be compared with the known temperature profiles to investigate the accuracy of the technique.

APPENDIX A: Quasi-Far-Zone Field Derivation

In this section, the closed form solutions for far-zone fields radiated by electric and magnetic surface currents in the presence of a half-space of glacial ice are derived and presented. The derivation of these formulas involves use of the electromagnetic reciprocity principle. Also, lossless media is assumed for all of the formulas presented in this section.

General Description of Reciprocity in Relation to a Half-Space of Ice

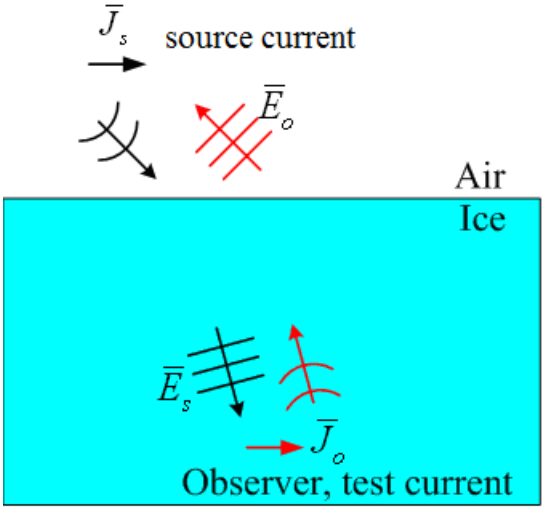

Figure A.1 – Reciprocity

Reciprocity states that the response of a system to a source is unchanged when source and measurer are interchanged [18]. Figure A.1 describes this reciprocal relationship between source and measurer in relation to a half-space of ice. In Figure A.1, a source current $\bar{J}_s$, located near the air/ice interface, radiates an electric field $\bar{E}_s$ which is sensed by an observer (measurer) located far from the air/ice interface.

The observer has a hypothetical test current $\bar{J}_o$ that radiates an electric field $\bar{\bar{E}}_o$, which is planar near the air/ice interface. Since $\bar{J}_s$ is located near the air/ice interface, $\bar{\bar{E}}_s$ is not yet planer near the air/ice interface, and therefore can not be described directly in terms of planar transmission and reflection coefficients. However, the reciprocal relationship between source and observer will be taken advantage of to describe $\bar{\bar{E}}_s$ in terms of the planar $\bar{\bar{E}}_o$ near the air/ice interface.

Using the notation in Figure A.1, reciprocity can be stated mathematically for electric sources via the following relation.

$$\left\langle \bar{\bar{E}}_o, \bar{J}_s \right\rangle = \left\langle \bar{\bar{E}}_s, \bar{J}_o \right\rangle \qquad \textbf{Eq. A.1}$$

The brackets in Equation A.1 indicate the inner product, which expands to the following

$$\iint_S \left(\bar{\bar{E}}_o \cdot \bar{J}_s \right) dS = \iint_S \left(\bar{\bar{E}}_s \cdot \bar{J}_o \right) dS \qquad \textbf{Eq. A.2}$$

Equation A.2 directly relates the source and observer in Figure A.1, and shows that switching the role of source and observer has no effect on the problem solution. The "observer current" $\bar{J}_o$ can be considered to be a hypothetical test current. Although $\bar{J}_o$ is useful in the quasi-far-field formula derivation, it disappears in the final result.

<u>The Four Cases to Consider when Deriving Quasi-Far-Zone Field Formulas</u>

There are four cases to consider when deriving the quasi-far-zone electric fields radiated by surface currents in the presence of a half-space of ice. These four cases, which involve different combinations of field polarization (parallel or

perpendicular) and source and observer location, are outlined in Table A.1. The derivation method for each of the four cases is basically the same. Therefore, only the electric fields for Case 1 will be derived. The formulas for the other 3 cases will be outlined later.

Table A.1 – The Four Reciprocity Cases

Case	E-Field Polarization	Source and Observer Location
1	parallel	Both in Same Medium
2	perpendicular	Both in Same Medium
3	parallel	In Different Mediums
4	perpendicular	In Different Mediums

Derivation of Electric Fields due to Electric Source Currents for Case 1

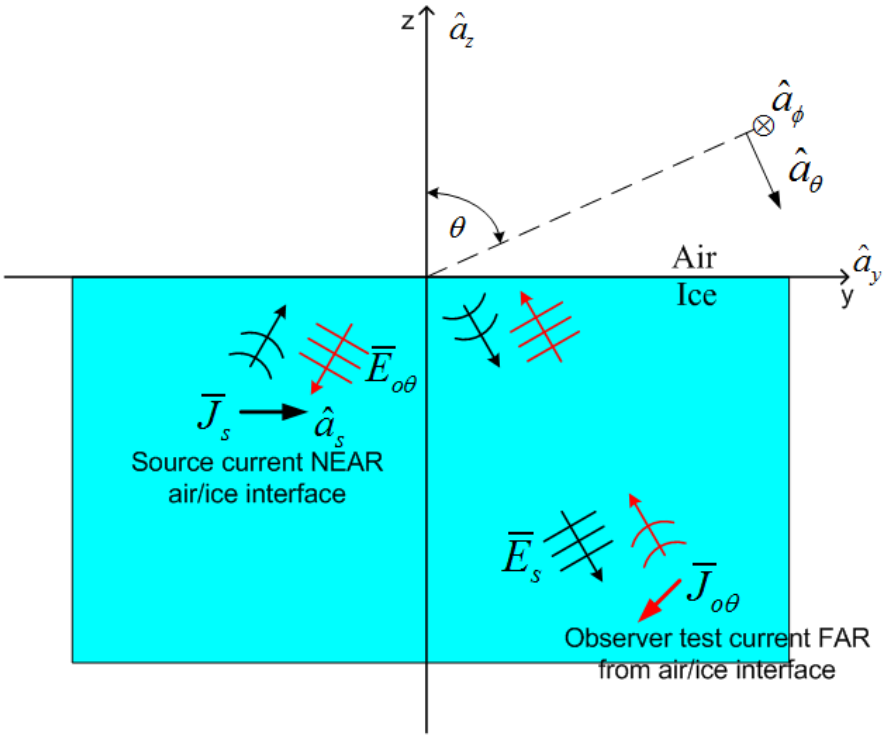

Figure A.2 - Case 1 Reciprocity Derivation

Case 1 involves parallel-polarized electric far-zone fields in which source and observer are located in the same medium (air or ice). Figure A.2 depicts the reciprocal relationship between source and observer for Case 1, and although the source and observer are both shown in ice, they could have also both been shown in air. In Case 1, the far-zone electric field $\overline{E}_s$ is generated by a source current $\overline{J}_s$ which is directed in the $\hat{a}_s$ direction. The $\hat{a}_s$ direction can be either $\hat{a}_x$, $\hat{a}_y$, or $\hat{a}_z$. Because the observer and source are in the same medium, $\overline{E}_s$ will consist of both incident and reflected fields. The observer, located far from the air/ice interface "senses" $\overline{E}_s$ by using a theta directed test current $\overline{J}_{o\theta}$. $\overline{J}_{o\theta}$, which is directed in the $\hat{a}_\theta$ direction, generates an electric field $\overline{E}_{o\theta}$ in the -$\hat{a}_\theta$ direction. Rewriting Equation A.1 to correspond with Figure A.2 yields

$$\left\langle \overline{E}_{o\theta}, \overline{J}_s \right\rangle = \left\langle \overline{E}_s, \overline{J}_{o\theta} \right\rangle \qquad \textbf{Eq. A.3}$$

Expanding Equation A.3 yields

$$\iint_S \left(\overline{E}_{o\theta} \cdot \overline{J}_s \right) dS = \iint_S \left(\overline{E}_s \cdot \overline{J}_{o\theta} \right) dS \qquad \textbf{Eq. A.4}$$

Next, integrating Equation A.4 produces the following result,

$$J_s w_s l_s \hat{a}_s \cdot \overline{E}_{o\theta} = J_{o\theta} w_o l_o \hat{a}_\theta \cdot \overline{E}_s \qquad \textbf{Eq. A.5}$$

where *w* and *l* denote the dimensions of the surface current. Note that

$$\hat{a}_\theta \cdot \overline{E}_s = E_{s\theta} \qquad \textbf{Eq. A.6}$$

indicating that the usage of a theta-directed test current $J_{o\theta}$ extracts the theta component $E_{s\theta}$ of $\bar{E}_s$. Rearranging Equation A.5 in terms of $E_{s\theta}$ yields

$$E_{s\theta} = \frac{J_{sy} w_s l_s \hat{a}_s \cdot \bar{E}_{o\theta}}{J_{o\theta} w_o l_o} \qquad \textbf{Eq. A.7}$$

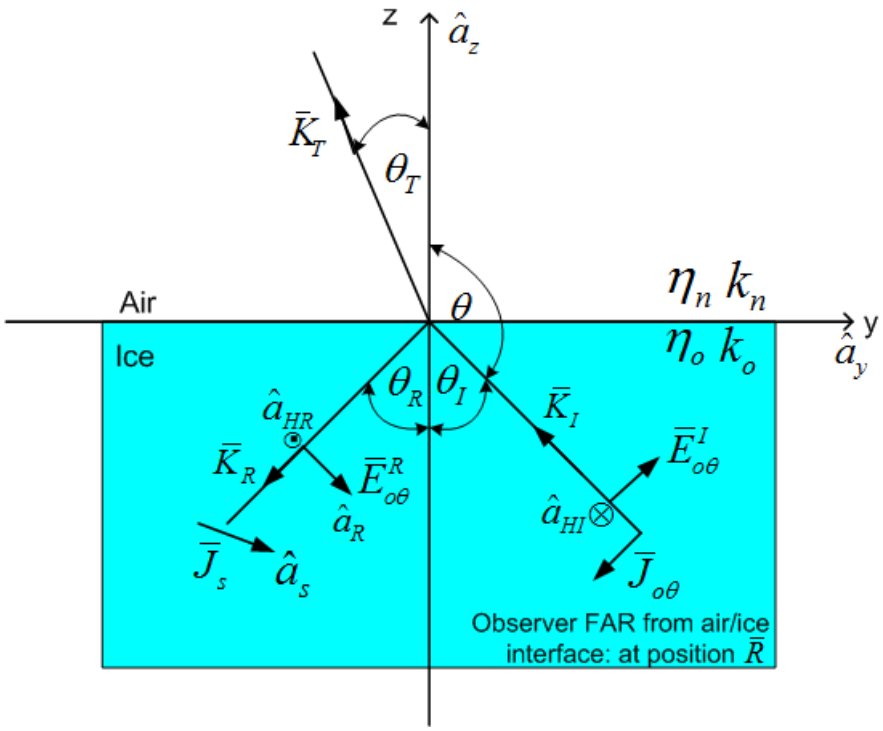

Figure A.3 – Fields Produced by θ-Directed Observer Electric Test Current

The field $\bar{E}_{o\theta}$ can be found using the geometry shown in Figure A.3, which shows the far-zone electric fields produced by $\bar{J}_{o\theta}$, as well as the associated variables. Since both the source and observer are located in the same medium, $\bar{E}_{o\theta}$ can be described by the following

$$\bar{E}_{o\theta} = \bar{E}^{I}_{o\theta} + \bar{E}^{R}_{o\theta} \qquad \textbf{Eq. A.8}$$

where $\bar{E}^{I}_{o\theta}$ and $\bar{E}^{R}_{o\theta}$ are the incident and reflected components of $\bar{E}_{o\theta}$. The incident field $\bar{E}^{I}_{o\theta}$ is a plane wave directed in the $-\hat{a}_{\theta}$ direction described by the following well-known formula [11]

$$\bar{E}^{I}_{o\theta} = \frac{jk_o\eta_o J_{o\theta} w_o l_o}{4\pi} e^{-j(\bar{K}_I \cdot \bar{R})}\left(-\hat{a}_{\theta}\right) \qquad \textbf{Eq. A.9}$$

where k_o and η_o indicate the wavenumber and intrinsic impedance of the medium containing the observer. Also,

$$\bar{K}_I = -k_o \bar{R} \qquad \textbf{Eq. A.10}$$

is the propagation vector of the incident electric field radiated by the observer test current, where the observer position vector is defined by

$$\bar{R} = \sin\theta\cos\phi\hat{a}_x + \sin\theta\sin\phi\hat{a}_y + \cos\theta\hat{a}_z \qquad \textbf{Eq. A.11}$$

and θ and ϕ are the angular positions of the observer. Also, $\bar{K}_I$ is related to the unit incident propagation vector $\hat{k}_I$ via the following

$$\bar{K}_I = k_o\hat{k}_I = k_o\left(k_{Ix}\hat{a}_x + k_{Iy}\hat{a}_y + k_{Iz}\hat{a}_z\right) \qquad \textbf{Eq. A.12}$$

The reflected field $\bar{E}^{R}_{o\theta}$ is also a plane wave and is described by the following well-known formula [11]

$$\bar{E}_{o\theta}^{R} = \Gamma_{\theta} \frac{jk_o \eta_o J_{o\theta} w_o l_o}{4\pi} e^{-j(\bar{K}_R \cdot \bar{R})} (\hat{a}_R) \qquad \textbf{Eq. A.13}$$

where Γ_θ is the parallel-polarized reflection coefficient defined by

$$\Gamma_{\theta} = \frac{\eta_n \cos\theta_T - \eta_o \cos\theta_I}{\eta_n \cos\theta_T + \eta_o \cos\theta_I} \qquad \textbf{Eq. A.14}$$

and η_n is the intrinsic impedance of the medium not containing the observer, which may or may not contain the source. The transmitted and incident angles are θ_T (determined by Snell's Law [11]) and θ_I. Also, $\hat{a}_R$ is the direction of $\bar{E}_{o\theta}^{R}$, as shown in Figure A.3.

Since the direction of propagation, electric field, and magnetic field for a plane wave are always mutually orthogonal, the following can be used to determine the direction of $\bar{E}_{o\theta}^{R}$

$$\hat{a}_R = \hat{a}_{HR} \times \hat{k}_R = -\hat{a}_{\phi} \times \hat{k}_R \qquad \textbf{Eq. A.15}$$

where $\hat{a}_{HR}$ is the direction of the reflected magnetic field, which is in the $-\hat{a}_\phi$ in Figure A.3. Also, $\hat{k}_R$ is the unit propagation vector of the reflected electromagnetic wave and equals the following

$$\hat{k}_R = k_{Ix}\hat{a}_x + k_{Iy}\hat{a}_y - k_{Iz}\hat{a}_z = \frac{\bar{K}_R}{k_o} \qquad \textbf{Eq. A.16}$$

indicating that $\hat{k}_R$ propagates in the same $\hat{a}_x$ and $\hat{a}_y$ direction as $\hat{k}_I$, but in the opposite $\hat{a}_z$ direction.

Equation A.7 can be solved for $E_{s\theta}$, the electric field produced by the source current. By inspection of Equation A.7, since $\bar{E}_{o\theta}$ (defined by Equations A.8, A.9, and A.13) consists of incident and reflected fields, so must $E_{s\theta}$. Therefore, the parallel-polarized electric field produced by $\bar{J}_s$ can be described by

$$E_{s\theta} = E_{s\theta}^{I} + E_{s\theta}^{R} \qquad \textbf{Eq. A.17}$$

The incident field is

$$E_{s\theta}^{I} = \frac{J_s w_s l_s \hat{a}_s \cdot \bar{E}_{o\theta}^{I}}{J_{o\theta} w_o l_o} \qquad \textbf{Eq. A.18}$$

and the reflected field is

$$E_{s\theta}^{R} = \frac{J_s w_s l_s \hat{a}_s \cdot \bar{E}_{o\theta}^{R}}{J_{o\theta} w_o l_o} \qquad \textbf{Eq. A.19}$$

Substituting Equation A.9 into Equation A.18 results in

$$E_{s\theta}^{I} = \frac{jk_o \eta_o J_s w_s l_s}{4\pi} e^{-j(\bar{K}_I \cdot \bar{R})} \hat{a}_s \cdot -\hat{a}_\theta \qquad \textbf{Eq. A.20}$$

and substituting Equation A.13 into Equation A.19 results in

$$E_{s\theta}^{R} = \Gamma_\theta \frac{jk_o \eta_o J_s w_s l_s}{4\pi} e^{-j(\bar{K}_R \cdot \bar{R})} \left(-\hat{a}_\phi \times \hat{k}_R\right) \cdot \hat{a}_s \qquad \textbf{Eq. A.21}$$

Equations A.20 and A.21 are the parallel-polarized electric field formulas due to an electric source current current J_s, with arbitrary direction $\hat{a}_s$, for both source and observer located in the same medium. Notice the elimination of $J_{o\theta}$, w_o, and l_o, which are associated with the observer test current. However, the propagation vectors $\hat{k}_R$, $\hat{k}_I$, $\overline{K}_R$, and $\overline{K}_I$, are with respect to the observer as shown in Figure A.3. Since there is no longer any potential confusion between observer current and source current, it is desirable to change the notation of Equations A.20 and A.21 to the following

$$E_{\theta J}^{I} = \frac{jk_o Jwl\eta_o}{4\pi} e^{-j(\overline{K}_I \cdot \overline{R})} \hat{a}_s \cdot -\hat{a}_\theta \qquad \textbf{Eq. A.22}$$

$$E_{\theta J}^{R} = \Gamma_\theta \frac{jk_o Jwl\eta_o}{4\pi} e^{-j(\overline{K}_R \cdot \overline{R})} \left(-\hat{a}_\phi \times \hat{k}_R\right) \cdot \hat{a}_s \qquad \textbf{Eq. A.23}$$

where $E_{\theta J}^{I}$ and $E_{\theta J}^{R}$ are the parallel-polarized incident and reflected fields due to an electric source current J with arbitrary direction $\hat{a}_s$. The subscript *s* has been removed from *J*, *w*, and *l*, since it is no longer necessary.

Electric Fields due to Electric Source Currents for All Cases

A procedure similar to that used for deriving the Case 1 electric-field formulas can be used to derive the electric-field formulas for the other 3 cases listed in Table A.1. Whether or not the observer and source are located in the same or different mediums affects whether the total electric field consists of both incident and reflected, or only transmitted fields. Also, the electric-field polarization affects the direction of the total electric field. The formulas for the electric fields due to electric current sources for all 4 cases listed in Table A.1 are presented below.

Far-Zone Electric Fields due to Electric Current Sources

Case 1

$$E_{\theta J}^{I} = \frac{jk_o Jwl\eta_o}{4\pi} e^{-j(\bar{K}_I \cdot \bar{R})} \left(-\hat{a}_\theta\right) \cdot \hat{a}_s \qquad \textbf{Eq. A.24}$$

$$E_{\theta J}^{R} = \Gamma_\theta \frac{jk_o Jwl\eta_o}{4\pi} e^{-j(\bar{K}_R \cdot \bar{R})} \left(-\hat{a}_\phi \times \hat{k}_R\right) \cdot \hat{a}_s \qquad \textbf{Eq. A.25}$$

Case 2

$$E_{\theta J}^{T} = T_\theta \frac{jk_o Jwl\eta_o}{4\pi} e^{-j(\bar{K}_T \cdot \bar{R})} \left(\hat{a}_\phi \times \hat{k}_T\right) \cdot \hat{a}_s \qquad \textbf{Eq. A.26}$$

Case 3

$$E_{\phi J}^{I} = \frac{jk_o Jwl\eta_o}{4\pi} e^{-j(\bar{K}_I \cdot \bar{R})} \left(-\hat{a}_\phi\right) \cdot \hat{a}_s \qquad \textbf{Eq. A.27}$$

$$E_{\phi J}^{R} = \Gamma_\phi \frac{jk_o Jwl\eta_o}{4\pi} e^{-j(\bar{K}_R \cdot \bar{R})} \left(-\hat{a}_\phi\right) \cdot \hat{a}_s \qquad \textbf{Eq. A.28}$$

Case 4

$$E_{\phi J}^{T} = T_\phi \frac{jk_o Jwl\eta_o}{4\pi} e^{-j(\bar{K}_T \cdot \bar{R})} \left(-\hat{a}_\phi\right) \cdot \hat{a}_s \qquad \textbf{Eq. A.29}$$

Transmission and Reflection Coefficients for Electric Current Sources

$$T_\theta = \frac{2\eta_n \cos\theta_I}{\eta_n \cos\theta_T + \eta_o \cos\theta_I} \qquad \textbf{Eq. A.30}$$

$$T_\phi = \frac{2\eta_n \cos\theta_I}{\eta_n \cos\theta_I - \eta_o \cos\theta_T} \qquad \textbf{Eq. A.31}$$

$$\Gamma_\theta = \frac{\eta_n \cos\theta_T - \eta_o \cos\theta_I}{\eta_n \cos\theta_T + \eta_o \cos\theta_I} \qquad \textbf{Eq. A.32}$$

$$\Gamma_\phi = \frac{\eta_n \cos\theta_I - \eta_o \cos\theta_T}{\eta_n \cos\theta_I + \eta_o \cos\theta_T} \qquad \textbf{Eq. A.33}$$

Propagation Vectors, Wavenumbers, and Intrinsic Impedances

$$\hat{k}_I = -\bar{R} = k_{Ix}\hat{a}_x + k_{Iy}\hat{a}_y + k_{Iz}\hat{a}_z \qquad \textbf{Eq. A.34}$$

$$\hat{k}_R = k_{Ix}\hat{a}_x + k_{Iy}\hat{a}_y - k_{Iz}\hat{a}_z \qquad \textbf{Eq. A.35}$$

$$\hat{k}_T = k_{Ix}\hat{a}_x + k_{Iy}\hat{a}_y + sign(k_{Iz})\sqrt{k_n^2 - k_{Ix}^2 - k_{Iy}^2} \qquad \textbf{Eq. A.36}$$

$$\bar{R} = \sin\theta\cos\phi\hat{a}_x + \sin\theta\sin\phi\hat{a}_y + \cos\theta\hat{a}_z \qquad \textbf{Eq. A.37}$$

$$\bar{K}_I = k_o\hat{k}_I \qquad \textbf{Eq. A.38}$$

$$\bar{K}_R = k_o\hat{k}_R \qquad \textbf{Eq. A.39}$$

$$\bar{K}_T = k_n\hat{k}_I \qquad \textbf{Eq. A.40}$$

$$k_o = 2\pi f\sqrt{\mu_f\mu_o\varepsilon_f\varepsilon_o} \qquad \textbf{Eq. A.41}$$

$$k_n = 2\pi f\sqrt{\mu_f\mu_n\varepsilon_f\varepsilon_n} \qquad \textbf{Eq. A.42}$$

$$\eta_o = \sqrt{\frac{\mu_f\mu_o}{\varepsilon_f\varepsilon_o}} \qquad \textbf{Eq. A.43}$$

$$\eta_n = \sqrt{\frac{\mu_f\mu_n}{\varepsilon_f\varepsilon_n}} \qquad \textbf{Eq. A.44}$$

Note, in Equations A.41 through A.44, μ_f and ε_f are the free-space magnetic permeability and electric permittivity, respectively. Also, ε_o and ε_n are the dielectric constants of the medium containing and not containing the observer, respectively. The relative magnetic permeabilities μ_o and μ_n are both equal to 1 for since glacial ice and air are both non-magnetic mediums.

Required Formula Adjustments for Incident Angles Exceeding the Critical Angle

For cases involving transmission from a medium with a high dielectric constant to one with a lower dielectric constant (i.e. transmission from ice to air), the possibility for an evanescent wave exists. An evanescent wave is a surface wave that decays exponentially in the $\hat{a}_z$ direction, and is therefore a non-propagating wave. This occurs then the incident angle θ_I is greater than the critical angle θ_c, making the transmission angle θ_T imaginary. The critical angle is determined via the following

$$\theta_c = \sin^{-1}\left(\sqrt{\frac{\varepsilon_n}{\varepsilon_o}}\right) \qquad \textbf{Eq. A.45}$$

For the case of evanescent waves, the following adjustments are required for the transmission and reflection coefficients, and transmission vector [11].

$$T_\theta = \frac{2\eta_n \cos\theta_I}{-jA\eta_n + \eta_o \cos\theta_I} \qquad \textbf{Eq. A.46}$$

$$T_\phi = \frac{2\eta_n \cos\theta_I}{\eta_n \cos\theta_I - jA\eta_o} \qquad \textbf{Eq. A.47}$$

$$\Gamma_\theta = \frac{-j\eta_n A - \eta_o \cos\theta_I}{-j\eta_n A + \eta_o \cos\theta_I} \qquad \textbf{Eq. A.48}$$

$$\Gamma_\theta = \frac{-j\eta_n A - \eta_o \cos\theta_I}{-j\eta_n A + \eta_o \cos\theta_I} \qquad \textbf{Eq. A.49}$$

$$\bar{K}_T = k_{Ix}\hat{a}_x + k_{Iy}\hat{a}_y - jsign(k_{Iz})\sqrt{-k_n^2 + k_{Ix}^2 + k_{Iy}^2}\,\hat{a}_z \qquad \textbf{Eq. A.50}$$

where

$$A = \sqrt{\left(\frac{\varepsilon_o}{\varepsilon_n}\right)\sin^2\theta_I - 1} \qquad \textbf{Eq. A.51}$$

Derivation of Electric Fields due to Magnetic Sources Using Duality

Table A.2 – Duality [18]

(1) For Problems in Which Only Electric Sources Exist

(2) For Problems in Which Only Magnetic Sources Exist

Electric Source (1)	Magnetic Source (2)
E	H
H	- E
J	M
k	k
η	1/η

Duality (see Table A.2) [18] is used to determine the electric far-zone fields due to magnetic source currents. To provide an example of this procedure, $E^I_{\theta M}$ is derived from $E^I_{\phi J}$, which is shown again below

$$E^I_{\phi J} = \frac{jk_o Jwl\eta_o}{4\pi} e^{-j(\bar{K}_I \cdot \bar{R})}\left(-\hat{a}_\phi\right)\cdot\hat{a}_s \qquad \textbf{Eq. A.52}$$

First, using Table A.2, the necessary replacements are made for changing from an electric source current *J* to a magnetic source current *M*, resulting in the following:

$$H^I_{\phi M} = \frac{jk_o Mwl}{4\pi\eta_o} e^{-j(\bar{K}_I \cdot \bar{R})}\left(-\hat{a}_\phi\right)\cdot\hat{a}_s \qquad \textbf{Eq. A.53}$$

where $\hat{a}_s$ is now the direction of *M*. Notice that whereas a ϕ-directed electric current produces a ϕ-directed electric field, a ϕ-directed magnetic current produces a ϕ-directed magnetic field. Now, using the following relation, the electric field associated with $H^I_{\phi M}$ can be determined

$$E = \eta H \qquad \textbf{Eq. A.54}$$

So, the parallel-polarized incident electric field due to a magnetic source current is

$$E^I_{\theta M} = \frac{jk_o Mwl}{4\pi} e^{-j(\bar{K}_I \cdot \bar{R})} \left(-\hat{a}_\phi\right) \cdot \hat{a}_s \qquad \textbf{Eq. A.55}$$

Electric Fields due to Magnetic Source Currents for All Cases

Restating Equation A.55 and using duality to derive all of the parallel and perpendicular electric field components due to magnetic source currents results in the following

Far-Zone Electric Fields due to Magnetic Current Sources

Case 1

$$E^I_{\theta M} = \frac{jk_o Mwl}{4\pi} e^{-j(\bar{K}_I \cdot \bar{R})} \left(-\hat{a}_\phi\right) \cdot \hat{a}_s \qquad \textbf{Eq. A.56}$$

$$E^R_{\theta M} = \hat{\Gamma}_\theta \frac{jk_o Mwl}{4\pi} e^{-j(\bar{K}_R \cdot \bar{R})} \left(-\hat{a}_\phi\right) \cdot \hat{a}_s \qquad \textbf{Eq. A.57}$$

Case 2

$$E^T_{\theta M} = \hat{T}_\theta \frac{jk_o Mwl}{4\pi} e^{-j(\bar{K}_T \cdot \bar{R})} \left(-\hat{a}_\phi\right) \cdot \hat{a}_s \qquad \textbf{Eq. A.58}$$

Case 3

$$E_{\phi M}^{I} = \frac{jk_o Mwl}{4\pi} e^{-j(\bar{K}_I \cdot \bar{R})} \left(\hat{a}_\theta\right) \cdot \hat{a}_s \qquad \textbf{Eq. A.59}$$

$$E_{\phi M}^{R} = \hat{\Gamma}_\phi \frac{jk_o Mwl}{4\pi} e^{-j(\bar{K}_R \cdot \bar{R})} \left(\hat{a}_\phi \times \hat{k}_R\right) \cdot \hat{a}_s \qquad \textbf{Eq. A.60}$$

Case 4

$$E_{\phi M}^{T} = \hat{T}_\phi \frac{jk_o Mwl}{4\pi} e^{-j(\bar{K}_T \cdot \bar{R})} \left(-\hat{a}_\phi \times \hat{k}_T\right) \cdot \hat{a}_s \qquad \textbf{Eq. A.61}$$

Duality also causes a change in the reflection and transmission coefficients for fields produced by magnetic source currents resulting in the following formulas.

Transmission and Reflection Coefficients for Magnetic Current Sources

$$\hat{T}_\theta = \left(\frac{\eta_o}{\eta_n}\right) T_\theta \qquad \textbf{Eq. A.62}$$

$$\hat{T}_\phi = \left(\frac{\eta_o}{\eta_n}\right) T_\phi \qquad \textbf{Eq. A.63}$$

$$\hat{\Gamma}_\theta = -\Gamma_\theta \qquad \textbf{Eq. A.64}$$

$$\hat{\Gamma}_\phi = -\Gamma_\phi \qquad \textbf{Eq. A.65}$$

APPENDIX B: FEM-NFFT-GO Matlab Code Contracts

There are a total of 25 Matlab and VBS functions used to carry out the FEM-NFFT-GO routine. Since this is an enormous amount of code, only the contracts describing the purpose of each function, the functions assumptions, and its inputs and outputs are presented here. The function contracts are presented in alphabetical order.

AnglePos.m

```
%%%%%%%%%%%%%%%%%%%%%%% ---Purpose---%%%%%%%%%%%%%%%%%%%%%%%%%%%%%
%%This function creates an angular position matrix from the point of
%view of the observer
%INPUTS:
% 1. thetaMin,thetaMax; min and max values of theta look
% 2. numTheta; the number of theta values to have
% 3. phi; a specific value of phi
% The inputs are given in units of degrees and converted to radians
%%OUTPUTS:
% 1. lookAngles; a matrix containing both theta and phi values of
%the observer
```

AngleVectors.m

```
%%%%%%%%%%%%%%%%%%%%%%% ---Purpose---%%%%%%%%%%%%%%%%%%%%%%%%%%%%%
% Converts the angular theta and phi directions into x,y,z
%coordinates
%%INPUTS:
% 1. lookAngles; the theta and phi angles of the observer
%%OUTPUTS:
% 1. aHatTheta; the theta directed unit vector converted to x,y,z
% 2. aHatPhi; the phi directed unit vector converted to x,y,z
```

AParameter.m

```
%%%%%%%%%%%%%%%%%%%%%%% ---Purpose---%%%%%%%%%%%%%%%%%%%%%%%%%%%%%
%%This function determines the parameter A, as defined in
%Engineering Electromagnetics (Demarest, p. 500). The A parameter is
%used within transmission and reflection coefficient formulas if the
%critical angle has been exceeded. It is necessary to maintain the
%proper sign and phase of the coefficients.
%INPUTS:
% 1. nA,nB; the indexes of refraction for each medium, where n1 is %
% the incident medium, and n2 is the transmission medium
% 2. thetai; the incident theta angle
%%OUTPUTS:
```

```
% 1. A; the A parameter
```

AutomateFieldCalc.vbs

```
'----------------- AutomateFieldCalc.vbs -------------------------'
' Assumptions:
' 1. a .pts file containing the points for which E and H are desired
is available
' 2. The .pts file contains points in units of meters, as required
by HFSS.
' 3. The geometry must have one box surrouding the entire geometry
' 4. The outputs desired are complex E and H in rectangular
coordinates
' 5. OUTPUTS: E_Field_Results.txt and H_Field_Results.txt
' 6. INPUTS: fieldDataPoints.pts
' NOTE: This code requires use of dirIN, but must be manually typed
into the code
' ---------------------------------------------------------------'
```

AutomatePropertyOutput.vbs

```
'------------------- AutomatePropertyOutput.vbs ------------------'
' Assumptions:
' 1. The boundary surrounding the geometry is a rectangular box
' 2. The boundary box is named exactly "BoundaryBox"
' 3. The geometry must have one box surrouding the entire geometry
' 4. The analysis setup is named exactly "Setup1"
' 5. The geometry is oriented so that the dielectric (ice) half
space is pointing in the negative z direction
' 6. The ice box is assumed to start at the origin and continue in
the negative z direction until the BoundaryBox is reached
' NOTE: This code requires use of dirIN, but must be manually typed
into the code
' ---------------------------------------------------------------'
```

currentDimensions.m

```
%%%%%%%%%%%%%%%%%%%%%%% ---Purpose---%%%%%%%%%%%%%%%%%%%%%%%%%%%%%
%%This function determines the length, width, and direction of a
%surface current, J or M
%%INPUTS:
%  1. faceID; the boundary box face identification
%  2. stepX,stepY,stepZ; the size of the increments in x,y,z
%  dimensions
%%OUTPUTS:
%  1. length,width; the dimensions of the current segment
%  2. curDir1,curDir2; the direction of the current segment, either
%  x,y,z
```

EDifferentMedium_J.m

```
%%%%%%%%%%%%%%%%%%%%%%% ---Purpose---%%%%%%%%%%%%%%%%%%%%%%%%%%%%%%
%%Determines the theta and phi component of the electric field due
%to an electric surface current, Js, for the case of the source and
%observer being in different mediums.
%%INPUTS:
% 1. Js; electric surface current magnitude
% 2. pos; position matrix of Js
% 3. k; the wavenumber
% 4. kT; the transmitted propagation vector
% 5. kHatT; the transmitted unit propagation vector
% 6. length, width; dimensions of Js
% 7. impdanceA; the impedance of the medium
% 8. aHatJ; the direction of Js
% 9. transC; transmission coefficient
% 10. aHatPhi; the phi unit direction
%%OUTPUTS:
% 1. EthetaJ; Etheta due to an electric surface current
% 2. EphiJ; Ephi due to an electric surface current
```

EDifferentMedium_M.m

```
%%%%%%%%%%%%%%%%%%%%%%% ---Purpose---%%%%%%%%%%%%%%%%%%%%%%%%%%%%%%
%%Determines the theta and phi component of the electric field due
%to a magnetic surface current, Ms, for the case of the source and
%observer being in different mediums.
%%INPUTS:
% 1. Ms; the surface current M
% 2. pos; the source position vector relative to the origin
% 3. k; the incident field wavenumber
% 4. KT; transmitted propagation vectors
% 5. kHatT; the transmission unit vector
% 6. length,width; the surface current step size dimensions
% 7. impedanceA; the impedance for the incident mediums
% 8. aHatM; the source unit vector.
% 9. transC; the transmission coefficient
% 10. aHatphi; the phi direction unit vector
%%OUTPUTS:
% 1. EthetaM; Etheta due to a magnetic surface current
% 2. EphiM; Ephi due to a magnetic surface current
```

EfarField.m

```
%%%%%%%%%%%%%%%%%%%%%%% ---Purpose---%%%%%%%%%%%%%%%%%%%%%%%%%%%%%%
%%This function determines the far field theta and phi components of
%E based on both the electric surface current Js and magnetic
%surface currents Ms. Primarily, this function simply determines
%which situation is in effect based on the source/observer
%locations, polarization, and source type
%  %%%%%%%% 4 source/observer possibilities:
%  a. source/observer = top/bottom medium
```

```
%  b. source/observer = bottom/top medium
%  c. source/observer = top/top medium
%  d. source/observer = bottom/bottom medium
%  %%%%%%%% 2 polarization possibilities:
%  a. parallel polarization (theta component)
%  b. perpendicular polarization (phi component)
%  %%%%%%%% 2 source type possibilities:
%  a. electric current
%  b. magnetic current
%%INPUTS:
% 1. Js,Ms; matrix of electric surface currents and magnetic surface
%    currents respectively
% 2. pos; matrix of source position vectors
% 3. k1,k2; wavenumbers for top and bottom media
% 4. KI; incident propagation vectors
% 5. KR; reflected propagation vectors
% 6. KT; transmission propagation vectors
% 7. kHatR; reflected unit vector
% 8. kHatT; transmission unit vector
% 9. length; length of the current segment
% 10. width;  width of the discrete sampled value
% 11. curDir1; direction of the 1st current vector on a face
% 12. curDir2; direction of the 2nd current vector on a face
% 13. impedance1,impedance2; impedances of top and bottom media
% 14. lookAngles; the theta and phi angles of the observer
% 15. reflectC; reflection coefficient array
% 16. transC; transmission coefficient array
% 17; aHatPhi; phi direction unit vector array
% 18; aHatTheta; theta direction unit vector array
%%OUTPUTS:
% 1. Etheta; the parallel polarized E field
% 2. Ephi; the perpendicularly polarized E field
%%Note: postscript 1 on inputs represents medium residing in
%positive z axis (top medium), and postscript 2 represents medium
%residing in negative z axis (bottom medium)
```

EIncMag.m

```
%%%%%%%%%%%%%%%%%%%%%% ---Purpose---%%%%%%%%%%%%%%%%%%%%%%%%%%%%%
%%This function produces the Ei value which is the E field magnitude
%value of the incident field with zero phase. This function can also
%be used to determine Hi. However, this requires dividing the result
%of this function by the impedance, impedance1, which is handled in
%the calling code.
%%INPUTS:
% 1. k1; the incident field wavenumber
% 2. Source; the current segment value (usually denoted J or M)
% 3. length; the length dimension of the discrete current values
% 4. width; the width dimension of the discrete current values
% 5. impedance1; the impedance value of the incident medium
%%OUTPUTS:
% 1. Ei; the E field magnitude
```

Equivalent_Currents.m

```
%%%%%%%%%%%%%%%%%%%%%% ---Purpose---%%%%%%%%%%%%%%%%%%%%%%%%%%%%%%
%Equivalent_Current samples near E and H fields from HFSS and then
%converts those fields to equivalent currents.
%%INPUTS:
% 1. dirIn: the input directory of the raw data files
% 2. ptsInput: the near field sampling interval
% 3. sDecXY: the sampling box decrement factor in the XY dimensions
% 4. sDecZ_Top: the sampling box decrment factor in the upper z
% plane
% 5. sDecZ_Bot: the sampling box decrment factor in the lower z
% plane
%%OUTPUTS:
% 1. Frequncy
% 2. stepX,stepY,stepZ: the sampling size dimension
% 3. Js"": the electric current matrix for each face
% 4. Ms"": the magnetic current matrix for each face
% 5. pos"": the current position matrix for each face
%%NOTE: The faces are divided into left, right, top, bottom, front,
%and back
```

ESameMedium_J.m

```
%%%%%%%%%%%%%%%%%%%%%% ---Purpose---%%%%%%%%%%%%%%%%%%%%%%%%%%%%%%
%%Determines the theta and phi component of the electric field due
%to an electric surface current, Js, for the case of the source and
%observer being in the same medium.
%%INPUTS:
% 1. Js; the surface current J
% 2. pos; the source position vector relative to the origin
% 3. k; the incident field wavenumber
% 4. KI; the incident field vector
% 5. KR; the reflected field vector
% 6. kHatR; the reflection unit vector
% 7. length,width; the surface current step size dimensions
% 8. impedanceA; the impedance for the incident mediums
% 9. aHatJ; the source unit vector.
% 10. reflectC; the reflection coefficient
% 11. aHatphi; the phi direction unit vector
% 12. aHatTheta; the theta direction unit vector
%%OUTPUTS:
% 1. EthetaJ; Etheta due to an electric surface current
% 2. EphiJ; Ephi due to an electric surface current
```

ESameMedium_M.m

```
%%%%%%%%%%%%%%%%%%%%%% ---Purpose---%%%%%%%%%%%%%%%%%%%%%%%%%%%%%%
%%Determines the theta and phi component of the electric field due
%to a magnetic surface current, Ms, for the case of the source and
%observer being in the same medium.
%%INPUTS:
```

```
% 1. Ms; the surface current M
% 2. pos; the source position vector relative to the origin
% 3. k; the incident field wavenumber
% 4. KI; the incident field vector
% 5. KR; the reflected field vector
% 6. kHatR; the reflection unit vector
% 7. length,width; the surface current step size dimensions
% 8. impedanceA; the impedance for the incident mediums
% 9. aHatM; the source unit vector.
% 10. reflectC; the reflection coefficient
% 11. aHatphi; the phi direction unit vector
% 12. aHatTheta; the theta direction unit vector
%%OUTPUTS:
% 1. EthetaJ; Etheta due to a magnetic surface current
% 2. EphiJ; Ephi due to a magnetic surface current
```

GainFactor.m

```
%%%%%%%%%%%%%%%%%%%%%% ---Purpose---%%%%%%%%%%%%%%%%%%%%%%%%%%%%
%Determines the gain factor improvement in the E fields due to the
%focusing effect arising from increasing dielectric constant with
%increasing depthin glacial ice.
%%INPUTS:
% 1. EthetaIN; the total theta directed E field, calculated from
%    previous code
% 2. EphiIN; the total phi directed E field, calculated from
%    previous code
% 3. lookAngles; the angles associated with EthetaTotal and %
%    EphiTotal
% 4. location; 1 = Antarctia, 2 = Greenland
% 5. z; the depth vector
%%OUTPUTS:
% 1. GthetaAD; Etheta as a function of aidaPrime (rows)
%    and depth (columns) - in magnitude gain
% 2. GphiAD; Ephi as a function of aidaPrime (rows) and
%    depth (columns) - in magnitude gain
% 3. g0; The incident angles at the surface directed towards the
%    ice, ranging only from 0 to 90 degrees (double sided).
% 4. g02; The incident angles at the surface directed towards the
%    ice, ranging only from 90 to 270 degrees.
% 5. aidaPrime; the effective look angle at each depth -- 0 degrees
%    at nadir (goes from 0 to 90 and 0 to -90 degrees)
% 6. Gf; The gain factor improvement matrix
```

Generate_PTS_File.m

```
%%%%%%%%%%%%%%%%%%%%%% ---Purpose---%%%%%%%%%%%%%%%%%%%%%%%%%%%%
%creates a .pts file for each of the six boundary box faces given
%x,y,z minimum and maxium values
%%INPUTS:
% 1. xMin,yMin,zMin; the minimum boundary box dimensions
% 2. xMax,yMax,zMax; the maximum boundary box dimensions
```

```
% 3. Frequency; the frequency of antenna operation
% 4. ptsInput; the number of sample points taken per wavelength
% 5. sDecXY; the sample box decrement factor in X and Y dimensions
% 6. sDecZ_TOP; the sample box decrement factor in positive Z
% 7. sDecZ_Bot; the sampel box decrement facotr in negative Z
% 8. dirIn; the directory containing the data files
%INPUT ASSUMPTIONS: Assume that the boundary box is rectangular; the
%input dimensions are in units of meters; the frequency is in units
%of Hz; the ptsInput is in units of points/wavelength
%NOTE: HFSS requires that the .pts file be in units of meters.
%OUTPUTS: outputs 6 .pts files, one for each boundary box face;
% 1. stepX,stepY,stepZ; the x,y,z sample increment values.
%comments assume positive z pointing upward, positive y pointing to
%the right, and poitive x pointing out of the screeen
```

KVectors.m

```
%%%%%%%%%%%%%%%%%%%%%% ---Purpose---%%%%%%%%%%%%%%%%%%%%%%%%%%%%%%
%%This function produces the K vectors. The K vectors describe the
%propagation of incident, reflected, or transmitted waves
%%INPUTS:
% 1. lookAngles; the look angles, theta and phi of the observer
% 2. k1,k2; the wavenumbers of the top and bottom media
%%OUTPUTS:
% 1. KI; the incident propagation vectors for media 1 and 2
% 2. KR; the reflected propagation vectors for media 1 and 2
% 3. KT; the transmitted propagation vectors for media 1 and 2
```

Master.m

```
%%%%%%%%%%%%%%%%%%%%%% ---Purpose---%%%%%%%%%%%%%%%%%%%%%%%%%%%%%%
%Master_Output runs either the FEM-NFFT by itself or in combination
%with the GO algorithm. This code is divided into three section with
%necessary comments listed below
% 1. INPUTS TO SPECIFY
% 2. The FEM-NFFT Procedure
% 3. The GO Procedure
```

NFFT.m

```
%%%%%%%%%%%%%%%%%%%%%% ---Purpose---%%%%%%%%%%%%%%%%%%%%%%%%%%%%%%
%NFFT performs the near to far field transformations
%%INPUTS:
% 1. thetaMin: the minimum desired value of the angle theta
% 2. thetaMax: the maximum desired value of the angle theta
% 3. numTheta: the number of theta values desired for angular
%    resolution
% 4. phi: the value of phi desired
% 5. e1,e2: the relative permittivity of the top and bottom mediums
% 6. u1,u2: the relative permeability of the top and bottom mediums
% 7. Frequncy
```

```
% 8. stepX,stepY,stepZ: the sampling size dimension
% 9. Js"": the electric current matrix for each face
% 10.Ms"": the magnetic current matrix for each face
% 11.pos"": the current position matrix for each face
%%OUTPUTS:
% 1. EthetaTotal: the total complex E-field in theta
% 2. EphiTotal: the total complex E-field in phi
% 3. lookAngles: the matrix in radians containing theta and phi
%    values
% 4. impedance1: the intrinsic impedance of the top medium
% 5. impedance2: the intrinsic impedance of the bottom medium
```

ObtainHFSS_Properties.m

```
%%%%%%%%%%%%%%%%%%%%%% ---Purpose---%%%%%%%%%%%%%%%%%%%%%%%%%%%%%
%Obtains outer boundary data from HFSS_DataOut.txt
%Determines box dimensions and frequency and convert dimensions to
%meters
%%%%% -- Assumptions -- %%%%%%
% 1. Assumes that the boundary is a rectangular box
% 2. Assumes HFSS units of nm,um,mm,meter,cm,km,ft,in,mil,uin
% 3. Code converts all units to meters
%%INPUT ASSUMTIONS: The input file contains text of the following
%form:
%   XSize   10mm
%   YSize   10mm
%   ZSize   2.5mm
%   Position    -5 ,-5 ,0    %position can contain units
%   Frequency   50000000000
%%INPUT:
% 1. HFSSInputFile; a file containing the data shown above
%%OUTPUT:
% 1. xMin,yMin,zMin; the minimum dimensions of boundary box
% 2. xMax,yMax,zMax; the maximum dimensions of boundary box
% 3. Frequency; the frequency of the HFSS simulation in Hz
```

reflectCoeff.m

```
%%%%%%%%%%%%%%%%%%%%%% ---Purpose---%%%%%%%%%%%%%%%%%%%%%%%%%%%%%
%%This function produces the reflection coefficient, which is either
%parallel or perpendicular depending on the polarization
%INPUTS:
% 1. lookAngles; matrix of theta and phi of the observer
% 2. thetaI; the incident angle
% 3. thetaT; the transmission angle
% 4. impedance1; the impedance value of the incident medium
% 5. impedance2; the impedance value of the transmission medium
% 6. n1,n2; the indexes of refraction for each medium
%%OUTPUTS:
% 1. reflectC; the reflection coefficient
```

SourceVector.m

```
%%%%%%%%%%%%%%%%%%%%%%% ---Purpose---%%%%%%%%%%%%%%%%%%%%%%%%%%%%%%
% Converts the curDir1 and curDir2 direction indexes to actual
% vector direction
%%NOTES: curDir'' = 1 indicates x directed current
%        curDir'' = 2 indicates y directed current
%        curDir'' = 3 indicates z directed current
%%INPUTS:
% 1. curDir1, curDir2; the direction of each type of current on the
%    data sample face
%%OUTPUTS:
% 1. aHatS1, aHatS2; the unit vector of each type of current on the
%    data sample face
```

SurfCurrents.m

```
%%%%%%%%%%%%%%%%%%%%%%% ---Purpose---%%%%%%%%%%%%%%%%%%%%%%%%%%%%%%
%%This function takes in the E and H field data from a face of the
%boundary box, and computes the electric and magnetic surface
%currents Js and Ms.
%%INPUTS:
% 1. Efilename; the data file containing the near-zone electric
%    field data for a surface
% 2. Hfilename; the data file containing the near-zone electric
%field data for a surface
% 3. faceID; a value identifying which face of the sampling box has
%    been input
%%OUTPUTS:
% 1. Js; the electric surface currents on the face
% 2. Ms; the magnetic surface currents on the face
% 3. pos; the position of each surface current on the face
```

ThetaAngles.m

```
%%%%%%%%%%%%%%%%%%%%%%% ---Purpose---%%%%%%%%%%%%%%%%%%%%%%%%%%%%%%
%%This function produces a matrix of the incident and transmission
%angles theta
%%INPUTS:
% 1. lookAngles; matrix of theta and phi of the observer
% 2. nA,nB; the refractive indexes of the incident and transmission
%    media.
%%OUTPUTS:
% 1. thetaI; the incident angle
% 2. thetaT; the transmitted angle
```

transCoeff.m

```
%%%%%%%%%%%%%%%%%%%%%%% ---Purpose---%%%%%%%%%%%%%%%%%%%%%%%%%%%%%%
%%This function produces the transmission coefficient, which is
%either parallel or perpendicular depending on the polarization
%%INPUTS:
% 1. lookAngles; matrix of theta and phi of the observer
% 2. thetaI; the incident angle
% 3. thetaT; the transmission angle
% 4. impedance1; the impedance value of the incident medium
% 5. impedance2; the impedance value of the transmission medium
% 6. n1,n2; the indexes of refraction for each medium
%%OUTPUTS:
% 1. transC; the reflection coefficient
```

WaveNumber.m

```
%%%%%%%%%%%%%%%%%%%%%%% ---Purpose---%%%%%%%%%%%%%%%%%%%%%%%%%%%%%%
%%This function produces the wavenumbers, impedances, and index of
%refraction from each medium in the half-space
%%INPUTS:
% 1. Frequency; the operating frequency
% 2. e1,e2; the dielectric constant of top and bottom media
% 3. u1,u2; the relative permeavility of the top and bottom media
%%OUTPUTS:
% 1. k1,k2; wavenumbers of top and bottom media
% 2. impedance1,impedance2; impedances of top and bottom medium
% 3. n1,n2; indexes of refraction of top and bottom media
```

APPENDIX C: IceTemp.m Matlab Code

This section contains the temperature profile extraction code, called *IceTemp.m*, which is a modified version of original code presented by Lie, Xie, and Dobbs in [27]. This code was used to perform the temperature profile extraction simulations shown in Chapter 5.

```
%%%%%%%%%%%%%%%%%%%%%%%%%%%%%%%%%%%%%%%%%%%%%%%%%%%%%%%%%%%%%%%%%%%%%%%%%%%%
%PART 1:  obtain Temperature profiles from the Excel Spreadsheet
%Data
% 1.) Read the temperature vs. depth profile for pure ice
% 2.) Enter in constants
% 3.) Produce layer depth matrix
% 4.) Load the Antenna Gain Data
% 2.) Calculate the real and imaginary parts of the permittivity
% 3.) Calculate the wavenumber, loss tangent, and attenuation
% 4.) Calculate the Total Attenuation

%%%%%%%%%%%%%%%% Read in the Temperature Profiles %%%%%%%%%%%%%%%%%%%
% GRIP Temperature Profile
T1 = xlsread ('Ice_temp_profile', 'Hypothetical profiles',
'B4:B304');
% Hypothetical 1 Profile
T2 = xlsread ('Ice_temp_profile', 'Hypothetical profiles',
'C4:C304');
% Hypothetical 2 Profile
T3 = xlsread ('Ice_temp_profile', 'Hypothetical profiles',
'D4:D304');
% read the depth profile
d = xlsread ('Ice_temp_profile', 'Hypothetical profiles',
'A4:A304');
% plot temperature profiles in terms of depth
figure (1);
plot(T1, d, 'r');hold on
plot(T2, d, 'b');hold on
plot(T3, d, 'm');hold off
grid;
h = gca;
set (h, 'YDir', 'reverse');
legend ('GRIP', 'Hypothetical_1', 'Hypothetical_2',
'Location','NorthEast');
title ('Ice Temperature Profiles');
xlabel ('T (C)');
ylabel ('Depth (m)');
%%%%%%%%%%%%%%%%%%%%%%%%%%%%%%%%%%%%%%%%%%%%%%%%%%%%%%%%%%%%%%%%%%%%%%%%%%%%

%%%%%%%%%%%%%%%%%%%%%%%% Constants %%%%%%%%%%%%%%%%%%%%%%%%%%%%%%
%depth of each layer (depth-resolution)
```

```
layerDepth = 100;                   %meters
% number of layers to consider
numLayers = 3000/layerDepth;
%bistatic radar separation for Configuration 1
separation = 50;                    %meters
halfSep = separation/2;             %meters
%Configuration 2 parameters are determined from the calculated
critical
%angle
%radar system bandwidth
B = 180e6;                          %Hz
%the transmitted power
Pt = 800;                           %watts
%transmitted pulse width
pulseWidth = 10e-6;                 %seconds
%center frequency of the chirp range
f = 210e6;              %Hz
w = 2*pi*f;             %rad/s
%the speed of light
c = 3e8;
%define free space permeability and permittivity
E0 = 8.854*10^-12;          %F/m
u0 = 4*pi*10^-7;            %H/m

%%%%%%%%%%%%%% Produce the layer depth matrix %%%%%%%%%%%%%%%%%%%%%
%units are in meters
for m=1:numLayers
    zDepth(m) = layerDepth*m;
end

%%%%%%%%%%%%%%%%%%%%%%%%% Load the Gain Data %%%%%%%%%%%%%%%%%%%%%%%%
Eplane=load('VivaldiEPlane.mat');
zE = Eplane.zDepth;
Gtheta = Eplane.GthetaAD;
% Gphi = Eplane.GphiAD;
Angles = Eplane.aidaPrime*180/pi;
s = size(Angles);
numAngle = s(1);
midWay = round(numAngle/2);
%only keep one half of the Gain and angle data, since it is
symmetrical.
GthetaHalf = Gtheta(1:midWay,:);
angleHalf = angles2(1:midWay,:);
%results from FEM-NFFT-GO
GainFNG = GthetaHalf;
angleFNG = angleHalf;

%%%%%%%%%%%%%%%%%%%% Calculate the Permittivity %%%%%%%%%%%%%%%%%%%%
% calculate the real part of the relative permittivity of pure ice
%using the constant Er method
Ep1 = 3.1884 + 0.00091.*T1;
Ep2 = 3.1884 + 0.00091.*T2;
Ep3 = 3.1884 + 0.00091.*T3;
```

```
% calculate the imaginary part of the relative permittivity
EDp1 = 10.^(-2.02+0.025.*T1)/(10*f/1e9);
EDp2 = 10.^(-2.02+0.025.*T2)/(10*f/1e9);
EDp3 = 10.^(-2.02+0.025.*T3)/(10*f/1e9);

%%%%%%%%%%% Calculate Wavenumber, Loss Tangent, Attenuation %%%%%%%%
%Loss Tangents
lossTan1 = EDp1./Ep1;
lossTan2 = EDp2./Ep2;
lossTan3 = EDp3./Ep3;
%Wave Number of the ice
k1 = w.*sqrt(Ep1)/c;
k2 = w.*sqrt(Ep2)/c;
k3 = w.*sqrt(Ep3)/c;
%Attenuation Profile (exact formulas)
alpha1 = w.*sqrt(u0.*E0*Ep1./2.*(sqrt(1+(lossTan1).^2)-1));
alpha2 = w.*sqrt(u0.*E0*Ep2./2.*(sqrt(1+(lossTan2).^2)-1));
alpha3 = w.*sqrt(u0.*E0*Ep3./2.*(sqrt(1+(lossTan3).^2)-1));

%%%%%%%%%%%%%% Calculate the Overall Attenuation value %%%%%%%%%%%%
format short, alphaAvg1 = mean(alpha1);
format short, alphaAvg2 = mean(alpha2);
format short, alphaAvg3 = mean(alpha3);
% two way attenuation in dB if the depth is 3000 m
two_way_att_dB_1 = alphaAvg1*8.686*3000*2;
two_way_att_dB_2 = alphaAvg2*8.686*3000*2;
two_way_att_dB_3 = alphaAvg3*8.686*3000*2;



%%%%%%%%%%%%%%%%%%%%%%%%%%%%%%%%%%%%%%%%%%%%%%%%%%%%%%%%%%%%%%%%%%%%%%%
%%%%%%%%%%%%%%%%%%%%%%%%%%%%%%%%%%%%%%%%%%%%%%%%%%%%%%%%%%%%%%%%%%%%%%%
% Part 2: Power Received Simulation
% Configuration 1 -- Use a 50 meter separation for all the layers --
% Predict the received radar power from the derived attenuation
% profiles above
% 1.) Determine the Incident Angle from the radar to each layer
% 2.) Determine the Loss and Range for each layer
% 3.) Calculate the real part of the Relative Permittivity from top
% to bottom and from bottom to top (only useful for calculating non-
% specular reflectivity)
% 4.) Calculate the specular reflectivity
% 5.) Calculate the veloctiy and wavelength
% 6.) Extract Antenna Gain values for given angle and depth
% 7.) Calculate the received power estimated from the loss, which
% was estimated from the attenuation, which was estimated from the
% known temperature profiles.

%%%%%%%%%%%%%%% Incident Angle to each layer (degrees) %%%%%%%%%%%%%%
for m = 1:numLayers
     incidentAngle1_1(m) = atand(halfSep/(zDepth(m)));
     incidentAngle2_1(m) = atand(halfSep/(zDepth(m)));
     incidentAngle3_1(m) = atand(halfSep/(zDepth(m)));
end
```

```
%%%%%%%%%%%%%%%%%%%% Loss and Range for each layer %%%%%%%%%%%%%%%%%
for m = 1:numLayers;
    if numLayers < 31
        R1_1(m) = zDepth(m)/cosd(incidentAngle1_1(m));
        L1_1(m) =
exp(2*secd(incidentAngle1_1(m))*10*sum(alpha1(1:10*m)));
        R2_1(m) = zDepth(m)/cosd(incidentAngle2_1(m));
        L2_1(m) =
exp(2*secd(incidentAngle2_1(m))*10*sum(alpha2(1:10*m)));
        R3_1(m) = zDepth(m)/cosd(incidentAngle3_1(m));
        L3_1(m) =
exp(2*secd(incidentAngle3_1(m))*10*sum(alpha3(1:10*m)));
    else
        R_1_1(m) =(100*m+1.1)/cosd(incidentAngle1_1(m));
        L_1_1(m) =
exp(2*secd(incidentAngle1_1(m))*1*sum(alpha1(1:m)));
        R_2_1(m) = (100*m+1.1)/cosd(incidentAngle2_1(m));
        L_2_1(m) =
exp(2*secd(incidentAngle2_1(m))*1*sum(alpha2(1:m)));
        R_3_1(m) = (100*m+1.1)/cosd(incidentAngle3_1(m));
        L_3_1(m) =
exp(2*secd(incidentAngle3_1(m))*1*sum(alpha3(1:m)));
    end
end

%%%%%%%%%%% Average Value of the Real Part Permittivity %%%%%%%
% from the top to bottom
for m = 1:numLayers
      Ep1_mt(m) = mean(Ep1(1:10*m));
      Ep2_mt(m) = mean(Ep2(1:10*m));
      Ep3_mt(m) = mean(Ep3(1:10*m));
end
% from bottom to top
for m = 1:numLayers-1;
    Ep1_mb(m) = mean(Ep1(10*m+1:301));
    Ep2_mb(m) = mean(Ep2(10*m+1:301));
    Ep3_mb(m) = mean(Ep3(10*m+1:301));
end
Ep1_mb(numLayers) = 2.7; % for frozon bedrock, from David's thesis
Ep2_mb(numLayers) = 2.7;
Ep3_mb(numLayers) = 2.7;

%%%%%%%%%%%%%%%%%%%% The Ice Reflectivity %%%%%%%%%%%%%%%%%%%%%%%%%
%%%%%%%% Assuming Specular Reflectivity
% assume it equals -80 dB at all layers except for the bedrock
interface!!!
gammaSP = -80;                          %dB
gammaSPMag = 10^(gammaSP/10);           %unitles
gammaBedrock = 0.00167;
for m = 1:numLayers-1;
    gamma1_1(m) = gammaSPMag;
    gamma2_1(m) = gamma1_1(m);
```

```
    gamma3_1(m) = gamma2_1(m);
end
gamma1_1(numLayers) = gammaBedrock;
gamma2_1(numLayers) = gammaBedrock;
gamma3_1(numLayers) = gammaBedrock;

%%%%%%%%%%%%%%%% Velocity and Lambda %%%%%%%%%%%%%%%%%%%%%%%%%%%%%
%calculate the velocity for each temp profile
vp1 = c/sqrt(Ep1_mb(1));                                %m/s
vp2 = c/sqrt(Ep2_mb(1));                                %m/s
vp3 = c/sqrt(Ep3_mb(1));                                %m/s
%calculate the wavelength in ice for each temp profile
lambda1 = vp1/f;                                        %m
lambda2 = vp2/f;                                        %m
lambda3 = vp3/f;                                        %m

%%%%%%%%%%%%%%%%%%%% Antenna Gain %%%%%%%%%%%%%%%%%%%%%%%%%%%%%%%%
%determine the gain at each incident angle and each depth
%%%% Assuming constant gain, not using Gain from FEM-NFFT-GO %%%%%%%
% 3 dB gain assumed
% for m=1:numLayers
%     for n=1:numLayers
%          GainMag(m,n)=10^0.3;
%     end
% end
%%%% Extracting Relevant Gain Values form FEM-NFFT-GO Code %%%%%%
for m=1:numLayers
    %the incident angle at z
    angleInc = incidentAngle1_1(m);
    %the difference between the incident angle at z and angles in
gain
    %pattern at z
    diFF = abs(angleFNG(:,m)-angleInc);
    %the index where the two angles agree most
    index = find(diFF == min(diFF));
    GainMag(m) = GainFNG(index,m);                      %dB
end

%%%%%%%%%%%%%%%%%%%%%%% Received Power %%%%%%%%%%%%%%%%%%%%%%%%%%%%
%units are in Watts
for m=1:numLayers
    Pr1_1(m) = Pt *
GainMag(m)^2*lambda1^2*gamma1_1(m)/((8*pi*R1_1(m))^2*L1_1(m));
    Pr2_1(m) = Pt *
GainMag(m)^2*lambda2^2*gamma2_1(m)/((8*pi*R2_1(m))^2*L2_1(m));
    Pr3_1(m) = Pt *
GainMag(m)^2*lambda3^2*gamma3_1(m)/((8*pi*R3_1(m))^2*L3_1(m));
end
%%%%%%%%%%%%%%%%%%%%%%%%%%%%%%%%%%%%%%%%%%%%%%%%%%%%%%%%%%%%%%%%%%%

%%%%%%%%%%%%%%%%%%%%%%%%%%%%%%%%%%%%%%%%%%%%%%%%%%%%%%%%%%%%%%%%%%%
% Part 2: Power Received Simulation
% Configuration 2 -- Use a separation defined by the incident angle
```

```
% that is half of the critical angle
% Predict the received radar power from the derived attenuation
% profiles above
% 1.) Determine the Incident Angle from the radar to each layer
% 2.) Determine the Loss and Range for each layer
% 3.) Calculate the real part of the Relative Permittivity from top
% to bottom and from bottom to top
% 4.) Calculate the specular reflectivity
% 5.) Calculate the received power estimated from the loss, which
% was estimated from the attenuation, which was estimated from the
% known temperature profiles.

%%%%%%%%%%%%%%%%%%%%%%% Critical Angle %%%%%%%%%%%%%%%%%%%%%%%%%%%%
%the critical angle only exists for propagation from ice to air
%the index of refraction for air
nAir = 1;
%ice dielectric constant for pursposes of calculating critical angle
Eice = 3.2;
%fixed critical angle and halfSepMax
cTheta = asind(nAir/sqrt(Eice));
halfSepMax = zDepth.*tand(cTheta);
%factor for determing the antenna separation to use based on the
%maximum possible antenna separation
factor = 2;
halfSep1 = halfSepMax./factor;
halfSep2 = halfSepMax./factor;
halfSep3 = halfSepMax./factor;

%%%%%%%%%%%%%%%% Incident Angle, Range, and Depth %%%%%%%%%%%%%%%%%%
for m=1:numLayers
   incidentAngle1_2(m) = atand(halfSep1(m)/(zDepth(m)));
   incidentAngle2_2(m) = atand(halfSep2(m)/(zDepth(m)));
   incidentAngle3_2(m) = atand(halfSep3(m)/(zDepth(m)));
   R1_2(m) = zDepth(m)/cosd(incidentAngle1_2(m));
   R2_2(m) = zDepth(m)/cosd(incidentAngle2_2(m));
   R3_2(m) = zDepth(m)/cosd(incidentAngle3_2(m));
   if numLayers < 31
        L1_2(m) =
exp(2*secd(incidentAngle1_2(m))*10*sum(alpha1(1:10*m)));
        L2_2(m) =
exp(2*secd(incidentAngle2_2(m))*10*sum(alpha2(1:10*m)));
        L3_2(m) =
exp(2*secd(incidentAngle3_2(m))*10*sum(alpha3(1:10*m)));
   else
       L1_2(m) =
exp(2*secd(incidentAngle1_2(m))*1*sum(alpha1(1:1*m)));
       L2_2(m) =
exp(2*secd(incidentAngle2_2(m))*1*sum(alpha2(1:1*m)));
       L3_2(m) =
exp(2*secd(incidentAngle3_2(m))*1*sum(alpha3(1:1*m)));
   end
end
```

```
%%%%%%%%%%%%%%%%%%%% The Ice Reflectivity %%%%%%%%%%%%%%%%%%%%%%%%
% for specular case, use same as Part 1
gamma1_2 = gamma1_1;
gamma2_2 = gamma2_1;
gamma3_2 = gamma3_1;

%%%%%%%%%%%%%%%%%%%% Antenna Gain %%%%%%%%%%%%%%%%%%%%%%%%%%%%
%determine the gain at each incident angle and each depth
%%%% Assuming constant gain, not using Gain from FEM-NFFT-GO %%%%%%%
%GainMag2 = GainMag;
%%%% Extracting Relevant Gain Values form FEM-NFFT-GO Code %%%%%%
for m=1:numLayers
    %the incident angle at z
    angleInc = incidentAngle1_2(m);
    %the difference between the incident angle at z and angles in
    %gain pattern at z
    diFF = abs(angleFNG(:,m)-angleInc);
    %the index where the two angles agree most
    index = find(diFF == min(diFF));
    GainMag2(m) = GainFNG(index,m);                          %dB
end

%%%%%%%%%%%%%%%%%%%% Received Power %%%%%%%%%%%%%%%%%%%%%%%%%%%%
%These are all basically for a constant incident angle
for m=1:numLayers
    Pr1_2(m) =
Pt*GainMag2(m)^2*lambda1^2*gamma1_2(m)/((8*pi*R1_2(m))^2*L1_2(m));
    Pr2_2(m) =
Pt*GainMag2(m)^2*lambda2^2*gamma2_2(m)/((8*pi*R2_2(m))^2*L2_2(m));
    Pr3_2(m) =
Pt*GainMag2(m)^2*lambda3^2*gamma3_2(m)/((8*pi*R3_2(m))^2*L3_2(m));
end
%%%%%%%%%%%%%%%%%%%%%%%%%%%%%%%%%%%%%%%%%%%%%%%%%%%%%%%%%%%%%%%%%%%

%%%%%%%%%%%%%%%%%%%%%%%%%%%%%%%%%%%%%%%%%%%%%%%%%%%%%%%%%%%%%%%%%%%
% Part 3: Derive Attenuation from Power      %%%%%%%%%%%%%%%%%%%%%%
% 1.) Estimate the Antenna Gain for Temperature Extraction
% 2.) Calculate total attenuation from z=0 to each depth
% 3.) Determine the attenuation at each depth
% 4.) Extract Temperature from Attenuation

%%%%%%%%%%%%%%%%%%% Estimated Antenna Gain %%%%%%%%%%%%%%%%%%%%%%%%
% Normal: Assume estimated gain is the same as that used for Pr
% simulations
GainMag_E = GainMag;
GainMag2_E = GainMag2;
% Assume a uniform dB error in the gain estimation
%error_dB = 30.0;
%GainMag_EdB = 10*log10(GainMag) - error_dB;
%GainMag2_Edb = 10*log10(GainMag2) - error_dB;
%GainMag_E = 10.^(GainMag_EdB/10);
%GainMag2_E = 10.^(GainMag2_Edb/10);
```

```
%%%%%%%% Calculate total attenuation from z=0 to each depth %%%%%%%%
for m=1:numLayers
   alphaAccum1(m) =
log((GainMag_E(m)^2*Pr1_2(m)*cosd(incidentAngle1_1(m))^2)/(GainMag2_
E(m)^2*Pr1_1(m)*cosd(incidentAngle1_2(m))^2))/(2*(secd(incidentAngle
1_1(m))-secd(incidentAngle1_2(m))));
   alphaAccum2(m) =
log((GainMag_E(m)^2*Pr2_2(m)*cosd(incidentAngle2_1(m))^2)/(GainMag2_
E(m)^2*Pr2_1(m)*cosd(incidentAngle2_2(m))^2))/(2*(secd(incidentAngle
2_1(m))-secd(incidentAngle2_2(m))));
   alphaAccum3(m) =
log((GainMag_E(m)^2*Pr3_2(m)*cosd(incidentAngle3_1(m))^2)/(GainMag2_
E(m)^2*Pr3_1(m)*cosd(incidentAngle3_2(m))^2))/(2*(secd(incidentAngle
3_1(m))-secd(incidentAngle3_2(m))));
end

%%%%%%%%%%%%%% Determine Attenuation at Each Depth %%%%%%%%%%%%%%%%
% the incremental z layer
deltaZ = layerDepth;
%determine the individual attenuation across each individual layer
%the sum of the previous attenuations
sumAlpha1 = 0;
sumAlpha2 = 0;
sumAlpha3 = 0;
for m=1:numLayers
    alphaInd1(m) = alphaAccum1(m)/deltaZ - sumAlpha1;
    sumAlpha1 = sumAlpha1 + alphaInd1(m);
    alphaInd2(m) = alphaAccum2(m)/deltaZ - sumAlpha2;
    sumAlpha2 = sumAlpha2 + alphaInd2(m);
    alphaInd3(m) = alphaAccum3(m)/deltaZ - sumAlpha3;
    sumAlpha3 = sumAlpha3 + alphaInd3(m);
end

%%%%%%%%%%%%%%%%%%%%%% Extract Temperature %%%%%%%%%%%%%%%%%%%%%%%%
for m = 1:numLayers-1
    f1 = @(T)(3*alphaInd1(m)/pi)^2*(3.1884+0.00091*T)-10^(-
4.04+0.05*T);
    T_1(m) = fzero(f1,T1(10*m));
    dT1(m) = T_1(m) - T1(10*m);
    f2 = @(T)(3*alphaInd2(m)/pi)^2*(3.1884+0.00091*T)-10^(-
4.04+0.05*T);
    T_2(m) = fzero(f2,T2(10*m));
    dT2(m) = T_2(m) - T2(10*m);
    f3=@(T)(3*alphaInd3(m)/pi)^2*(3.1884+0.00091*T)-10^(-
4.04+0.05*T);
    T_3(m)=fzero(f3,T3(10*m));
    dT3(m)=T_3(m)-T3(10*m);
end


%%%%%%%%%%%%%%%%%%%%%%%%%%%%%%%%%%%%%%%%%%%%%%%%%%%%%%%%%%%%%%%%%%%%
%%%%%%%%%%%%%%%%%%%%%%%%% Plots %%%%%%%%%%%%%%%%%%%%%%%%%%%%%%%%%%%%
%plot indexes
```

```
s1=1;
s2=290;
I=10;
figure(2)
%compare measured and extracted temperatures
plot(T1(1:I:290), zDepth(1:numLayers-1), 'r');hold on
plot(T_1, zDepth(1:numLayers-1), 'b')
plot(T2(1:I:290), zDepth(1:numLayers-1), 'r');hold on
plot(T_2, zDepth(1:numLayers-1), 'b')
plot(T3(1:I:290), zDepth(1:numLayers-1), 'r');hold on
plot(T_3, zDepth(1:numLayers-1), 'b')
grid;
h = gca;
set (h, 'YDir', 'reverse');
legend ('GRIP Measured', 'GRIP Simulated', 'Hypo.1 Measured',
'Hypo.2 Simulated', 'Hypo.3 Measured', 'Hypo.3 Simulated');
title ('Ice Temperature Profiles');
xlabel ('T, C');
ylabel ('Depth, m');

figure(3)
%compare measured and extracted temperatures
plot(dT1, zDepth(1:numLayers-1), 'r');hold on
plot(dT2, zDepth(1:numLayers-1), 'r');hold on
plot(dT3, zDepth(1:numLayers-1), 'r');hold on
grid;
h = gca;
set (h, 'YDir', 'reverse');
legend ('GRIP', 'Hypo.1','Hypo.2');
title ('Temperature Profile Estimation Error');
xlabel ('T, C');
ylabel ('Depth, m');

figure(4)
%compare measured and extracted attenuation
plot(alpha1(1:I:290), zDepth(1:numLayers-1), 'r');hold on
plot(alphaInd1(1:numLayers-1), zDepth(1:numLayers-1), 'b')
plot(alpha2(1:I:290), zDepth(1:numLayers-1), 'r');hold on
plot(alphaInd2(1:numLayers-1), zDepth(1:numLayers-1), 'b')
plot(alpha3(1:I:290), zDepth(1:numLayers-1), 'r');hold on
plot(alphaInd3(1:numLayers-1), zDepth(1:numLayers-1), 'b')
grid;
h = gca;
set (h, 'YDir', 'reverse');
legend ('GRIP Measured', 'GRIP Simulated', 'Hypo.1 Measured',
'Hypo.2 Simulated', 'Hypo.3 Measured', 'Hypo.3 Simulated');
title ('Ice Attenuation Profiles');
xlabel ('Attenuation, Np/m');
ylabel ('Depth, m');

figure(5)
%compare measured and extracted temperatures
```

```
plot(-(alpha1(1:I:290)-transpose(alphaInd1(1:numLayers-1))),
zDepth(1:numLayers-1), 'r');hold on
plot(-(alpha2(1:I:290)-transpose(alphaInd2(1:numLayers-1))),
zDepth(1:numLayers-1), 'r');hold on
plot(-(alpha3(1:I:290)-transpose(alphaInd3(1:numLayers-1))),
zDepth(1:numLayers-1), 'r');hold on
grid;
h = gca;
set (h, 'YDir', 'reverse');
legend ('GRIP', 'Hypo.1','Hypo.2');
title ('Attenuation Profile Error');
xlabel ('Attenuation, Np/m');
ylabel ('Depth, m');
```

REFERENCES

[1] Allen, C, Gandhi, M., Gogineni, P., and K. Jezek, "Feasibility Study for Mapping Polar Ice Bottom Topography using Interferometric Synthetic-Aperture Radar Technique," Information Telecommunication and Technology Center, University of Kansas, Lawrence, KS, Tech. Rep. RSL 11680-1, Jan. 1997.

[2] Allen, C., "Fall 2006 Project Background Information, Scope, and Expectation," EECS 823 Remote Sensing Class, The University of Kansas, Lawrence, KS, Fall 2006.

[3] Alley, R. "Personal Communication" "Richard Alley" ralley@geosc.psu.edu

[4] Balanis, C.A., "*Antenna Theory: Analysis and Design*", 3rd Ed., John Wiley & Sons, Inc. 2006.

[5] Bansal, R., "The Far-Field: How Far is Far Enough?," *Applied Microwave &Wireless*, November, 1999.

[6] Bogorodsky, V.V., Bentley, C.R., and P. Gudmansen, *"Radioglacicology"*, Kiewer, 1985.

[7] Booton, R.C., "*Computational Methods for Electromagnetics and Microwaves"*, Wiley Interscience, 1992.

[8] Breakal, J.K., Burke, G.J., and E.K. Miller, "The Numerical Electromagnetics Code (NEC)", 6th Symposium and Tech Exhibition on Electromagnetic Compatibility, Zurich, 1985.

[9] Chen, M., Zhang, Y., Zhao, W., and C.H. Liang, "Analysis of Antennas Around NURBS Surface with Hybrid MoM-PO Technqiue," *IEEE Transactions on Antennas and Propagation*, 2007, vol. 55, pp. 407-413.

[10] Clough, J.W., "Radio Wave Propagation in Antarctic Ice sheet," Ph.D. Thesis, University of Wisconsin, 1974.

[11] Demarest, K., "*Engineering Electromagnetics"*, Prentice Hall, 1997.

[12] Dunson, D., "A Wideband Synthetic Aperture Radar for Ice Sheet Basal Measurements," Master's Thesis, The University of Kansas, Lawrence, KS, 2006.

[13] Fernandez-Recio, R., Garcia-Castillo, L.E., Gomez-Revuelto, I., and M. Salazar-Palma, "Fully Coupled Hybrd FEM-UTD Method for Analysis of NURBS Radiation Problems," *IEEE Transactions on Antennas and Propagation*, 2008, vol. 56, pp. 774-783.

[14] GISP II Ice Core, http://www.gisp2.sr.unh.edu/

[15] Gogineni, P., Chulah, T., Allen, C., Jezek, K., and R. Moore, "An Improved Coherent Radar Depth Sounder," *J. Glaciol*., Vol. 44, pp. 659-669.

[16] GRIP Ice Core, http://www.ncdc.noaa.gov/paleo/icecore/greenland/summit/document/

[17] Haldar, M.K., "Introducing the Finite Element Method in Electromagnetics to Undergraduates Using Matlab," *International Journal of Electrical Engineering Education*, 2006.

[18] Harrington, R.F., "*Tim-Harmonic Electromagnetic Fields"*, McGraw-Hill, Inc., 1961.

[19] Harrington, R.F., *"Field Computation by Moment Methods"*, Krieger, 1968.

[20] Harrison, C.H., "Radio Echo Sounding of Horizontal Layers in Ice," *Journal of Glaciology*, Vol. 12, No. 66, 1973, pp. 383-397.

[21] HFSS Version 10 Manual, ftp://ftp.ansoft.com/techsup/download/web/primg/hfss_v10.zip

[22] HFSS Vector Field Calculations, http://www.ansoft.com/hfworkshop02/HFSS_Vector_Field_Calculations.pdf

[23] Introduction to Scripting in HFSS, ftp://162.105.247.210/incoming/aa/scripting.pdf

[24] Jin, J.M. and X.Z. Sheng, "A Hybrid FEM/SBR Method to Compute Scattering by Large Bodies with Small Protruding Scatterers," *Microwave Optical Technology Letters*, 1997., vol. 15, pp. 78-84.

[25] Kravstov, Yu.A, and Yu.I. Orlov, *"Geometrical Optics of Inhomogeneous Media"*, Springer-Verlag, 1990.

[26] Kunz, K.S. and R.J. Luebbers, *"Finite Difference Time Domain Method for Electromagnetics"*, CRC-Press, 1993.

[27] Li, J, Xie, T. and K.E. Dobbs, "Ice Temperature Profile Estimation by Using a Wideband Ice Depth Sounder," EECS 823 Final Project, The University of Kansas, Lawrence, KS, 2006.

[28] MacGregor, J.A., "Development and Applications of a Radar-Attenuation Model for Polar Ice Sheets," Ph.D. Thesis, University of Washington, 2008.

[29] Matzler, C. and U. Wegmuller, " Dielectric Properties of Fresh-water Ice at Microwave Frequencies," *Journal of Physics D: Applied Physics*, 1987, Vol. 20, pp. 1623-1630.

[30] Moore, J.C. and S. Fujita, "Dielectric Properties of Ice Containing Acid and Salt Impurity at Microwave and Low Frequencies," *Journal of Geophysical Research*, Vol. 98, No. B6, June 1993.

[31] Nesje, A., and S.O. Dahl, "*Glaciers and Environmental Change*," Arnold Publishing, London, 2000.

[32] Paden, J., Allen, C., Gogineni, P., Jezek, K., Dahl-Jensen, D., and L. Larsen, "Wideband Measurements of Ice Sheet Attenuation and Basal Scattering," *IEEE Geoscience and Remote Sensing Lett.*, Vol. 2., No. 2, Apr 2005.

[33] Panser, B., "Development of an Electrically Small Vivaldi Antenna: The CReSIS Aerial Vivaldi (CAV-A)," M.S. Thesis, University of Kansas, 2007.

[34] Paterson, W.S.B., *"The Physics of Glaciers"*, Pergamon Press, 1981.

[35] Petrenko, V. and R. Whitworth, *"Physics of Ice"*, 1st Ed., Oxford University Press, Oxford, 1999.

[36] Ramo, S, Whinnery, J.R., and Theodore Van Duzer, *"Fields and Waves in Communication Electronics,"* 3rd Ed., John Wiley & Sons, Inc., 1994.

[37] Robin, G., Evan, S., and J.T. Bailey, "Interpretations of Radio Echo Sounding in Polar Ice Sheets," *Phl. Trans. Roy. Soc. Of London*, vol. A-265, pp. 437-505, 1969.

[38] Rutledge, D.B. and M.S. Muha, "Imaging Antenna Arrays," *IEEE Trans. Antennas Propag.*, Vol. 30, pp. 535-540, 1982.

[39] Salazar-Palma, M., Sarkar, T.K., Garcia-Castillo, L.E., Roy, T., and A. Djordjevic, *"Iterative and Self-Adaptive Finite-Elements in Electromagnetic Modeling"*, Artech House, 1998.

[40] Sharawi, M.S. and Aloi, D.N., "Design of a Linearly Polarized Rectangular Patch Antenna Using MoM, FDTD, and FEM," IEEE Antennas and Propagation Symposium, June 2007, pp. 3916-1919.

[41] Smith, G. S., "Directive Properties of Antennas for Transmission into a Material Half-Space," *IEEE Transactions on Antennas and Propagation*, 1984, vol. 32, pp. 232-246.

[42] Souchez, R.A. and R.D. Lorrain, *"Ice Composition and Glacier Dynamics"*, Springer-Verlag, New York, 1991.

[43] Sowers, T. "Personal Communication", "Todd Sowers" sowers@geosc.psu.edu

[44] Stakgold, I., "*Green's Functions and Boundary Value Problems"*, John Wiley & Sons, Inc., 1979.

[45] Wang, Y., Chaudhuri, S.K., and S. SafevNaeini, "An FDTD/Raytracing Analysis Method for Wave Penetration through Inhomogeneous Walls," *IEEE Transactions on Antennas and Propagation*," 2002., vol. 50,. pp. 1598-1604.

[46] West, J.W., and K.R. Demarest, "The Radiation Characteristics of an Arbitrary Antenna Positioned on a Polar Ice Sheet", *Geophysics*, 1987